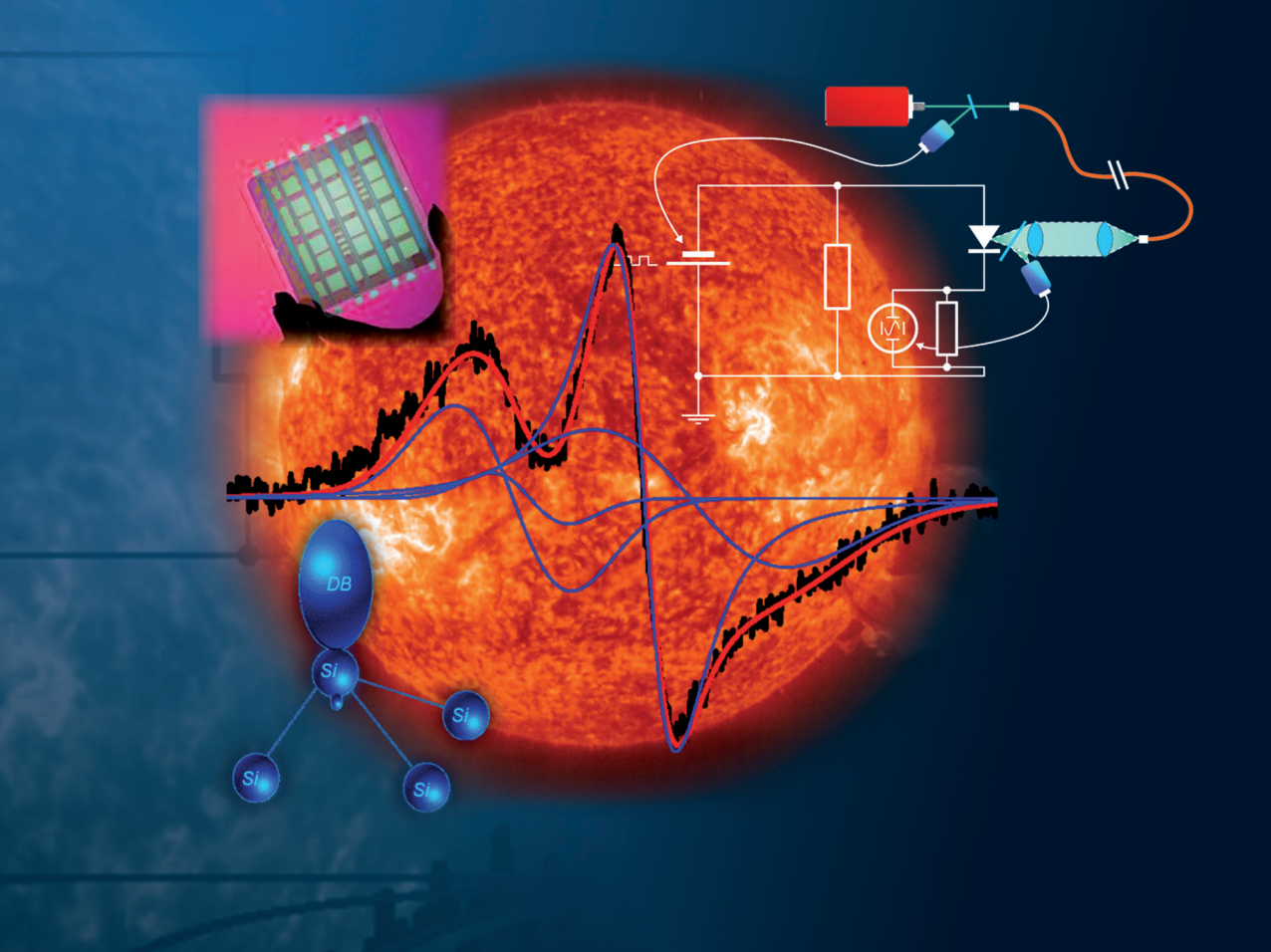


## **Electron Spin Resonance and Transient Photocurrent Measure- ments on Microcrystalline Silicon**

Thorsten Dylla





Schriften des Forschungszentrums Jülich Reihe Energietechnik / Energy Technology

Band/Volume 43

Forschungszentrum Jülich GmbH Institut für Photovoltaik

# Electron Spin Resonance and Transient Photocurrent Measurements on Microcrystalline Silicon

Thorsten Dylla

Schriften des Forschungszentrums Jülich Reihe Energietechnik / Energy Technology

Band/Volume 43

ISSN 1433-5522

ISBN 3-89336-410-2

Bibliographic information published by Die Deutsche Bibliothek. Die Deutsche Bibliothek lists this publication in the Deutsche Nationalbibliografie; detailed bibliographic data are available in the Internet at <a href="http://dnb.ddb.de">http://dnb.ddb.de</a>.

Publisher Forschungszentrum Jülich GmbH

and Distributor: Zentralbibliothek

D-52425 Jülich

Telefon (02461) 61-5368 · Telefax (02461) 61-6103

e-mail: zb-publikation@fz-juelich.de Internet: http://www.fz-juelich.de/zb

Cover Design: Grafische Medien, Forschungszentrum Jülich GmbH

Printer: Grafische Medien, Forschungszentrum Jülich GmbH

Copyright: Forschungszentrum Jülich 2005

Schriften des Forschungszentrums Jülich Reihe Energietechnik / Energy Technology Band / Volume 43

D 188 (Diss., Berlin, Freie Univ., 2004)

ISSN 1433-5522 ISBN 3-89336-410-2

Neither this book nor any part may be reproduced or transmitted in any form or by any means, electronic or mechanical, including photocopying, microfilming, and recording, or by any information storage and retrieval system, without permission in writing from the publisher.

## Kurzfassung

In der vorliegenden Arbeit wurden die elektronischen Eigenschaften von mikrokristallinen Silizium ( $\mu$ c-Si:H) Dünnschichten mittels Elektronen-Spin-Resonanz (ESR), transienter Photoleitung (Time-of-Flight (TOF)) und Messung der elektrischen Leitfähigkeit untersucht. Es wurden Modelle und mögliche Erklärungsansätze hinsichtlich der Natur und der energetischen Verteilung der elektronischen Defekte als Funktion des Filmaufbaus diskutiert und deren Auswirkungen auf den elektrischen Transport erörtert. Dazu wurde  $\mu$ c-Si:H mit strukturellen Eigenschaften im Bereich von hochkristallinem bis zu vollständig amorphen Schichten abgeschieden. Der Grad der Kristallinität wurde jeweils mittels Raman Spektroskopie bestimmt.

Es zeigt sich, dass die gemessenen Spindichten  $N_S$  mit dem strukturellen Aufbau der  $\mu$ c-Si:H Schichten korrelierten. Während die höchsten  $N_S$  generell bei hochkristallinem Material gefunden werden, verringert sich die Spindichte mit zunehmenden amorphen Volumenanteil in den Schichten. Dies kann mit den zunehmenden Wasserstoffgehalt und der damit verbundenen Absättigung von offenen Bindungen an den Säulengrenzen erklärt werden. Ferner fungiert die zusätzlich zwischen den kristallinen Säulen eingebaute amorphe Phase als Passivierungsschicht, was zu einer effektiveren Absättigung von "dangling bond" Zuständen an der Säulengrenzen führt.

In Abhängigkeit von der Struktur der Filme, insbesondere der aktiven Oberfläche, zeigen sich deutliche reversible und irreversible nderungen im ESR-Signal als auch in der Dunkelleitfähigkeit der μc-Si:H Schichten. Die poröse Struktur des hochkristallenen Materials begünstigt die Eindiffusion von atmosphärischen Gasen, welche sowohl den Charakter als auch die Dichte der Oberflächenzustände beeinflussen. Als wesentliche Ursache wurden zwei Prozesse identifiziert, Adsorption und Oxidation. Beide führen zu einer Zunahme der Spindichte. Bei der Adsorption konnte diese auf eine reversible nderung der db₂ Resonanz (g=2,0052) zurückgeführt werden, während die db₁ Resonanz (g=2,0043) unverändert bleibt. Mit zunehmenden amorphen Anteilen in den Schichten nimmt die Größe der durch Adsorption und Oxidation hervorgerufenen Effekte ab, was auf eine zunehmende Kompaktheit der Filme zurückgeführt werden kann.

Messungen an n-dotierten  $\mu$ c-Si:H Filmen wurden zur Untersuchung der Zustandsdichte in der Bandlücke benutzt und bestätigten, dass die gemessene Spindichte  $N_S$  mit der Defektdichte zusammenhängt. Die Resultate legen nahe, das für einen weiten Bereich von Strukturkompositionen die Verschiebung des Fermi-Niveaus durch die Kompensation von Zwischenbandzuständen bestimmt wird. Dies gilt für Dotierkonzentrationen kleiner als die Defektkonzentration im intrinsischen Material, während für höhere Dotierungen eine Dotiereffizienz von eins beobachtet wird. Es lässt sich folgern, das die Spindichte den Hauptteil der Zwischenbandzuständen repräsentiert ( $N_S = N_{DB}$ ).

Die Kenntnis über Art und Dichte von Defekten ist von entscheidender Bedeutung beim Verständnis des Ladungsträgertransportes. Mittels TOF-Technik wurden pin-Dioden auf der Basis von  $\mu$ c-Si:H untersucht, sowie Löcherdriftbeweglichkeiten und die zugrundeliegenden Transportmechanismen bestimmt. Trotz der sehr hohen Kristallinität der Proben zeigen temperaturabhängige Messungen, das der Löchertransport durch "Multiple Trapping" in einer exponentiellen Verteilung von Bandausläuferzuständen bestimmt ist, ein Verhalten das vorwiegend mit nichtkristallinen Materialien in Verbindung gebracht wird. Die Breite des Valenzbandausläufers konnte auf 31 meV bestimmt werden, was zu Löcherdriftbeweglichkeiten von 1-2 cm²/Vs führt. Diese Werte bestätigen das Vorhandensein von Beweglichkeitskanten für Löcher in mikrokristallinen Filmen und erweitern die Bandbreite von Materialien, für die eine anscheinend universale Bandbeweglichkeit in der Größenordnung von 1 cm²/Vs gefunden wird.

## **Abstract**

The electronic properties of microcrystalline silicon ( $\mu$ c-Si:H) films have been studied using electron spin resonance (ESR), transient photocurrent time-of-flight (TOF) techniques, and electrical conductivity measurements. Structural properties were determined by Raman spectroscopy. A wide range of structure compositions, from highly crystalline films with no discernable amorphous content, to predominantly amorphous films with no crystalline phase contributions, was investigated. Models and possible explanations concerning the nature and energetic distribution of electronic defects as a function of film composition are discussed.

It is shown that the spin density  $N_S$  in  $\mu$ c-Si:H films is linked strongly to the structure composition of the material. The highest  $N_S$  is always found for material with the highest crystalline volume fraction. With increasing amorphous content,  $N_S$  decreases, which is attributed to increasing hydrogen content and improved termination of dangling bonds. Moreover, the amorphous phase content, incorporated between the crystalline columns, appears to act as a passivation layer, leading to more effective termination of unsatisfied bonds at the column boundaries

Both reversible and irreversible changes in the ESR signal and dark conductivity due to atmospheric effects are found in  $\mu$ c-Si:H. These are closely connected to the structure composition, in particular the active surface area. The porous structure of highly crystalline material facilitates in-diffusion of atmospheric gases, which strongly affects the character and/or density of surface states. Two contributing processes have been identified, namely adsorption and oxidation. Both processes lead to an increase of  $N_S$ . In the case of adsorption the increase is identified as arising from changes of the db2 resonance (g=2.0052), while the intensity of the db1 resonance (g=2.0043) remains constant. With increasing amorphous content the magnitude of both adsorption and oxidation induced changes decreases, which may be linked to the greater compactness of such films.

Measurements on n-type  $\mu$ c-Si:H films were used as a probe of the density of gap states, confirming that the spin density  $N_S$  is related to the density of defects. The results confirm that for a wide range of structural compositions, the doping induced Fermi level shift in  $\mu$ c-Si:H is governed by compensation of defect states,

for doping concentrations up to the dangling bond spin density. At higher concentrations a doping efficiency close to unity was found, confirming that in  $\mu$ c-Si:H the measured spin densities represent the majority of gap states ( $N_S = N_{DB}$ ).

The nature and density of defects is of great importance in determining electronic transport properties. By applying the TOF technique to study pin solar cells based on  $\mu$ c-Si:H, conclusive hole drift mobility data were obtained. Despite the predominant crystallinity of these samples, the temperature-dependence of hole transport is shown to be consistent with multiple-trapping in an exponential distribution of band tail states, behavior that is frequently associated with non-crystalline materials. A valence band tail width of 31 meV, and hole band mobilities of 1-2 cm²/Vs, were estimated from the data. These measurements support the predominance of mobility-edge transport for holes in these microcrystalline films, and extend the range of materials for which an apparently universal band mobility of order 1 cm²/Vs is obtained.

## **Contents**

1	Intr	oduction	n	1
2	Fun	damenta	als	7
	2.1	Structu	aral Properties of Microcrystalline Silicon	7
	2.2		onic Density of States	9
		2.2.1	Band-Tail States	10
		2.2.2	Deep Defects	11
	2.3	Charge	Carrier Transport	14
		2.3.1	Barrier Limited Transport	15
		2.3.2	Dispersive Transport in Disordered Semiconductors	15
3	Sam	ple Pre	paration and Characterization	19
	3.1	Charac	terization Methods	19
		3.1.1	Raman Spectroscopy	19
		3.1.2	Electron Spin Resonance (ESR)	21
		3.1.3	Electrical Conductivity	24
		3.1.4	Transient Photocurrent Measurements (TOF)	24
		3.1.5	Thickness Measurements	30
	3.2	Deposi	tion Technique	32
		3.2.1	Plasma-Enhanced Chemical Vapor Deposition (PECVD) .	32
		3.2.2	Hot-Wire Chemical Vapor Deposition (HWCVD)	33
	3.3	Sample	Preparation	34
		3.3.1	Sample Preparation for ESR and conductivity measurements	35
		3.3.2	PIN-Diodes for Transient Photocurrent Measurements	36
4	Intr	insic Mi	crocrystalline Silicon	39
	4.1	Raman	Spectroscopy	39
	4.2		cal Conductivity	41
	4.3		ignals and Paramagnetic States in Intrinsic $\mu$ c-Si:H	42
	4.4		sion - Relation between ESR- and Structural Properties	47
	4.5		ary	50

#### CONTENTS

5	N-T	ype Doped μc-Si:H	51
	5.1	Structure Characterization	51
	5.2	Electrical Conductivity	52
	5.3	ESR Spectra	54
	5.4	Dangling Bond Density	55
	5.5	Conduction Band-Tail States	57
	5.6	Discussion	59
	5.7	Summary	61
6	Rev	ersible and Irreversible Effects in μc-Si:H	63
	6.1	Metastable Effects in $\mu$ c-Si:H	63
		6.1.1 Influences of Sample Preparation	63
		6.1.2 Reversible Effects in the ESR Signal	70
		6.1.3 Reversible Effects in the Electrical Conductivity	73
	6.2	Irreversible Oxidation Effects	75
		6.2.1 Reversibility by Chemical Reduction	77
		6.2.2 Charge Transfer caused by Oxidation of N-Type $\mu$ c-Si:H .	78
	6.3	On the Origin of Instability Effects in $\mu$ c-Si:H	80
		6.3.1 Adsorption of Atmospheric Gases	80
		6.3.2 Irreversible Effects caused by Oxidation	84
	6.4	Summary	84
7	Trai	nsient Photocurrent Measurements	85
	7.1	Electric Field Distribution	85
	7.2	Transient Photocurrent Measurements	87
		7.2.1 Non-Uniform Electric Field Distribution	87
		7.2.2 Uniform Electric Field Distribution	90
	7.3	Temperature Dependent Drift Mobility	93
	7.4	Multiple Trapping in Exponential Band-Tails	94
	7.5	Discussion	96
	,	7.5.1 Photocurrent and Photocharge Transients	97
		7.5.2 Hole Drift Mobilities	98
		7.5.3 The Meaning of Multiple Trapping	99
8	Scho	ematic Density of States	101
9	Sum	nmary	105
A		•	107
В	List	of Samples	111

#### CONTENTS

C Abbreviations, Physical Constants and Symbols	115
Bibliography	119
Publications	135
Acknowledgments	137

## **Chapter 1**

### Introduction

Solar cells provide a nearly inexhaustible, environmentally neutral way to produce electricity. After the first discovery of the photoelectric effect in 1839 by Becquerel [1], the technological breakthrough came in 1954 when D.M. Chapin, C.S. Fuller, and G.L. Pearson first reported of a crystalline silicon based solar cell with a conversion efficiency of  $\eta = 6\%$  [2]. Since then a lot of progress, in both the scientific and the technological sense, has been made, and nowadays conversion efficiencies for silicon solar cells of up to 20% for commercial manufacture and above 24% on the laboratory scale have been achieved [3]. However, the costs of photovoltaics are still too high to be competitive with classical electricity production, e.g. coal/oil/gas-fired or nuclear fission powerplants. Thin film solar cells offer a great potential for a reduction of costs as they combine the advantage of low temperature procession, low material consumption, large area producibility as well as the prospect of monolithic series connection to modules [4, 5]. The most promising materials for thin film solar cells are copper-indium-gallium-diselenite (CIGS), cadmium-tellurite (CdTe), and thin film silicon in various modifications. Photovoltaic modules based on amorphous silicon were the first thin film solar cells commercially available and are presently the only thin film devices that have an impact on the photovoltaic world market [5]. However, the conversion efficiencies of solar cell modules based on amorphous silicon are low ( $\eta$ =4-7 % [6]), caused by the presence of defects, tail states, and light induced degradation, known as Staebler-Wronski effect (SWE) [7].

Recently, microcrystalline silicon ( $\mu$ c-Si:H) has attracted interest due to its higher stability against light induced degradation, with the absorption extending into the near infrared, similar to crystalline silicon. First produced as a thin film by Vepřek and Mareček in 1968 [8] using a hydrogen plasma chemical transport technique, it has been shown about 10 years later by Usui and Kikuchi [9] that  $\mu$ c-Si:H can also be prepared using plasma enhanced chemical vapor deposition

(PECVD), providing compatibility with already well established amorphous thin film technology. In the last few years much progress regarding the preparation, the solar cell performance as well as the understanding of the structural and electronic properties of  $\mu$ c-Si:H has been made. However, there are still tremendous technological and scientific challenges, e.g. the understanding of the interrelation between the solar cell performance and the material properties of  $\mu$ c-Si:H are of great interest. Microcrystalline silicon as referred to in the literature describes a wide range of silicon material rather than a well defined system. In fact,  $\mu$ c-Si:H is a structure modification consisting of varying amounts of microcrystallites, hydrogenated amorphous silicon and voids [10, 11]. Interestingly, it has been shown that not, as one might expect, material with the highest crystalline volume fractions and the largest crystallite size but material prepared close to the transition to amorphous growth yields the highest conversion efficiencies [12, 13]. Obviously, the transition between microcrystalline and amorphous growth is of great importance. Approaching this transition, e.g. by increasing the silane concentration, the structural as well as the optoelectronic properties, e.g. the electronic conductivity, the photosensitivity as well as the spin density, of the  $\mu$ c-Si:H material change significantly [14, 15, 16, 17, 18, 13]. The variation of the amorphous volume content is often accompanied by changes of the compactness of the material. In particular it is generally observed that deposition conditions which lead to the technologically needed high deposition rates, tend to result in a porous structure. Also attempts to grow material with large grain size in order to improve the carrier mobility, frequently result in porous material. Although it has been reported that  $\mu$ c-Si:H is more resistant [13] and highly crystalline material even does not suffer from SWE [19], the presence of crack-like voids makes this material susceptible to in-diffusion of impurities and atmospheric gases which might lead to various metastable and irreversible effects. Earlier investigations on highly crystalline material prepared with chemical transport deposition show that atmospheric gas adsorption and/or oxidation affects the density of surface states, electrical transport and the electron spin density [20]. So far only a few investigations on inand meta-stable effects on recently prepared material exists [21, 22, 23], and the detailed nature of these effects is presently still not understood. The rather complicated structure has major consequences on the electronic structure, e.g. the density of states (DOS) within the band gap. In particular, since there is no well defined structure, the microscopic identification of states observed is complicated as they can be located in the various phases, at boundaries or at interfaces. It is therefore not surprising that there exists no conclusive DOS map and the understanding does in many cases not go beyond a phenomenological description. Thus a study of the density and properties of defect states as a function of the structural composition is of great importance.

Electron spin resonance (ESR) is a powerful tool to investigate and identify

defect states provided that they are paramagnetic and it has been successfully applied to amorphous silicon and its alloys (see e.g. [24, 25, 26]). First applied to  $\mu$ c-Si:H in the 80s [20, 27, 28], systematic studies have only been performed in the last recent years, and various ESR signals have been identified [29, 30, 31, 32]. Intrinsic  $\mu$ c-Si:H shows an asymmetric signal with contributions at g=2.0043 (db<sub>1</sub>) and g=2.0052 (db<sub>2</sub>). The origins of these lines are still under discussion. While it has been suggested that the asymmetry results from an axial symmetric g-tensor of defects on grain surfaces [31], there are a number of indications that these lines originate from two independent states located in different microscopic environments [21, 33, 34, 35, 36, 32]. For n-type material and also for illuminated material a third resonance at g=1.996-1.998 can be observed. According to a similar resonance found in polycrystalline silicon this resonance has been called CE-Line and has been attributed to electrons in the conduction band [27, 29] and later also to shallow localized states in the conduction band-tail [35, 36, 37, 38]. A number of reports on ESR properties of highly crystalline n-type  $\mu$ c-Si:H have been published and show that highly crystalline n-type material shows a nearly linear dependence of the dark conductivity  $\sigma_d$  on phosphorous doping concentrations for  $PC = [PH_3]/([PH_3] + [SiH_4])$  higher than 10 ppm [30, 39, 40]. For lower doping concentrations the conductivity deviates from this linear dependence. It is likely that within this doping regime the Fermi level shift is governed by the compensation of gap states. However, this has not been proven yet and will be a key task of this work.

Moreover, the presence of localized states within the bandgap has a major influence on the transport properties and has to be considered in order to explain transport features. In contrast to c-Si, the occurrence of band-tail states and deep defects open additional transport paths, they might act as traps for charge carriers, or form barriers. There is, of course, a wide range of possible structures in microcrystalline silicon materials. This explains the large spread in reported drift mobilities and transport properties. In the past, various models have been proposed to describe the transport in  $\mu$ c-Si:H. These models adopt and combine former approaches successfully applied for either polycrystalline or pure amorphous material, e.g. for n-type  $\mu$ c-Si:H the so called "grain boundary trapping model" [41], successfully applied to poly-crystalline silicon, has been used to describe the transport behavior [42, 43] and also percolation models were applied to interpret conductivity and Hall effect data [44, 45]. On the other hand, similarities between a-Si:H and  $\mu$ c-Si:H suggest that structural disorder are from constitutional importance and transport might take place by direct tunneling between localized states (hopping) or by trap-limited band motion (multiple trapping) [46, 47, 48, 49].

This work provides a comprehensive study of paramagnetic centers in  $\mu$ c-Si:H. Material with different structure compositions and doping levels have been inves-

tigated by ESR and electrical conductivity. It will be shown that structural changes influence the nature as well as the density of the defects. Accompanied by structural changes the material tends to be susceptible of instabilities due to adsorption and chemical reactions of atmospheric gases. The present work investigates and identifies instability effects caused by adsorption and oxidation in state of the art material, with a wide range of structure compositions. The application of additional n-doping will be used as a probe for the density of gap states. Additionally, the transport properties of highly crystalline  $\mu$ c-Si:H will be studied using transient time-of-flight experiments.

#### This thesis is organized as follows:

- **Chapter 2:** A short summary of the structural properties as well as their impact on the electronic structure of microcrystalline silicon is given. In the second part, the influences of the electronic properties on electrical transport will be treated. Different transport models proposed for  $\mu$ c-Si:H material are shown and compared.
- **Chapter 3:** A short presentation of the experimental techniques, used in this work, is followed by a brief description of the deposition process and the particular preparation of the samples.
- **Chapter 4:** In Chapters 4-8, the results of the material characterization are presented and discussed. Chapter 4 addresses the properties of paramagnetic states in intrinsic μc-Si:H with varying structure compositions ranging from highly crystalline to fully amorphous.
- **Chapter 5:** In this Chapter films with different structure compositions and doping levels are studied by ESR and electrical conductivity. n-Doping densities in the range of the intrinsic defect density are used as a probe for the density of gap states.
- **Chapter 6:** Electron spin resonance and conductivity measurements are used to study adsorption and oxidation effects on  $\mu$ c-Si:H with different structure compositions. The magnitude of observed meta-stable and irreversible effects will be discussed with respect to changes of the active surface area.
- **Chapter 7:** The hole transport properties of highly crystalline material are studied in this Chapter. Transient photocurrent measurements are presented and consistently analyzed using the model of multiple trapping in an exponential band-tail.

**Chapter 8:** In this chapter, the information derived from the studies in Chapters 4-7 will be combined and summarized in a schematic picture of the density of states in both, a spatial and energetic sense.

**Chapter 9:** In this last chapters, the most important results will be summarized and the conclusions are drawn.

## Chapter 2

### **Fundamentals**

In this first chapter, the basic structural properties of microcrystalline silicon as well as their consequences for the density of states are discussed. As the electronic density of states (DOS) is mainly determined by the disorder of the system, the nature of band-tail states and deep defects are discussed. In the third section of this chapter the transport properties are outlined with respect to the DOS.

#### 2.1 Structural Properties of Microcrystalline Silicon

Microcrystalline silicon ( $\mu$ c-Si:H) as referred to in the literature describes a wide range of silicon material rather than a well defined structure. In fact,  $\mu$ c-Si:H is a general term for a silicon composition containing varying amounts of crystalline grains, amorphous phase, and voids. These phases are separated from each other by a disordered silicon tissue or grain boundaries additionally complicating the structure. To obtain a picture of the structure, a number of characterization methods, e.g. transmission electron microscopy (TEM), X-ray diffraction (XRD), and Raman spectroscopy, have been applied in the past [10, 50, 51]. A schematic picture of the structure derived from these works is shown in Fig. 2.1. The figure shows a wide range of material structures ranging from highly crystalline, left hand side, to predominantly amorphous growth on the right hand side. The particular structure of the  $\mu$ c-Si:H strongly depends on the deposition conditions. The transition in growth can be achieved by varying a number of different deposition parameter, as has been demonstrated by Roschek, [53], Vetterl [12] for plasma enhanced chemical vapor deposition (PECVD), and by Klein [13] for material prepared by hot-wire chemical vapor deposition (HWCVD). In particular the silane concentration is very useful to control the crystallinity of the  $\mu$ c-Si:H material. However, the structure not only depends on the deposition conditions, but also on the substrate used. In particular for material deposited at the transition

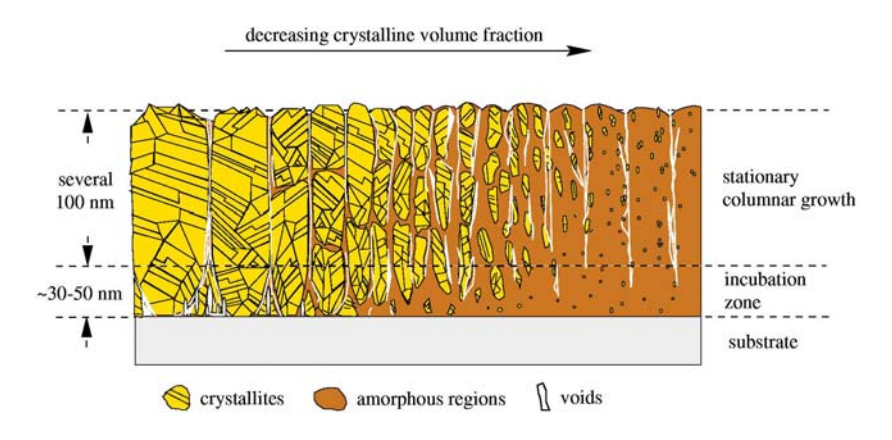


**Figure 2.1:** Schematic picture of structure features found in  $\mu$ c-Si:H. From left to right the film composition changes from highly crystalline to amorphous. The picture was taken from Houben [52]

between  $\mu$ c-Si:H and a-Si:H growth, the structure varies significantly depending on the substrate. While for a fixed set of process parameters the material deposited on aluminum foil results in crystalline growth, fully amorphous structure can be observed for the one deposited on glass [54, 55, 50]. The substrate dependence is of particular importance and has to be kept in mind if one wants to compare results obtained from different measurement techniques, since different substrates, e.g. glass or aluminum, are required for different methods.

Typical for all structure modifications is the occurrence of an incubation zone. The particular thickness and composition of this region strongly depends on the deposition condition and the substrate used. In the highly crystalline regime, crystallization starts from nucleation centers close to the substrate-film interface. With increasing film thickness the diameter of the columnar structures increases resulting in the typically observed conical shape. In the highly crystalline regime the columnar clusters of coherent regions have a diameter of up to 200 nm and extend over the whole film thickness. However, the structure inside the columns is not monocrystalline. In fact it consists of coherent regions with a diameter of 4-20 nm that are separated from each other by stacking faults and twin boundaries [10, 50, 56, 57, 58].

The columns themselves are separated from each other by crack-like voids and disordered material. In fact, studies using transmission electron microscopy (TEM) [50, 10], infrared spectroscopy (IR) [11, 59], and hydrogen effusion [60] have shown that highly crystalline material often exhibits a pronounced porosity.

Studies have also shown that these voids may extend from the surface deep into the film and allow for in-diffusion of atmospheric gases along the column boundaries [20, 22].

An increasing amorphous phase content leads to a reduction of the column diameter, while an extended disordered phase is incorporated in the increasing incubation layer and at the column boundaries. Concerning the porosity there is some not yet understood discrepancy between results obtained from TEM and IR. While TEM shows cracks and voids, there is no indication of oxygen in-diffusion or low temperature hydrogen effusion in such material, suggesting a rather compact structure. At the site of transition between crystalline and amorphous growth, the material structure changes significantly. The columns no longer extend throughout the entire film thickness. In fact, the crystalline regions are frequently interrupted and embedded in an amorphous matrix. The size of the crystalline domains decreases as the size of the coherent regions forming them. Finally only amorphous growth is obtained and no crystalline contribution can be found in the material. However, the electronic properties of the amorphous phase found in this kind of material differs from standard a-Si:H and is therefore often referred to as "protocrystalline", "polymorphous" or "edge material" [61, 62, 63].

#### 2.2 Electronic Density of States

The structural properties of  $\mu$ c-Si:H, in particular the disorder, lead to some phenomena in the electronic density of states (DOS) that cannot be found in the crystalline counterpart. The lack of translational symmetry leads to some major consequences for the electronic properties of the material. However, as the electronic structure is mostly determined by the short range order, the overall electronic properties are very similar compared to the equivalent crystal. But, due to the lack of long range order, the abrupt band edges found in the crystal are replaced by a broadened tail of states extending into the forbidden gap. On the other hand, the deviation from the ideal network structure also results in electronic states deep within the gap (dangling bonds). As microcrystalline silicon is a phase mixture of crystalline and disordered regions separated by grain boundaries and voids, the particular band structure dependents on the particular spatial position within the material, and an overall DOS-diagram can not be drawn easily.

In the following section a brief description of the main features of the DOS is given. On the basis of the simplified picture for the DOS in a-Si:H, shown in Fig. 2.2, band-tail and defect states are discussed and adopted for a description of the DOS of  $\mu$ c-Si:H. Note, while the schematic DOS for a-Si:H shown in Fig. 2.2 is sufficient to describe a number of experimental results including electron spin

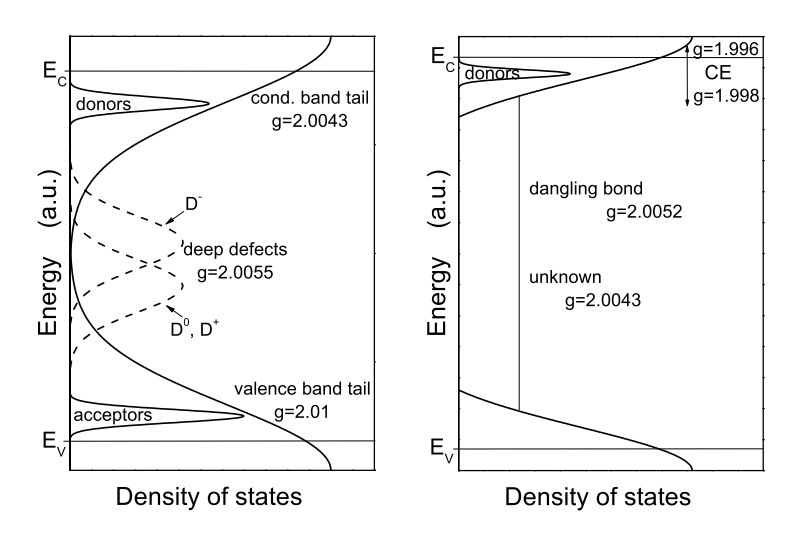


Figure 2.2: Schematic density of states of amorphous (left) [65] and microcrystalline (right) silicon [39].

resonance (ESR) very well, there are other models for the distribution of defects, e.g. the so-called defect-pool model (see e.g. [64] for a review), which however will not be treated here.

#### 2.2.1 Band-Tail States

One consequence of a missing long range order is the existence of band-tail states. Local fluctuations in the interatomic distances and the bonding angles result in spatial fluctuations of the band edges. This leads to regions within the band, where charge carriers can be trapped. The existence of localized states in disordered material was first predicted by Anderson [66], and it has been shown by Mott that any random potential introduces localized states in the tails of the band [67, 68]. The resulting DOS is schematically shown in Fig. 2.2, where the usually sharp band edges are replaced by a broad tail extending deep into the bandgap. Within the band-tail localized and extended states are separated by mobility edges at energies  $E_C$  or  $E_V$ , respectively. The mobility edge derives its name from the fact that at zero temperature only charge carriers above  $E_C$  (for  $E_V$  below) are mobile and contribute to transport [68]. While these ideas have been developed and experimentally proven mainly for amorphous material, it has been shown by Werner et al. [69, 70, 71] that for poly-crystalline silicon, the spatial distribution of defects at grain boundaries also leads to potential fluctuations, resulting in band-

tail states.

As grain boundaries and amorphous phase content are an inherent structure feature of  $\mu$ c-Si:H, it is most likely, that localized band-tail states might also exist is this material class. Evidence for the existence of band-tail states comes from e.g. electron spin resonance [39, 72], electrical transport measurements [73], photo deflection spectroscopy [44], and photo luminescence measurements [74, 75]. From transient photocurrent measurements on a-Si:H material one can deduce that the tail falls exponentially towards the mid-gap (for a review see e.g. [76]). The same shape was also found in poly-crystalline silicon [69, 70] and has lately been adopted to  $\mu$ c-Si:H [77, 75, 73]. Though the exact underlying reasons are unclear, theoretical works confirm the existence of exponential tails [78, 79, 80, 81, 82]. The particular width of the band-tail depends on the bonding character of the states and degree of disorder. Despite these theories, the precise relation between structural disorder and band-tail shape remains unclear.

The effect of band-tails is unique for the disordered phase and the influence of localized states is apparent in electrical transport, doping, recombination and other phenomena.

#### 2.2.2 Deep Defects

In a crystal any departure from the perfect crystalline lattice is a defect, this definition then needs to be reviewed in the case of  $\mu$ c-Si:H. As shown in section 2.1 the particular structure of  $\mu$ c-Si:H is determined by (i) a lack of long range translation symmetry in the amorphous phase, (ii) a high density of twins and stacking faults within the columns, and (iii) grain boundaries. Structural defects, as defined in crystalline semiconductors, are therefore inherent parts of the system and it is not very helpful to think of it as a collection of only defects. In the context of this work it is more useful to define a defect as a deviation from the fourfold bonding configuration. This kind of defect will form for example at the grain boundaries, where the ordered lattice of the crystalline grains abruptly ends. On the other hand, Phillips has shown that for a disordered tetrahedral bonded semiconductor it is impossible to construct a "continuous random network" (CRN) without extremely large internal stress. Broken or unsaturated bonds will therefore be formed to release the internal stress. These defects form states with an energy position between the bonding and anti-bonding states, roughly speaking in the middle of the band gap (see Fig. 2.2). In hydrogenated silicon, however, most of the broken bonds are saturated by hydrogen.

#### **Defect Relaxation and Correlation Energy**

In the case of the silicon dangling bond, the defect can exhibit three charge states. Besides the neutral  $D^0$ , where the defect is singly occupied, there are a positively charged  $D^+$  and a negatively charged configuration  $D^-$ , where the dangling bond is occupied with zero or two electrons, respectively (see left panel of Fig. 2.2). The energy position within the band gap depends on the charge state of the dangling bond defect. Starting from a singly occupied defect  $(D^0)$ , the adjoining of a second electron influences the total energy of the defects in a way, that

- 1. due to Coulomb interaction the two electrons repel each other splitting the energy level of the  $D^0$  and the  $D^-$  state by the correlation energy  $U_{corr} = e^2/4\pi\varepsilon\varepsilon_0 r$ , where r is the effective separation of the two electrons and thus roughly the localization length of the defect wave function [65];
- 2. if the network around a defect is able to readjust around a negatively charged defect, this may cause a change in the bonding and lowers the energy by an amount of  $U_{relax}$ .

The effective correlation energy  $U_{eff}$  is a combination of both the Coulomb  $U_{corr}$  and the relaxation energy  $U_{relax}$ ,

$$U_{eff} = \frac{e^2}{4\pi\varepsilon\varepsilon_0 r} - U_{relax} \tag{2.1}$$

If the relaxation energy  $U_{relax}$  exceeds the correlation energy  $U_{corr}$  (negative  $U_{eff}$ ), the energy level of the doubly occupied state  $D^-$  is smaller than the one of the neutral state  $D^0$ . Thus in an equilibrium state only  $D^+$  and  $D^-$  defects and no singly occupied states are observed. This behavior can be found in the defect structure of e.g. chalcogenide glasses [83].

In  $\mu$ c-Si:H, there is a lot of experimental evidence that dangling bond states possess a positive effective correlation energy  $U_{eff}$ . In this case the level of the neutral defect  $D^0$  lies below the one occupied with two electrons  $D^-$ , as shown in Fig. 2.2. Thus, unlike the case of the negative  $U_{eff}$ , the defect can exist in the neutral state that, due to the existence of an unpaired electron, acts as a paramagnetic center and can therefore be detected by electron spin resonance (ESR).

#### Paramagnetic States in $\mu$ c-Si:H

The particular structure of  $\mu$ c-Si:H offers a number of sites where dangling bond defects can be located: the crystalline regions, the grain boundaries, the amorphous phase or due to the presence of impurity atoms like oxygen. This is the reason why, in contrast to a-Si:H, the structure of paramagnetic defects is not yet

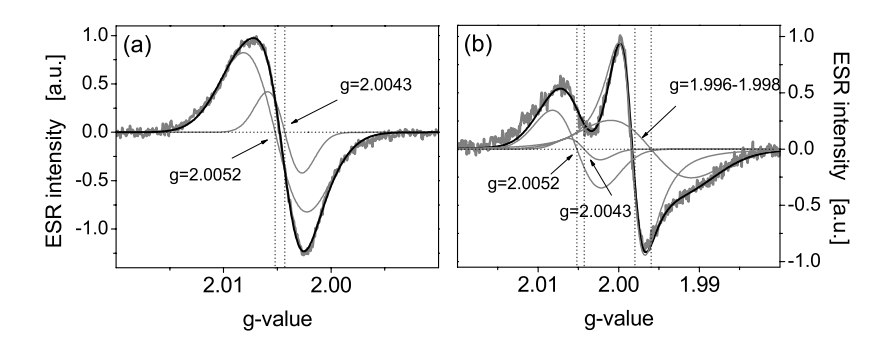


**Figure 2.3:** Typical ESR-Spectra of (a) undoped  $\mu$ c-Si:H with contributions at g=2.0043 and g=2.0052 and (b) n-doped material with an additional contribution at g=1.998. Both spectra were taken from material investigated in this work.

well understood. Besides the unknown microscopic location, there are also uncertainties regarding the energy positions of defects within the gap, which have been taken into account in the schematic DOS of  $\mu$ c-Si:H shown in the right panel of Fig. 2.2. For intrinsic  $\mu$ c-Si:H, the most important paramagnetic defect is the Si dangling bond (DB). An ESR spectrum of high quality intrinsic material shows an asymmetric line shape with contributions at g=2.0043 and g=2.0052. A typical spectra taken of undoped  $\mu$ c-Si:H material is shown in Fig. 2.3 (a). The origin of these two contributions is still controversially discussed. While it has been suggested by several authors that the anisotropy arises from two independent dangling bond states in different microscopic environments [21, 33, 35, 34, 36, 32], Kondo et al., on the other hand, assigned the two components contributing to the ESR signal to an axial symmetric g-tensor of  $P_b$ -like<sup>1</sup> defects located on < 111 > oriented grain surfaces with components of  $g_{\parallel}=2.0022$  and  $g_{\perp}=2.0078$  [31]. A more recent publication from de Lima et al. [84] also suggested the signal arising from an axial-symmetric center, but extracted g-values of  $g_{\parallel} = 2.0096$  and  $g_{\perp} = 2.0031$ , relating the signal with defects in the crystalline phase.

As microcrystalline silicon can consist of a considerable amount of amorphous phase, also dangling bond defects located in the a-Si:H fraction may contribute to the ESR signal. The DB defect found in a-Si:H has a characteristic g-value of g=2.0055 and a typical peak to peak line width of  $\Delta H_{pp} = 10$  G in X-band<sup>2</sup> [85].

Another aspect of the increasing amorphous phase is the Staebler-Wronski-Effect (SWE) [7]. The SWE describes the light induced breaking of weak Si-Si bonds in the silicon network which leads to the creation of additional dangling

 $<sup>{}^{1}</sup>P_{b}$  centers are silicon dangling bonds at the Si/SiO<sub>2</sub>-interface of oxidized silicon wafers.

<sup>&</sup>lt;sup>2</sup>For details of the notation see section 3.1.2

bond defects [86]. For highly crystalline  $\mu$ c-Si:H, it has been shown that it does not suffer from the SWE [19]. However, due to the presence of amorphous phase, this material might also be susceptible to light-induced metastable effects, which in fact was recently confirmed by Klein [87].

For n-type doped and also for illuminated intrinsic  $\mu$ c-Si:H samples, another resonance with a g-value of g=1.996-1.998 can be observed (Fig. 2.3 (b)). Since the intensity of this signal is correlated with the dark conductivity  $\sigma_D$  at 300 K and the g-value is close to the one of free electrons in crystalline silicon, this signal was first attributed to electrons in the conduction band [27, 29]. The resonance has therefore been referred to as the conduction electron (CE) resonance. Later on, this signal has also been attributed to localized states in the conduction bandtail [88, 35, 38, 39, 72].

#### **Substitutional Doping**

Controlled incorporations of impurities are typically used to provide additional free charge carriers. Typical donors and acceptors used to dope silicon are phosphorus and boron, respectively. In crystalline silicon (c-Si), the inclusion of dopants immediately lead to a shift of the Fermi level  $E_F$  up to an energy position, located between the energy level of the dopant and the band edge, even for very low doping concentrations. In contrast to crystalline silicon, the high concentration of intrinsic defects has a major influence on the free carrier concentration achieved from doping. Additional incorporation of e.g. donors will be compensated by the defects as they act as acceptors by creating  $D^-$  states, accumulating the charge carriers. This is the reason why deep defect states within the band gap first have to be compensated before the Fermi level can shift to the conduction band edge.

For amorphous silicon another complication prevents that high doping densities can be achieved. The doping induces deep states in the gap preventing a shift of the Fermi level [89, 90]. Different, independent experiments have shown that the total defect density increases with the square root of the doping concentration [65].

#### 2.3 Charge Carrier Transport

In crystalline silicon, the charge carrier transport takes place in the extended states of the band and can be described using effective mass theory [91]. In  $\mu$ c-Si:H, on the other hand, the presence of localized states within the bandgap has a major

influence on the transport properties and has to be considered in models used to explain transport features. The existence of band-tail states and deep defects may open new transport paths or they might act as traps for charge carriers or form barriers.

In the past, various models have been proposed adopting and combining models successfully used to describe transport data from either poly-crystalline or pure amorphous material. As  $\mu$ c-Si:H consists of small crystals separated by grain boundaries, first attempts to explain the transport behavior were done adopting the model of "grain boundary trapping" developed for polycrystalline silicon by Seto [41] and further extended by Baccarani et al. [92]. On the other hand, the existence of band-tail states suggests that transport might take place by direct tunneling between localized states (hopping) or by trap-limited band motion (multiple trapping). In the following section a phenomenological description of these ideas and their consequences will be given.

#### 2.3.1 Barrier Limited Transport

The model of barrier limited transport is based on the ideas of Seto [41] and got a further improvement by Baccarani [92] (see also [93]). It is successfully used to describe the transport behavior of poly-crystalline silicon. As microcrystalline silicon consists of crystallites separated by grain boundaries, the model proposes that the transport properties are mainly determined by defect states located at the grain boundaries. Charge carriers can be trapped and ionize these states leading to potential barriers. Charge carriers overcome these barriers by thermionic emission. Temperature dependent measurements done by Spear et al. [94] and Willeke [95] seemed to prove this model showing the characteristic temperature activated mobility expected for barrier limited transport, but have only been performed in a small temperature range. On the other hand, conductivity measurements over a wide range of temperatures showed that  $\mu$ c-Si:H does not exhibit a single activated transport behavior [44]. Lately this model has been further refined by including tunneling as a process to overcome the barriers [42] in order to explain Hall mobilities of n-type  $\mu$ c-Si:H. A detailed discussion of barrier-controlled transport in microcrystalline semiconductors can be found e.g. in Refs. [42, 96].

#### 2.3.2 Dispersive Transport in Disordered Semiconductors

On the other hand, the existence of a broad tail of states extending into the gap (see section 2.2.1 for details), suggests that these states play an important role in the transport mechanism. As discussed above, band-tail states are a result of structural disorder. A typical transport feature found in disordered materials is that of

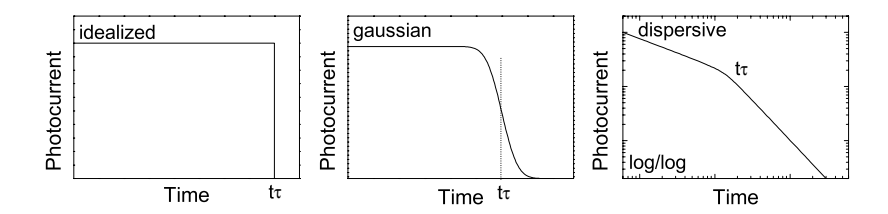


**Figure 2.4:** Current pulse shapes obtained in a time-of-flight experiment. The different shapes are a result of different transport mechanism leading to different degrees of dispersion as described in the text.

dispersive transport. In Fig. 2.4 transient photocurrents are shown. Experimentally, these currents can be measured by e.g. time-of-flight experiments (TOF), described in section 3.1.4.

In a TOF experiment, the material of interest is usually packed between two contacts and the time required for a charge carrier packed to drift from one side of the sample to the other is measured. The left panel of Fig. 2.4 shows an idealized current following the generation of charge carriers. It describes a sheet of charge, photoinjected on the front side of the sample, moving across the specimen with a constant velocity. The current breaks down at the transit time  $t_{\tau}$  where the charge carriers reach the back contact. In practice, however, the initially discrete packet of charge carriers will broaden as it drifts across the specimen (middle panel of Fig. 2.4). The dispersion w is a consequence of statistical variations in scattering processes and carrier diffusion which is connected to the drift mobility through the Einstein relation  $(D = \frac{kT}{e}\mu_d)$ . When the first carriers arrive at the back contact, the current starts to drop, the width of the current decay is a measure of the dispersion at that time. In this case the transit time is defined as that time at which the mean position of the charge carrier packet traverses the back electrode. This is equal to the time, where half the charge has been collected. Because of the shape of the dispersion it is referred to as Gaussian transport in the literature.

While transit pulses of the form shown above are observed in many crystalline and some amorphous solids, in some cases they differ significantly. A typical current transient shape for such a case is shown in the right panel of Fig. 2.4 (note the log-log scale). Quite surprisingly, the current appears to decrease over the whole time range of the measurement. Even at times prior to the transit time  $t_{\tau}$  the current does not show a constant value as observed for Gaussian transport. Perhaps the most outstanding feature is that as a function of time the current decays approximately linearly on a logarithmic scale, indicating a power-law behavior. The two linear regimes are separated by a time  $t_{\tau}$  and show the following time distribution

function

$$I(t) \propto \begin{cases} t^{-(1-\alpha_1)} & t < t_{\tau} \\ t^{-(1+\alpha_2)} & t > t_{\tau}. \end{cases}$$
 (2.2)

The dispersion parameter  $\alpha_{1,2}$  is determined by the disorder of the material [97]. Note that Eq. 2.2 has no characteristic long time cut-off, in fact, even at times greater than  $2t_{\tau}$  the magnitude of the current suggests that still a significant number of charge carriers remains within the specimen. Such a high degree of dispersion occurs when during transport the average charge carrier experiences a single localization event with a time that is comparable with the mean transit time defined by the applied voltage and the sample thickness [98]. A second phenomenon observed is the universality of the transient current pulse shape. Transient currents measured for a given sample at different applied fields exhibit the same degree of relative dispersion. This behavior also extends to variations in the sample thickness.

To account for the high degree of dispersion, two mechanism have been proposed, namely hopping and trap-limited band transport.

#### **Hopping**

In a hopping system, developed by Scher and Montroll [99], the transport is based on hopping and tunneling of the charge carriers between states. The probability for a transition varies with the separation R of two sites as  $\exp(-2R/R_0)$ , where  $R_0$  is the localization radius of the state (equal to the effective Bohr radius for localized carriers) [68]. If the mean intersite distance  $\bar{R}$  is large compared to  $R_0$ , one will observe a wide spread of the probabilities to escape from a state and the broadening of the charge carrier packet is highly pronounced. The dispersion arises from the random distribution of the site separation. The immobilized carriers are trapped in centers more isolated from their neighbors than the average distance. With increasing time, the drifting carriers will be more and more accumulated in more isolated sites with longer release time constants. This results in the observed continuously decaying current even for very long times.

Hopping in an exponential band-tail has been applied to describe the transport behavior of  $\mu$ c-Si:H in the low temperature region [46, 47] as well as the behavior found at elevated temperatures [46, 48].

#### **Multiple Trapping in Band-Tails**

A number of studies in 1977 showed that dispersive transport can also arise from trap-limited band transport [100, 101, 98, 102, 103]. In a multiple trapping model, charge transport only takes place in the extended states of the band. Charge carriers trapped in localized states are immobile and must first be thermally excited

above the mobility edge to contribute to transport. It has been shown by Schmidlin [98] that for anomalous dispersion to be generated, the concentration of the localized states must accomplish the following two criteria. First, a charge carrier is likely to be trapped in a localized state at least once during the transit and second, the release time of a carrier trapped in a localized state must be comparable to the transit time  $t_{\tau}$  [98]. As has been discussed above (see section 2.2.1), the band-tails in  $\mu$ c-Si:H are expected to decrease exponentially towards the gap. Provided that the localized states in the vicinity of the mobility edge all to have the same origin, e.g. potential fluctuations, the energy dependence of the capture cross section is probably weak [104], so that each localized state has the same probability to capture a charge carrier. However, the exponential dependence of the thermal reemission leads to a broad distribution of release times. The dispersion arises from the energy distribution of states and since thermal excitation is involved, both the mobility and the dispersion strongly depend on temperature.

## **Chapter 3**

## Sample Preparation and Characterization

This chapter summarizes the experimental methods used to prepare and characterize the material investigated in this work. In the first section the measurement techniques applied to study the material properties are discussed. The second part describes the basics of the deposition techniques, namely plasma enhanced chemical vapor deposition (PECVD) and hot wire chemical vapor deposition (HWCVD). As for different characterization methods different substrates and device structures are needed, the last section will provide an overview of the particular sample preparations and treatments.

#### 3.1 Characterization Methods

The aim of this section is describe the potential, but also the limitations of the individual techniques used for the material characterization. In this study, Raman spectroscopy was used to determine the crystallinity of the material, paramagnetic states were studied by electron spin resonance (ESR) and transport properties were investigated using conductivity measurements and transient photocurrent experiments (TOF).

#### 3.1.1 Raman Spectroscopy

Raman spectroscopy can provide detailed information about the vibrational properties of solids, liquids, and gases. A detailed description of the underlying physics can be found in the literature [105, 106]. Reviews of the application to  $\mu$ c-Si:H can be found in [107, 108] and a detailed description of the setup used in this work

in [109, 52]. Here Raman spectroscopy has been used to determine the crystalline volume content of the  $\mu$ c-Si:H material.

As described in section 2.1  $\mu$ c-Si:H is a phase mixture of crystalline and amorphous material. A typical Raman spectrum, as shown in Fig. 3.1, is a convolution of a crystalline and an amorphous spectrum. Spectra of crystalline silicon are dominated by a peak at  $520 \, \mathrm{cm}^{-1}$  attributed to the transversal optical (TO) phonon. Due to the finite grain size and internal stress in  $\mu$ c-Si:H this peak shifts to lower values (usually found at  $518 \, \mathrm{cm}^{-1}$ ) and the peak width increases [110, 107]. As a result of the absence of long range translation symmetry in a-Si:H, the quantum number  $\vec{k}$  is no longer well-defined and the excitation of a phonon is possible without restriction of  $\vec{k}$  preservation. In a-Si:H, one therefore observes a broad intensity distribution of the TO-phonon at 480 cm<sup>-1</sup>. Besides these two peaks a third peak at around 492 cm<sup>-1</sup> is often observed in  $\mu$ c-Si:H Raman spectra. This peak is a result of stacking faults in the crystalline phase, also referred to as wurtzite peak [111].

To account for the asymmetry, the crystalline peak was fitted by two Gaussian lines centered at 518 cm $^{-1}$  and 505 cm $^{-1}$ . As a measure of the crystallinity, the Raman intensity ratio  $I_C^{RS}$  was used, defined as

$$I_C^{RS} = \frac{I_{518} + I_{505}}{I_{518} + I_{505} + I_{480}}. (3.1)$$

For a given sample,  $I_C^{RS}$  was determined by de-convoluting the spectra into three contributions at wave numbers of 518, 505 and 480 cm $^{-1}$ . Although  $I_C^{RS}$  is related to the volume content of crystalline and disordered phase this evaluation must be used carefully. The Raman cross sections for crystalline and amorphous silicon are different and additionally they depend on the wavelength of the incident laser light. Measured by Tsu et al. [112], the cross section ratio at  $\lambda=496.5$  nm is  $\sigma_c/\sigma_a=0.88$ . Additionally, grain boundaries may lead to a signal at 480 cm $^{-1}$  [113]. For these reasons  $I_C^{RS}$  can be considered as a lower limit of the crystalline volume content.

Information about the distribution of the crystalline volume fraction in the growth direction can be obtained by using different excitation wavelengths  $\lambda$ . In this work laser wavelengths of 488 nm and 647 nm were used, that corresponds to an information depth<sup>1</sup> of 150 nm and 800 nm, respectively.

The validity of the determination of the crystallinity by Raman spectroscopy used in this work is still under discussion. While Ossadnik et al. [114] found no correlation between the Raman intensity ratio and the crystalline volume fraction obtained from X-ray diffraction measurements, recent work in the Juelich group

<sup>&</sup>lt;sup>1</sup>The information depth is defined as half of the absorption depth (depth where the signal is attenuated to a fraction of 1/e).

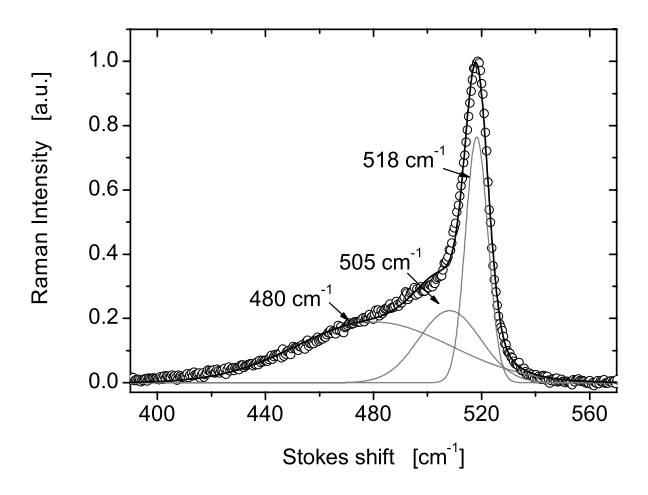


**Figure 3.1:** *Typical Raman spectrum of a μc-Si:H film.* 

shows a clear correlation between  $I_C^{RS}$ , X-ray diffraction and TEM [115, 116]. However, there is broad agreement that the crystallinity is underestimated by the Raman intensity ratio.

#### 3.1.2 Electron Spin Resonance (ESR)

Since the first spectrum recorded in 1945 [117], electron spin resonance (ESR)<sup>2</sup> has developed into a powerful spectroscopic technique used in many areas of modern physics, chemistry and biology. The subject matter of ESR is the interaction of electrons with magnetic fields and with each other. In this section the physical principles of ESR will be briefly discussed, followed by a brief description of the actual measurement.

#### 3.1.2.1 Spin Hamiltonian

For a system containing only one unpaired electron spins (S=1/2) the Hamilton operator can be written as

$$\mathcal{H} = g_0 \mu_B B_0 \mathbf{S} + \mu_B B_0 [\Delta g] \mathbf{S}. \tag{3.2}$$

where  $g_0$  is the electronic g-value for a free electron ( $\approx 2.0023$ ),  $\mu_B$  the Bohr magneton,  $B_0$  is the flux density,  $[\Delta g]$  is the interaction tensor of the spin orbit

<sup>&</sup>lt;sup>2</sup>In the literature also referred to as Electron Paramagnetic Resonance (EPR)

coupling, and S the spin operator [118]. For the following discussion, terms due to hyperfine interaction, the interaction with the nuclei spin, and the spin-spin interaction are neglected because they have no resolvable contribution to the spectra measured in this work.

In Eq. 3.2 the second term describes the coupling of the electron spin with the magnetic moment of the orbital angular moment  $\mathbf{L}$ , whereas the tensor quantity  $[\Delta g]$  describes the deviation of the g-value from that of the free electron  $g_0$ . In covalent semiconductors, where the electronic eigenstates are usually described in terms of s- and p-state wavefunctions,  $\mathbf{L}$ , whose eigenstates are degenerate, has a zero expectation value if the crystal field interaction greatly exceeds the Zeeman term [24]. This effect is known as quenching of the orbital angular momentum by the crystal field. In this special case the second term in Eq. 3.2 becomes zero.

However, due to the interaction with a magnetic field the degeneracy of the eigenstates of  $\mathbf{L}$  is lifted and the quenching is partly removed. For an unpaired electron in the ground state, the elements of the g-tensor  $g_{ij}$  in the second term of Eq. 3.2 are given by [118]

$$g_{ij} = -2\lambda \sum_{n(\neq 0)} \frac{\langle \Psi_0 | L_i | \Psi_n \rangle \langle \Psi_n | L_j | \Psi_0 \rangle}{E_n - E_0}$$
(3.3)

where  $\lambda$  is the spin orbit coupling parameter. The index n counts all other orbitals  $\Psi_n$ ,  $E_0$  denotes the energy of the ground state and  $E_n$  the energy of the state  $\Psi_n$ . The g-value is therefore an important quantity in ESR measurements and serves to distinguish and identify electronic states. However, in disordered or powdered material the angular dependence is masked as all orientations can be observed at the same time. The obtained spectra are called "powder spectrum".

#### 3.1.2.2 Lineshape and Linewidth

Besides the g-value, the shape and the width of the resonance line contains a number of information about the spin system [119, 118]. It is important to note that in ESR one talks about the peak-to-peak width, which is defined as the width between the maximum and minimum of the derivative of the absorption line. Depending on the specific lineshape of the curve this value differs by a numerical factor from the linewidth at half maximum (FWHM) typically used in other spectroscopy methods.

In general one distinguishes between two different mechanisms broadening the resonance line, first the "homogeneous" broadening which is caused by the relaxation of the excited spin state and second the inhomogeneous broadening as a result of an unresolved overlap of different ESR lines.

#### **Homogeneous Broadening**

Because of the finite lifetime of an electron in the excited state, the uncertainty principle leads to a finite so called "natural linewidth". While an excited electron is re-enters its ground state its energy will be transferred to the surrounding lattice. Within a time  $T_1$  the spin-lattice relaxation restores the system into its the equilibrium state. In addition, there is an interaction of the spins with each other. The time constant of this spin-spin relaxation process is typically denoted  $T_2$ . From the spin-lattice and spin-spin relaxation the lineshape is of the form of a Lorentzian [118].

#### **Inhomogeneous Broadening**

Differences from the Lorentzian line shape discussed above can arise from g-value anisotropy or an unresolved hyperfine interaction. Additionally broadening can also result from structural disorder. In this case the overall resonance line consists of a number of narrower individual lines, that are a result of the so-called spin packets. Each spin packet can be seen as an individual system of spins, having the same Lamor frequency  $\omega_i$  around "their" magnetic field vectors  $B_i$ . In general  $B_i$  is given by the sum of the externally applied field  $B_0$  and the local field  $B_i^{loc}$ . Due to inhomogeneities, like crystal irregularities, magnetic field inhomogeneities, or dipolar interaction between unlike spins, the local field  $B_i^{loc}$  differs for spins belonging to different spin packets. The observed line shape is therefore a contribution of several Lorentzian signals arising from different spin packets. For disordered semiconductors like amorphous and microcrystalline silicon both, the energetic position as well as the local environment of the spins may not be identical, which leads to numerous slightly different g-values. Both effects are expected to be statistically distributed and thus the resulting line shape of the convolution of the homogeneous lines is of the form of a Gaussian.

#### 3.1.2.3 Experimental Setup

ESR has been measured using a commercial X-band spectrometer (BRUKER ESP 380E). A reflex klystron working at a frequency of around 9.3 GHz with a maximum power output of about 200 mW was used as the microwave source. During the measurement the microwave frequency was kept constant while the resonance conditions were reached by scanning the magnetic field  $B_0$ . The ESR signal was recorded using phase sensitive detection so that the measured signal intensity is proportional to the first derivative of the absorption signal. The area under the absorption curve, which is proportional to the spin density  $N_S$ , was obtained by double integrating the measured signal, numerically. For a quantitative analysis

of the ESR spectra (calculation of the g-value and the spin density  $N_S$ ) the ESR signal was compared to that of a sample of un-hydrogenated sputtered amorphous silicon, which was calibrated to a standard of Picein and DPPH [120]. For temperature dependent measurements a He gas flow cryostat (Oxford ESR 900) was used. To avoid condensation of water at the walls the cavity was purged with dry nitrogen.

ESR measurements were performed in a temperature range between 4.5 K and 300 K using a modulation frequency of 100 kHz and a modulation amplitude of 2 G. The microwave power could be attenuated in the range between 200 mW -  $0.2~\mu W$  and was usually set such that saturation effects did not occur. Details of the sample handling and the preparation can be found in section 3.3.1.

#### 3.1.3 Electrical Conductivity

Conductivity measurements were performed on specimens deposited on roughened borosilicate glass prepared in the same run as the samples prepared for ESR measurements. As contacts, coplanar silver pads were evaporated under high vacuum conditions having a thickness of 700 nm, an electrode spacing b=0.5 mm, and a width l=4 mm. In order to avoid errors due to surface coverage all measurements were performed under high vacuum (p < 0.01 Pa) conditions after an annealing step of 30 min at 450 K (compare section 6 and 6.3). To ensure that the determined conductivity is voltage independent (ohmic contacts), I-V curves have been measured between  $V = \pm 100$  V.

Having determined the current I for an applied voltage V (usually set to V=100 V) the specific dark conductivity  $\sigma_D$  is given by

$$\sigma_D = \frac{b \cdot I}{l \cdot d \cdot V} \tag{3.4}$$

where d is the film thickness and l, b are determined by the contact geometry (see above).

Temperature dependent measurements were performed between 100 K and 450 K using a nitrogen cooled continuous flow cold finger cryostat.

#### 3.1.4 Transient Photocurrent Measurements (TOF)

The time-of-flight (TOF) technique was first described by J.R. Haynes and W. Shockley in 1951 [121] and was further improved by R. Lawrence and A.F. Ribson in 1952 [122]. The first application to an amorphous material (a-Se) was first done by W. Spear in 1957 [123, 124, 125] and since then it has widely been used to obtain valuable information on transport processes in a wide range of low mobility amorphous and crystalline solids.

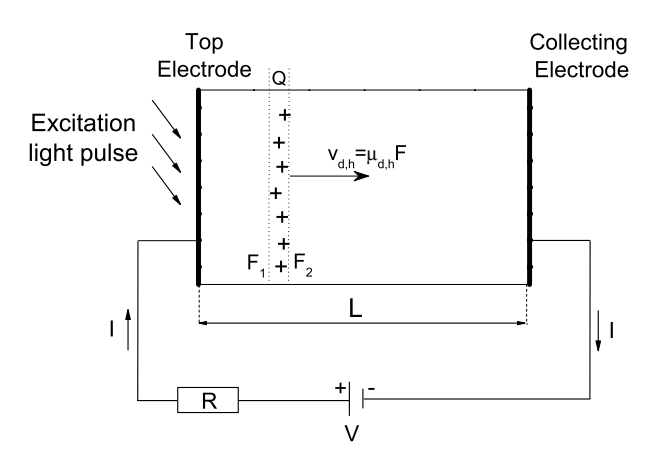


Figure 3.2: Schematic view of a time-of-flight experiment.

#### 3.1.4.1 Basic Features of the Time-of-Flight Technique

The aim of the experiment is to measure the time required for a charge carrier packet to drift from one side of the sample to the other under the influence of an applied electric field. The simplest embodiment of a time-of-flight experiment is illustrated in Fig. 3.2. The material of interest is sandwiched between two contacts; one, preferably both are semitransparent. Electron-hole pairs are injected on one side of the dielectric at a time t=0 using a short flash of strongly-absorbed light. Depending on the direction of the applied electric field F=V/L, where V is the applied voltage and L the thickness of the sample, either the electrons or the holes are drawn across the material with a drift velocity of

$$\mathbf{v}_d = \mu_d F. \tag{3.5}$$

This drifting charge carrier sheet will modify the applied field F. Simple electrostatic considerations show that the electric fields  $F_1$  and  $F_2$  indicated in Fig. 3.2 are given by

$$F_1(t) = F - \frac{q}{\varepsilon \varepsilon_0} \left( 1 - \frac{\mathbf{v}_d t}{L} \right) \tag{3.6}$$

$$F_2(t) = F + \frac{q}{\varepsilon \varepsilon_0} \left( \frac{\mathbf{v}_d t}{L} \right) \tag{3.7}$$

where q is the charge carrier density,  $\varepsilon$  is the dielectric constant of the material,  $\varepsilon_0$  the dielectric constant of the vacuum, and t the time [125, 126, 127]. These time dependent electric fields  $F_1$  and  $F_2$  will in turn induce a redistribution of the

charge at the electrodes. The current induced by this redistribution is called displacement current. As the current has to be the same everywhere in the circuit, the displacement current inside the sample has to be matched by an identical current in the external circuit. The drift motion of the charge carrier packet can therefore be detected by measuring the current induced in the external circuit. This current

$$I = \frac{q \mathbf{v}_d}{L} \tag{3.8}$$

is determined by the product of the injected charge q with its average drift velocity  $v_d$  normalized to the sample thickness L. While they are in motion the drifting charge carriers generate a displacement current which terminates when reaching the back contact. From the arrival time  $t_\tau$  an average drift mobility  $\mu_d$ 

$$\mu_d = \frac{L^2}{Vt_\tau} = \frac{L}{Ft_\tau} \tag{3.9}$$

can be determined.

Two facts are important to note at this point: (1) all generated charge inside the sample contributes to the integrated current measured in the external circuit to how far it moves through the sample, i.e. if an electron moves halfway across the sample one-half electron charge will flow through the external circuit and (2) for a constantly applied bias voltage the only way current can be induced in the external circuit is by motion of charge inside the sample.

#### 3.1.4.2 Requirements for a TOF-Experiment

From the section above one can deduce some basic conditions that must be met for a time-of-flight experiment to be feasible. In general the description of charge carrier transport used above can only be applied to insulating solids where the transit time is short compared to the dielectric relaxation time  $\tau_{rel} = \epsilon \epsilon_0/\sigma$  of the material. Due to the redistribution of the background charge located inside the material the dielectric relaxation causes a screen out of the injected charge. It also affects the externally applied field by redistributing the space charge in response to the applied potential and the applied field will no longer be uniform within the sample [128]. Blocking contacts are used to avoid an additional injection of charge carriers. To guarantee a uniform field during the period of carrier drift the external voltage is usually applied as a pulse right before the carrier injection.

As shown in Eq. 3.6 and 3.7 the drifting charge carriers may also perturb the externally applied electric field within the sample. Time-of-flight experiments are therefore performed in the space charge free regime, where the density of photoin-jected charge carriers is low enough, so that the self-field has little influence on the external field ( $F_{self} \ll F$ ). This is fulfilled when the integrated charge is small

compared to CV, where C is the capacitance of the specimen and V the externally applied voltage [129]. Within this limit the photocurrent scales linearly with the density of injected charge.

In principle the lower limit of a transit time  $t_{\tau}$  that can be measured is determined only by the *RC* time of the electronic circuit. The overall rise time of the system has to be shorter than the time scale of the experiment. On the other hand, the drift length  $\mu_d \tau_D F$  of the charge carriers has to be longer than the sample thickness *L*. In other words the transit time  $t_{\tau}$  has to be shorter than the deep trapping life time  $\tau_D$ , the time until the charge carriers are finally trapped in deep traps [99, 130].

Assuming that the charge induced by the laser is small compared to the CV the limitations of a reliable time-of-flight experiment can be expressed by

$$RC \ll t_{\tau} \ll \tau_{rel}, \tau_d$$
 (3.10)

where the lower limit is the RC response time and the upper is determined by the dielectric relaxation  $\tau_{rel}$  and the deep trapping life time  $\tau_d$ .

#### 3.1.4.3 Transit Time Evaluation

In contrast to Gaussian transport, in the case of dispersion the excess charge carrier packet spreads out to a much higher degree in a non-symmetrical way (see section 2.3.2). In addition, the absence of a long time cut-off of the transient current makes it rather complicated to define a characteristic transit time  $t_{\tau}$ . A number of different methods have been used in the past to evaluate the transit time. This has led to different results for  $t_{\tau}$  depending on the particular method used and therefore has to be taken into account if one wants to compare mobility results obtained and published by different groups.

This section will provide a short overview about the different methods. A more detailed review has been presented by Qi Wang et al. [131].

#### **Transient Photocurrent Method**

The "Transient Photocurrent Method" was used by a number of authors, e.g. Scharfe et al., Pai et al., Tiedje et al. and Serin et al. [76, 132, 133, 49]. Measuring the transient photocurrent as shown in Fig. 2.4, the characteristic transit time  $t_{\tau}$  is simply defined as the "kink" in the power law.

#### Method of Normalized Photocurrents

For the determination of  $t_{\tau}$  using the "Method of Normalized Photocurrents", the photocurrent transients measured at different applied fields are normalized using

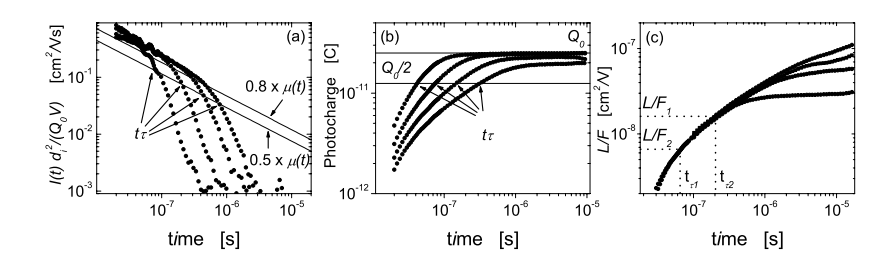


**Figure 3.3:** Graphical evaluation of the transit time using the (a) method of normalized photocurrents, (b) the half-charge method, (c) the normalized photo charge technique as described in the text. Each panel shows 4 different curves taken on a  $\mu$ c-Si:H sample at different applied voltages V.

 $I(t)d^2/(Q_0V)$ , where d equals the specimen thickness,  $Q_0$  is the total charge of the excess charge carrier package, and V the applied voltage. As shown in Fig. 3.3 (a) the pre-transients overlap establishing an "envelope" curve  $\mu(t)$ . The "envelope" curve  $\mu(t)$  is used to determine the transit time. About the exact evaluation of the transit time there is still some controversy. While Marshall, Street, and Thompson defined the transit time as the crossing point of the measured transient with the curve  $0.8 \times \mu(t)$  [134], Nebel et al. used  $0.5 \times \mu(t)$  which gives somewhat larger values of  $t_\tau$  as can be seen in Fig. 3.3 [135, 136].

#### **Half-Charge Method**

The evaluation of the transit time using the "half-charge" method is based on the same principle as used for Gaussian transport. The procedure to determine  $t_{\tau}$  is illustrated in Fig. 3.3 (b), where the transient photocharge obtained by integrating the transient photocurrents is plotted versus the time. As the number of charge carriers in the packet is determined by the value where the charge transients show an asymptotic behavior, the transit time can be extracted by evaluating the time where half the charge has been collected. This method is typically applied to determine  $t_{\tau}$  for Gaussian transport behavior. However, Wang et al. have shown that this evaluation is also valid in the case where transport is dispersive [131]. This method has widely been used by the Schiff group [131, 137, 138].

#### **Normalized Photo Charge Technique**

The "half-charge method" described above is based on the fact that at times before the charge carriers have reached the collecting electrode, the photocharge Q(t) is proportional to the distance moved by the mean position of the photocarrier distri-

bution. This can be written as the following equation, derived from calculating the electrostatic energy dissipated by a charge  $Q_0$  in a uniform electric field F which is  $Q_0Fx(t)$ . Equating this with the energy furnished by the externally applied bias voltage Q(t)V one gets

$$x(t) = d\frac{Q(t)}{Q_0}. (3.11)$$

From Eq. 3.9 one concludes that the transit time is solely determined by the ratio L/F. Doubling both, electric field F and distance L, the transit time remains unchanged. Generalizing the distance L to x(t) Eq. 3.9 can be written as:

$$\frac{L}{F} = \frac{x(t)}{F} = Q(t)\frac{d^2}{Q_0 V}$$
 for  $(t \ll t_\tau)$  (3.12)

Equating the transit photocharge, by integrating the photocurrent, L/F can be determined by using Eq. 3.12 and can be plotted as a function of time. These graphs are referred to as "displacibility plots"; a typical example is shown in figure 3.3 (c). The transit time for a chosen value of L/F can be determined directly from the graph, as indicated in the figure. As this method is simply an enhancement of the half-charge method it is clear that transit times obtained are consistent with the other methods. However, there are two advantages of using this method. First, only a handful of transients are enough to obtain a continuous curve of transit times and secondly one can obtain the displacibility for transit times shorter than would be accessible by increasing the applied voltage. This method introduced by Schiff et al. in 1993 has been used by a number of other authors [131, 139, 140, 141, 142].

#### 3.1.4.4 Experimental Arrangement

The experimental arrangement used for time-of-flight measurements is illustrated in Fig. 3.4. The charge carriers were excited using a nitrogen laser pumped dye laser (Laser Science Inc.) with a pulse width of 3 ns. As laser dye Coumarin 500 with an emission maximum at  $\lambda = 500$  nm was used, so the carrier generation took place within the first 160 nm of the illuminated side of the intrinsic layer. Stronger absorbed light was intentionally avoided to prevent back diffusion problems. The intensity of the laser was attenuated with neutral density filters until the photogenerated charge was below the CV-limit (see section 3.1.4.2). The repetition rate of the laser was chosen to a value low enough to avoid a build up of charge in the material. A value of 2 Hz was allowable for temperatures between T=300 K and 100 K.

The specimens were mounted on the cold finger of a commercial vacuum cryostat (Oxford Instruments Model DN1754). This allowed measurements in the temperature range between T = 77 K and 350 K. Additionally, the cryostat acted

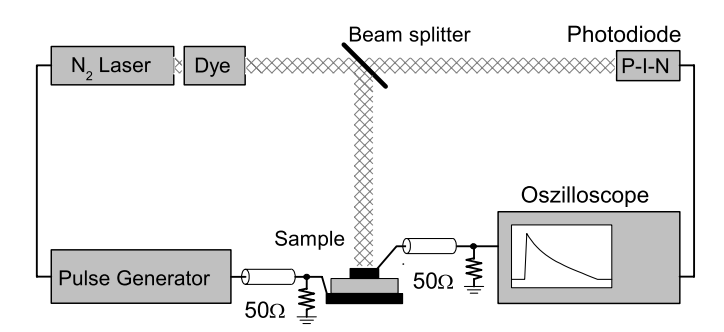


Figure 3.4: Schematic view of the experimental setup for time of flight measurements used in this work.

as a shield against electromagnetic interferences and also avoided influences of optical bias effects from accidental room light illumination. Great care was taken that the series resistance of the contacts was sufficiently small not to limit the time resolution of the system. To induce photocarrier drift an electric field was applied by a bias voltage across the sample. A step voltage was used to assure that the applied field was uniformly distributed (see section 3.1.4.2 and [128]). The photocurrent transients were measured by recording the voltage across a 50  $\Omega$  resistor in the time range between  $t=0-10~\mu s$ . For longer times a larger resistor of typical 0.3–33 k $\Omega$  was used. In order to reduce the signal-to-noise ratio the average of 100 pulses was taken. For data acquisition and averaging of the transients a digital oscilloscope (LeCroy Model 9400, 500 MHz bandwidth) was used. The oscilloscope was connected to a computer for storage and analysis of the measured currents.

#### 3.1.5 Thickness Measurements

In this work, thin films of  $\mu$ c-Si:H as well as pin diodes containing a  $\mu$ c-Si:H ilayer were prepared and investigated. Details of the preparation and particular structures can be found in section 3.2 and 3.3. For most of the methods presented, a knowledge of the film or the i-layer thickness is of great importance. Two different methods for thickness measurements were applied, namely mechanical step profiling and capacitance measurements. The advantages and limitations of both methods will be discussed in the following.

Mechanical measurements of the film thickness were performed using a mechanical step profiling system (Sloan DEKTAK 3030 Auto II). This method has been used for the measurements of both thin films and pin diodes. For films de-

posited on molybdenum and glass substrates the abrupt step necessary for the measurement was created by scratching the film and then applying and tearing off an adhesive tape. Thereby, a part of the film teared off from the substrate leaving a sharp edge. In the case of the pin diodes the step was created by mechanically scratching away the Si-layers using a scalpel. The bottom ZnO was then etched away with an HCl solution. Afterwards the thickness of the thin films or diodes could be measured using the mechanical step profiling system. To determine the i-layer thickness of the diodes, the thickness of the doped layers as well as the thickness of the ZnO has to be subtracted. The advantage of this method is that it measures the thickness directly with a precision of not less than 10 nm for thin films and about 50 nm in the case of the diodes. The shortcoming of this method is that an abrupt step right next to the position of interest has to be created, which especially in the case of the pin structures might destroy the device by creating shunt resistances.

Measuring the capacitance of the pin structure provides a simple, nondestructive way to determine the i-layer thickness of the PIN-diodes using:

$$C = \frac{\varepsilon \varepsilon_0 A}{d_w}. (3.13)$$

Here  $\varepsilon$ , A, and  $d_w$  are the dielectric constant, the area of the contacts, and thickness of the depletion layer, respectively. The dielectric constant of silicon is  $\varepsilon$ =11. Capacitance measurements were performed using a pulse generator (Avtech, Av-1023-C) and a digital oscilloscope (LeCroy, Model 9400). Two different methods were used to estimate the capacitance. The first is to determine the RC-time constant of the sample/load resistor system, by measuring the current decay following the application of the external field on the sample. The second approach was to determine the charge induced by a voltage step. Therefore a known capacitance  $(C_{ext})$  was connected in series with the sample. As the charge between the two capacitors can only be displaced, both capacitors  $C_{ext}$  and  $C_{Sample}$  store the same amount of charge. By measuring the voltage  $V_{ext}$  across  $C_{ext}$ , the capacitance of the sample can be calculated using:

$$C_{Sample} = \frac{C_{ext.} V_{ext.}}{V_{appl.} - V_{ext.}}. (3.14)$$

The induced charge has been measured 500 ns after the application of a voltage step. This method is commonly applied to amorphous silicon diodes and gives values which are in agreement with values obtained from physical measurements. However, it was found that for  $\mu$ c-Si:H structures sometimes the capacitance is up to one order of magnitude higher than calculated from the geometry of the specimen [143, 144].

# 3.2 Deposition Technique

Two well established and widely used techniques for the deposition of thin films of silicon are plasma enhanced chemical vapor deposition (PECVD) and hot wire chemical vapor deposition (HWCVD). Both methods are based on the decomposition of silicon containing gases. The major difference between both processes is the way how the precursors are made. While in PECVD the gases are decomposed by a plasma, in HWCVD the reaction takes place at a hot wire usually made of tungsten or tantalum. Both deposition techniques will be briefly described in the following section.

#### 3.2.1 Plasma-Enhanced Chemical Vapor Deposition (PECVD)

A very common method for the preparation of microcrystalline silicon is plasma enhanced chemical vapor deposition (PECVD), also known as glow discharge deposition. Detailed information about this technique and the underlying physics can be found in the literature, e.g in the books by Chapman [145], Haefer [146], Frey and Kienel [147], or Luft and Tsuo [148]. In this work, a 6-chamber deposition system with designated chambers for p-, n-, and intrinsic layers was used. A detailed description of the technical realization can be found in the work by Vetterl [12].

In the PECVD process the source gases are decomposed by an electrical discharge. The main mechanism for the decomposition is the impact of electrons, that take up sufficient energy from an alternating electrical field with typical frequencies in the range between 13.56 and 150 MHz. The precursors arising diffuse and drift to the substrate, usually placed on one electrode, and contribute to the film growth after several secondary gas phase reactions. The detailed plasma chemistry and growth mechanism are of course much more complex. A major advantage of PECVD is that the activation energy for the dissociation of the source gases comes from an externally applied alternating electric field and does not need to be supplied thermally. Therefore the substrate temperature  $T_S$  can be adjusted independently, allowing the use of low  $T_S$ .

#### **Deposition Parameters**

The main source gas for the deposition of amorphous and microcrystalline silicon is silane (SiH<sub>4</sub>). An overview about the possible reactions in a silane plasma was given by e.g. Perrin et al. [149]. The structure and the electro-optical properties of the silicon films depend on various deposition parameters. It has been shown that with the admixture of hydrogen ( $H_2$ ) to the silane plasma or by the use of high discharge powers microcrystalline growth can be achieved [150]. In particular the

admixture of hydrogen  $(H_2)$  offers a straightforward way to change the growth conditions all the way from highly crystalline to amorphous growth. The silane concentration SC defined as the ratio of silane gas flow and the total gas flow, is therefore one of the main parameters varied in this work.

$$SC = \frac{[SiH_4]}{[SiH_4] + [H_2]} \tag{3.15}$$

Besides the gas composition several of other parameters are significant in determining the properties of the deposited films; the deposition pressure p, the substrate temperature  $T_S$ , and the plasma power density P. The plasma excitation frequency  $\nu_{ex}$  is also very important for the film properties and classifies the process into RF-PECVD (standard frequency of 13.56 MHz) and VHF-PECVD (higher frequencies up to 150 MHz). Doping can be achieved by adding trimethylboron (TMB) or diborane (B<sub>2</sub>H<sub>6</sub>) and phosphine (PH<sub>3</sub>) for p-type and n-type doping, respectively<sup>3</sup>. Deposition parameters used throughout this work are listed in table 3.1

**Table 3.1:** Typical PECVD-Deposition Parameters used within this work.

Parameter		value
Excitation frequency	$v_{ex}$	95MHz (VHF)
Plasma power density	P	$0.07 \text{ W/cm}^2$
Substrate temperature	$T_{Sub}$	200°C
Pressure	p	40 Pa
Silane concentration	SC	2 - 100%
Phosphor doping	PC	0 - 20 ppm
Boron doping	BC	0 - 70 ppm

## 3.2.2 Hot-Wire Chemical Vapor Deposition (HWCVD)

Hot-wire chemical vapor deposition (HWCVD), also known as catalytic chemical vapor deposition (CAT-CVD) [151, 152, 153], is becoming increasingly popular in the field of silicon thin film deposition, particularly since recently it was

 $<sup>^3</sup>$ Doping densities are typically measured in parts per million (ppm). Taking the density of crystalline silicon a doping density of 1ppm corresponds to about  $5 \times 10^{16}$  doping atoms per cm $^3$ . However, the built-in factor as well as the doping efficiency of the dopant have to be taken into account in order to determine the active doping density.

demonstrated that solar cells prepared with HWCVD can show power conversion efficiencies comparable to solar cells prepared with PECVD [13]. The use of HWCVD instead of PECVD promises higher deposition rates for  $\mu$ c-Si:H (30 Å/s and higher [154, 155]) and prospects for upscaling [156], which however has only partly been fulfilled so far [13].

Although the dissociation of silane is of catalytic nature, wire temperatures of T > 1500 K are necessary for the decomposition of silane and hydrogen that are used as source gases for the film growth. The choice of material used for the wire is therefore limited by thermal stability; tantalum and tungsten are typical choices. Both materials desorb only atomic silicon and hydrogen at temperatures higher than 1700K [157]. Only at lower temperatures the dissociation into silyl radicals like SiH<sub>2</sub> and SiH<sub>3</sub> is of some importance. For a detailed discussion about the HW deposition technique, gas phase reactions, and the technical realization of these processes see [13] and references therein.

#### **Deposition Parameters**

As in PECVD, the main source gases for the deposition of amorphous and microcrystalline silicon are  $SiH_4$  and  $H_2$ . The structure and composition of the resulting films can be varied by simply changing the hydrogen dilution. A second parameter varied in this work is the substrate temperature, which has a major influence on the properties of the deposited films. Typical hot-wire deposition parameters used throughout this work can be found in table 3.2.

Table 3.2: Typical HWCVD parameters used in this work.

Parameter		value
Filament temperature	$T_F$	1530°C-1650°C
Substrate temperature	$T_{Sub}$	180°C −450°C
Pressure	p	3.5-5 Pa
Silane concentration	SC	3 - 25 %

### 3.3 Sample Preparation

In this work material prepared by HWCVD as well as PECVD has been investigated. For the different experimental methods applied (see section 3.1), different substrates and structure configurations are necessary. Details of the preparation of the different samples and structures will be given in the following sections.

# **3.3.1** Sample Preparation for ESR and conductivity measurements

For ESR measurements the use of powdered samples allows large amounts of material to be placed in the resonant cavity. This results in high signal intensities and thereby an improved signal-to-noise ratio. Therefore, material investigated by ESR, is usually deposited on aluminum (Al) foil. For the deposition standard household foil (brand "Alio") was cleaned with 2-Propanol (99.5% purity) and wrapped around four glass substrates, each of  $25 \times 100 \text{ mm}^2$  size. Usually one of the substrates was equipped with one or two square holes  $(10 \times 10 \text{ mm}^2)$  in which a different substrate could be placed, e.g. roughened glass substrates for conductivity measurements. A typical arrangement of the substrates is shown in Fig. 3.5.

After deposition the chamber was flushed with argon for 5 minutes and then evacuated. To cool down, the substrate was kept in vacuum ( $p \approx 10^{-9}$  mbar) for at least 3 hours. Afterwards, the material was immediately prepared for the measurement. The Al foil was etched away with a 16% HCl solution. The remaining flakes of  $\mu$ c-Si:H material were filtered out and thoroughly rinsed in de-ionized water. Finally the material was dried for about 24 hours at ambient ( $T \approx 30^{\circ}C$ ). The  $\mu$ c-Si:H powder was then inserted into quartz tubes with an inner diameter of 4 mm and a wall thickness of d = 0.5 mm. If the powder consisted of very loosely packed flakes, which was the case for highly crystalline films, the material was additionally crushed to obtain comparable packing densities and filling heights.

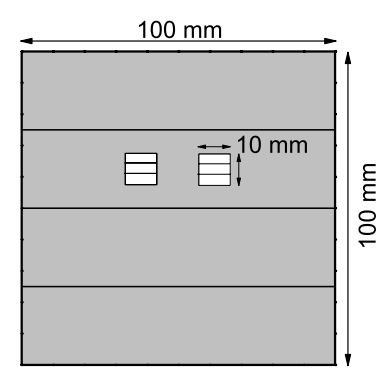


**Figure 3.5:** Typical substrate arrangement for the deposition of  $\mu$ c-Si:H thin films using Al foil. The Al foil is wrapped around 4 glass substrates (25 × 100 mm<sup>2</sup>). The square holes in one of the substrates were used to mount roughened glass substrates, which were co-deposited and later used for e.g conductivity measurements.

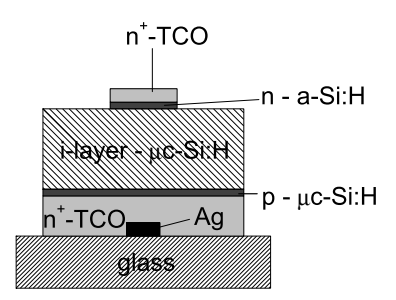


Figure 3.6: Schematic picture of a pin diode prepared for time-of-flight measurements.

This procedure also made sure that the material fits into the homogeneous part of the magnetic field. To maintain a defined environment, the powdered material was sealed into the quartz tubes under He atmosphere. This procedure yielded filling heights of about  $0.5-1~\rm cm$  with a material mass between  $22-300~\rm mg$ .

During this process the  $\mu$ c-Si:H is in contact with water and air for several hours. Alternatively, material has been also deposited on molybdenum foil (Mo). The foil had a size of  $100 \times 100$  mm, a thickness of d=0.05 mm, and a purity of 99.9%. From the Mo foil the material peeled off in flakes after bending the foil and could be sealed immediately without further treatment. As for the Al substrates, the Mo foil was equipped with a hole so that e.g. glass substrates could be deposited in the same run.

To study the influence of different environments during storing or annealing, the material was removed from the He filled tubes and sealed into Ar or  $O_2$  atmosphere or was treated in HCl solution or water as discussed above. Samples for conductivity measurements have been prepared on roughened borosilicate glass  $(4 \times 15 \text{ mm}^2)$  in the same run as their ESR counterparts. Roughened glass was used because films with a thickness larger than  $d=1~\mu m$  tend to peel off from a smooth substrate. After deposition, coplanar silver contacts were evaporated under high vacuum conditions having a thickness of 700 nm, a width of 4 mm, and a distance of 0.5 mm.

#### 3.3.2 PIN-Diodes for Transient Photocurrent Measurements

Besides limitations due to the material investigated, the main criterion for a specimen suitable for time-of-flight (TOF) measurements is the existence of blocking contacts. The samples used for time-of-flight measurements were pin structures as shown in Fig. 3.6 which were prepared using VHF-PECVD (for details about the process see section 3.2.1). As in forward bias the pin diode passes the current, in

reverse bias mode the contacts do not inject charge. Another advantage of the pin structure is that it is essentially the same as used for solar cells, so the measured TOF properties can be directly related to the device performance.

Sodium-free laboratory glass (Corning 1737) was used as substrate. To contact the diode to the external circuit, silver stripes with a thickness of d = 700 nm and a width of b=1 mm were evaporated on to the glass. As transparent conductive oxide (TCO), aluminum doped zinc oxide (ZnO:Al) was deposited by rf-magnetron sputtering; for a detailed description of the process see [158]. To avoid contamination the deposition of the p, i, n layers took place in designated chambers of a PECVD system. The p-layer was prepared in the highly crystalline growth regime (SC=1.5%) with a thickness of d=30 nm. Doping was achieved by adding trimethylboron (TMB - B(CH<sub>3</sub>)<sub>3</sub>) to the silane-hydrogen gas mixture. To avoid contamination of the i-chamber after deposition of the p-layer, the pchamber was purged with argon for 5 minutes and afterwards pumped below a pressure of  $p < 2 \times 10^{-8}$  mbar before the substrate was transferred. The intrinsic  $\mu$ c-Si:H layers were prepared using a silane-hydrogen mixture of SC=5-6%. Several diodes with varying i-layer thicknesses in the range between  $d=2 \mu m$  and  $d=6.5 \mu m$  were prepared. After the deposition of the i-layer, the chamber was again purged with argon and pumped to a pressure of  $p < 2 \times 10^{-8}$  mbar before the specimen was transferred into a n-chamber and a d=30 nm n-layer was deposited on top of the structure. The n-layer was amorphous silicon a-Si:H(P) where phosphine was used as doping gas. As contacts RF-magnetron sputtered ZnO:Al dots with diameters between 1-2 mm and a thicknesses of d=100 nm were used. After deposition, the top surface of these structures were plasma-etched (SF<sub>6</sub>-gas process), in order to remove the n-layer from regions not under the ZnO:Al.

Solar cell "sister" samples were prepared in the same run as the diodes used for the TOF measurements. Here the ZnO:Al on top of the n-layer was replaced by a silver (Ag) back reflector. These structures showed lower power conversion efficiencies compared to the best solar cells obtained for this material [159]. The lower conversion efficiencies are due to a decrease in short circuit current density  $J_{SC}$  by the smooth TCO as front contact and the choice of the back-reflector.

# **Chapter 4**

# **Intrinsic Microcrystalline Silicon**

The relation between the structure properties, in particular the ratio between crystalline and amorphous volume content, and the electronic properties of the material is of great interest. Especially since it has been shown, that contrary to what one might expect, material prepared close to the transition to amorphous growth yields the highest solar cell conversion efficiencies, rather than material with the largest crystalline grain size and the highest crystalline volume fractions. In this Chapter, paramagnetic states found in intrinsic  $\mu$ c-Si:H are identified and correlated to the structure properties of the material. ESR measurements, on intrinsic  $\mu$ c-Si:H prepared by HWCVD under various deposition conditions leading to material with structure compositions varying from highly crystalline to fully amorphous are described. Additionally, data from a PECVD series prepared and studied by Baia Neto et al. [17, 18, 160] is reanalyzed and compared with results obtained for the HWCVD material.

# 4.1 Raman Spectroscopy

In Fig. 4.1 Raman spectra of  $\mu$ c-Si:H prepared on different substrates are shown. The silane concentration  $SC=[SiH_4]/([H_2]+[SiH_4])$  was chosen to result in (a) highly crystalline material and (b) material at the transition between crystalline and amorphous growth. With increasing SC the amorphous phase content in the film increases, resulting in an increasing contribution of the amorphous signal in the Raman spectra around  $480 \text{ cm}^{-1}$ . While the highly crystalline material, shown in panel (a), shows no difference in the spectra of films prepared on glass or aluminum, the structure of the material prepared at the transition between crystalline and amorphous growth depends strongly on the substrate used (see panel (b)). Material deposited on glass substrates shows a much stronger contribution of the amorphous peak than that deposited on aluminum. This substrate dependence has

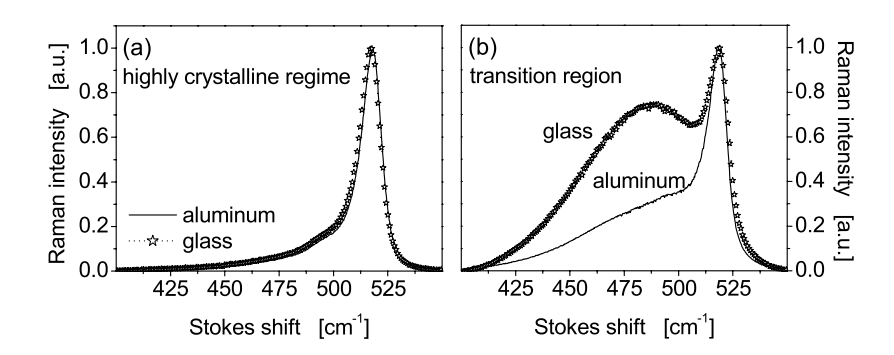


**Figure 4.1:** Raman spectra of material prepared on different substrates under deposition conditions resulting (a) in highly crystalline material and (b) material at the transition between crystalline and amorphous growth.

to be kept in mind, as in the following chapters conductivity measurements are compared with results obtained from ESR, for which glass and aluminum substrates have been used. In particular, a comparison of material properties near the transition between microcrystalline and amorphous growth has to be made carefully.

The structural properties of the deposited films are not determined solely by the silane concentration and the substrate. In Fig. 4.2 the Raman intensity ration  $I_C^{RS}$ , determined as described in section 3.1.1, is shown as a function of SC for a number of samples prepared with (a) PECVD (taken from reference [160]) and (b) HWCVD prepared at different substrate temperatures ranging from  $T_S = 185$ °C to  $T_S = 450$ °C. For all series, the silane concentration was varied covering the complete range from highly crystalline to predominately amorphous growth. Except for the HW material prepared at  $T_S = 450$ °C, for which glass substrates were used, all spectra were taken from material deposited on aluminum substrates. Independent of the particular deposition parameter or deposition process, one observes a decrease of  $I_C^{RS}$  with increasing SC. The qualitative behavior upon changes of SC are the same and is discussed for the VHF material, plotted in Fig. 4.2 (a). Between SC = 2 - 4%,  $I_C^{RS}$  decreases only slightly, from 0.80 to 0.74, indicating a highly crystalline structure. Above SC = 4% an increasing amorphous phase content results in a decreasing  $I_C^{RS}$  and for silane concentrations higher than 7% only an emorphous phase contribution can be observed in the Rehigher than 7% only an amorphous phase contribution can be observed in the Raman signal. The region SC = 4% - 7% is referred to as the transition zone. Within this regime of deposition parameters, the material structure changes from crystalline to predominately amorphous. The position and width of the zone strongly depends on the deposition parameters used, e.g. the substrate temperature during

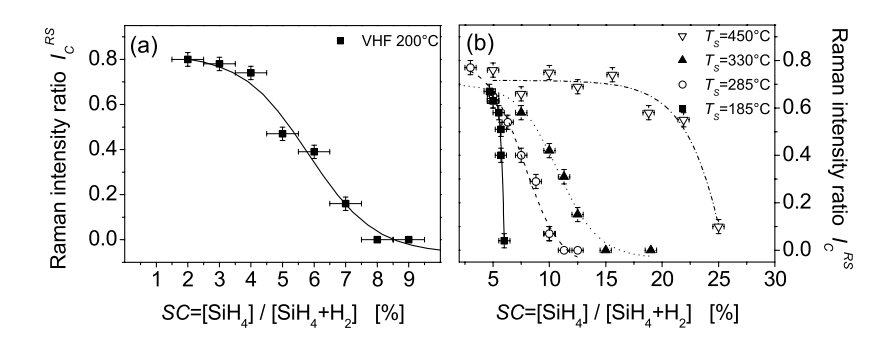


**Figure 4.2:** Raman intensity ratio of (a) VHF-PECVD material and (b) HWCVD-material deposited at different substrate temperatures ranging from  $T_S = 185^{\circ}C$  to  $T_S = 450^{\circ}C$  taken from reference [17, 18, 160] and [13], respectively.

the process plays an important role for the structural development of the films. This is shown in Fig. 4.2 (b), where the  $I_C^{RS}$  of HW-material prepared at different  $T_S$  is shown. An increasing  $T_S$  leads to a shift of the transition to higher values of SC. The dependency on  $T_S$  has been also observed for PECVD material [161].

The observed shifts of the transition under different deposition conditions make it difficult to use the silane concentration as a single parameter to predict the electronic properties of samples prepared under different conditions. Even material prepared in the same run, but on different substrates, may show different properties. Therefore, in the following sections the Raman intensity ratio  $I_C^{RS}$ , rather than SC, will be used to compare electronic properties of different samples.

### 4.2 Electrical Conductivity

Within this section, a short review of the conductivity data of both the PECVD and the HWCVD material taken from references [17] and [13], respectively, will be given. These results are of particular importance for the following Chapters and will therefore briefly be reviewed in this context.

The transition in growth is directly reflected in the conductivity as shown in Fig. 4.3. Here, results of dark conductivity  $\sigma_D$  measurements are plotted versus the Raman intensity ratio  $I_C^{RS}$  for material prepared using (a) VHF-PECVD and (b) HWCVD. Plotting  $\sigma_d$  versus  $I_C^{RS}$  has recently become a widely used method to compare material prepared under different deposition conditions and in different systems (see e.g. [16, 13]). All samples show the same general dependent

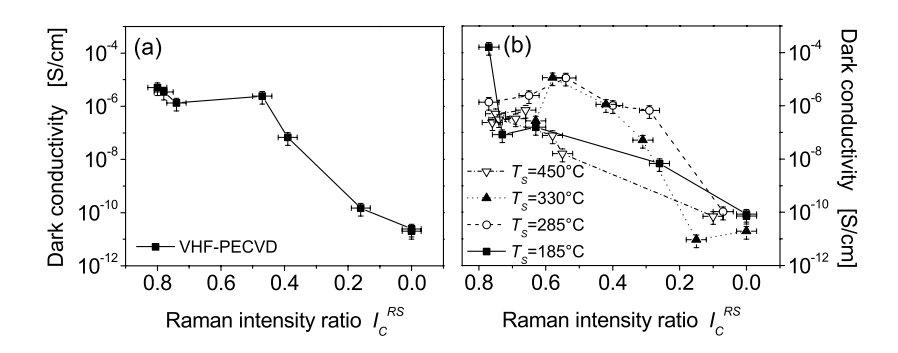


**Figure 4.3:** Dark conductivity  $\sigma_D$  as a function of  $I_C^{RS}$  of material prepared with (a) VHF-PECVD and (b) HWCVD at various substrate temperatures, taken from reference [17, 18] and [13], respectively.

dency of  $\sigma_D$  upon  $I_C^{RS}$ . Material prepared in the crystalline growth regime shows a dark conductivity of  $10^{-4}$  to  $10^{-7}$  S/cm, which is of the same order of magnitude as observed for crystalline silicon. However, in c-Si the electron mobilities ( $\mu \approx 1500~\text{cm}^2/\text{Vs}$  [91]) exceed by far the electron mobilities in  $\mu$ c-Si:H (a few cm²/Vs [49]). This suggests a considerable background doping in intentionally undoped  $\mu$ c-Si:H. As a consequence of the structural transition, for material with an  $I_C^{RS}$  lower than 0.4  $\sigma_D$  decreases by several orders of magnitude, resulting in values below  $10^{-10}$  S/cm, which is typical for a-Si:H [65]. When comparing material prepared in the transition regime, the drop in  $\sigma_D$  occurs at slightly higher values of  $I_C^{RS}$  for the material prepared with PECVD compared to that prepared with HWCVD. For material prepared with HWCVD one observes subsequent lower values of the conductivity for substrate temperatures of  $T_S = 450^{\circ}\text{C}$  and  $185^{\circ}\text{C}$ . Anticipating results obtained in the next section, the low  $\sigma_D$  of the  $T_S = 450^{\circ}\text{C}$  material can be explained by a high defect density. On the other hand, the  $T_S = 185^{\circ}\text{C}$  material shows very low spin density. The low values of  $\sigma_D$  might therefore be a result of a reduced impurity level or reduced mobility caused by grain boundary effects.

# 4.3 ESR Signals and Paramagnetic States in Intrinsic $\mu$ c-Si:H

ESR measurements were performed on powdered material deposited on aluminum substrates. Details of the powder preparation process can be found in section 3.3.1.

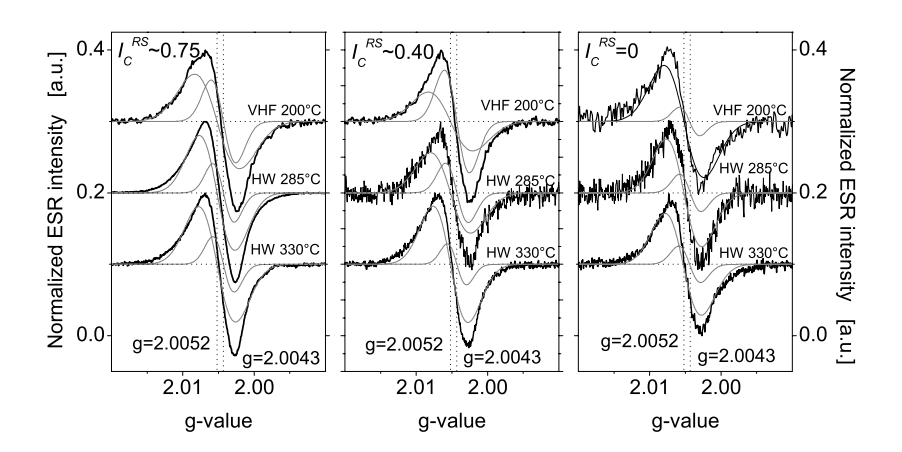


**Figure 4.4:** Typical ESR spectra of VHF-PECVD and HWCVD material with structure compositions varying from highly crystalline ( $I_C^{RS} \approx 0.75$ ) to fully amorphous ( $I_C^{RS} \approx 0$ ). The discrepancy for the crystalline HW-material is a result of post-oxidation of these highly porous structures. A detailed study of these effects can be found in Chapter 6.

Fig. 4.4 shows typical ESR spectra taken on material with different crystallinity prepared with VHF-PECVD and HWCVD. The structure varies from highly crystalline ( $I_C^{RS} \approx 0.75$ ) to material at the transition between crystalline and amorphous growth ( $I_C^{RS} \approx 0.4$ ) and finally to material which shows no contribution of the crystalline phase in the Raman spectra ( $I_C^{RS} = 0$ ). All spectra show the typical asymmetric line shape with contributions at g=2.0043 and g=2.0052, in the following denoted as db<sub>1</sub> and db<sub>2</sub>, respectively. Numerical fits to the measured data are included in the graphs, as gray lines. Interestingly, the line width of the two resonances changes only little upon different structure compositions and the width is also similar for material prepared with either PECVD or HWCVD. Optimum fits of the superimposed lines could be performed using Gaussian lines with line widths of  $\Delta H_{pp} = 5.6 \pm 0.3$  G for the db<sub>1</sub> and  $\Delta H_{pp} = 9.7 \pm 0.5$  G for the db<sub>2</sub> resonance. However, while these fits work perfectly for the PECVD material, some deviations can be observed for the HWCVD material. In particular, at the high g-value site of the spectra, the two resonances does not fit the spectra correctly. This is a result of post-oxidation of these highly porous structures and will be extensively studied in Chapter 6.

Looking at the VHF-PECVD material (uppermost spectra), one observes that for the highly crystalline material the spectrum is dominated by the db<sub>2</sub> resonance, while for material prepared at the  $\mu$ c-Si:H/a-Si:H transition with  $I_C^{RS} \approx 0.40$  the resonance at g=2.0043 contributes much more to the overall ESR signal, resulting

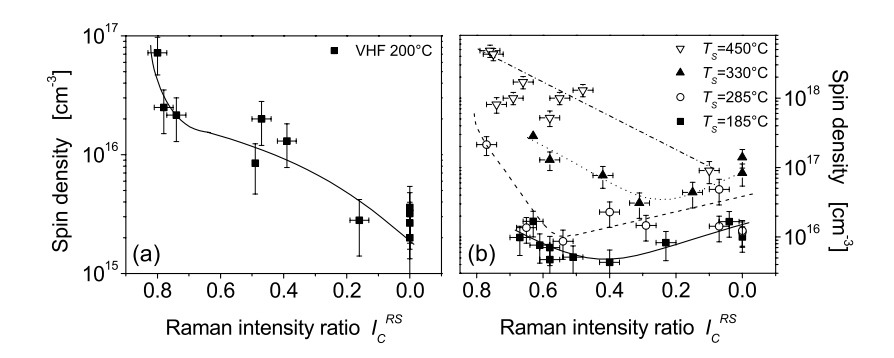


**Figure 4.5:** Spin density as a function of  $I_C^{RS}$  for  $\mu$ c-Si:H prepared with (a) VHF-PECVD and (b) HWCVD deposited at various substrate temperatures. The values for the VHF-PECVD material were taken from reference [17].

in a shift of the average g-value<sup>1</sup> with respect to lower values. For material with no discernable crystalline signal in the Raman spectra ( $I_C^{RS}=0$ , right panel), the g-value shifts to higher values, however, without reaching the value of g=2.0055 characteristically observed in a-Si:H. The signal is clearly dominated by the resonance at g=2.0052. The same trend can be also observed for the HW material prepared at  $T_S=285^{\circ}\mathrm{C}$  (see Fig. 4.4). For the highly crystalline and amorphous material the spectra are dominated by the db<sub>2</sub> resonance at g=2.0052, while for the material at the  $\mu$ c-Si:H/a-Si:H transition an increasing contribution of the db<sub>1</sub> line can be observed. Material prepared at substrate temperatures as high as  $T_S=330^{\circ}\mathrm{C}$ , regardless of the structure composition all spectra are dominated by the db<sub>2</sub> resonance. It is important to note, that for a fixed  $I_C^{RS}$  the increasing contribution of the db<sub>2</sub> resonance goes along with an increasing overall spin density  $N_S$ . This issue will be discussed in more detail below.

The spin density  $N_S$  obtained from numerical integration of the ESR spectra is plotted in Fig. 4.5 versus the Raman crystallinity  $I_C^{RS}$ . Remarkably, independent of the deposition technique and deposition conditions used, the highest spin densities are always observed for the material with the highest crystallinity. For the VHF-PECVD material, plotted in Fig. 4.5 (a),  $N_S$  decreases slightly between  $I_C^{RS} = 0.78$  and 0.39. At the highest crystallinity,  $N_S$  increases steeply from  $2.5 \times 10^{16}$  cm<sup>-3</sup> at  $I_C^{RS} = 0.78$  to values of  $7.2 \times 10^{16}$  cm<sup>-3</sup> at  $I_C^{RS} = 0.80$ . Beyond the transition to amorphous growth ( $I_C^{RS} < 0.39$ ), the spin density drops further down by one order of magnitude to values as low as  $2 \times 10^{15}$  cm<sup>-3</sup>.

<sup>&</sup>lt;sup>1</sup>The average g-value is defined as the zero-crossing of the ESR signal.

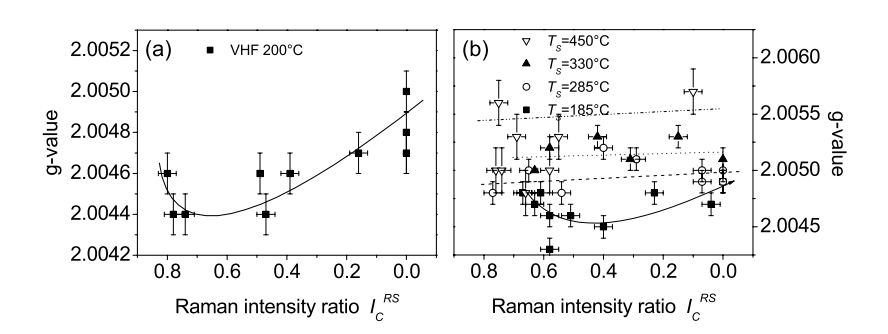


**Figure 4.6:** *g*-values as a function of  $I_C^{RS}$  of material prepared (a) VHF-PECVD and (b) HWCVD deposited at various substrate temperatures. The values for the VHF-PECVD material were taken from reference [17].

For the HWCVD material, again the highest  $N_S$  is always found for material with the highest crystallinity. Within the crystalline regime, the spin density decreases considerably with increasing amorphous content for all substrate temperatures  $T_S$ . For material dominated by amorphous phase content ( $I_C^{RS} < 0.4$ ), the spin density increases, rather than staying constant or decreasing as observed for the PECVD material. Only for the highest  $T_S$  of 450°C the spin density decreases monotonously, however at very high values of  $N_S > 10^{17}$  cm<sup>-3</sup>. Finally, independent of the particular structure composition,  $N_S$  increases significantly when the substrate temperature is increased by up to three orders of magnitude for  $I_C^{RS} \approx 0.5$ . It is important to note that the lowest spin densities of  $N_S = 4 \times 10^{15}$  cm<sup>-3</sup> are observed for material prepared at  $T_S = 185$ °C and a crystalline volume fraction of  $I_C^{RS} \approx 0.4$ , and that solar cells prepared under similar conditions have shown maximum efficiencies of  $\eta = 9.4\%$  [162].

The corresponding average g-values are plotted versus  $I_C^{RS}$  in Fig. 4.6. For the PECVD material shown in Fig. 4.6 (a), the average g-value shifts from a value of 2.0043 to 2.0051, when going from crystalline to amorphous structure. This means that with increasing amorphous content the g-value is clearly shifted to higher values, however without reaching the value of 2.0055 usually found in a-Si:H. As shown in Fig. 4.6 (b), the g-values for material prepared with HWCVD are generally higher (note the different scaling of the y-axis in panels (a) and (b)). The variations as a function of structure are considerably less for the HW-material. Again, even for material with no contribution of the crystalline phase in the Raman signal, the g-values do not reach the typical value of 2.0055 found in a-Si:H. Generally, one observes an increasing g-value for increasing substrate temperature over the entire range of  $I_C^{RS}$ .

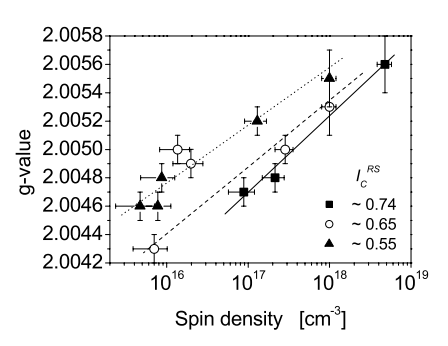


**Figure 4.7:** *g*-value vs. spin density  $N_S$  of material prepared with HWCVD for three structure compositions ranging from highly crystalline to transition material. The data are taken from Fig. 4.5 (b) and 4.6 (b).

Comparing Fig. 4.5 (b) and Fig. 4.6 (b), one can observe that both  $N_S$  and the g-value increase with increasing substrate temperature  $T_S$ . In Fig. 4.7 the gvalue is plotted versus  $N_S$  for three different structure compositions, ranging from highly crystalline to material prepared close to the transition between microcrystalline and amorphous growth. The values of  $N_S$  and g were taken from Fig. 4.5 and 4.6, respectively; the data points in Fig. 4.8 therefore correspond to material prepared at different substrate temperatures. Although there is some scatter of the data for the  $I_C^{RS} \approx 0.65$  material, there is a clear correlation between this two quantities: For increasing spin density the g-value is clearly shifted to higher values. This can be observed for all structure compositions between  $I_C^{RS} = 0.74$ and 0.55. Assuming that within the crystalline regime the ESR signal is a composition of only two resonances at g=2.0043 and g=2.0052, the shift of the average g-value is a result of a change in the ratio of these contributions. This of course also assumes that the g-value of each line does not shift for different deposition conditions, which is a rather strong postulation. Keeping this in mind, the results indicate that the increasing spin density  $N_S$ , as a function of increasing  $T_S$ , is caused by an increasing number of paramagnetic states that belong to the db<sub>2</sub> resonance.

The fact that high quality  $\mu$ c-Si:H material with no discernable crystalline signal in the Raman signal does not show the typical a-Si:H g-value of 2.0055 was a little puzzling. Material has therefore been prepared with even higher silane concentrations ranging from SC = 9% to 100% using VHF-PECVD. Spin densities and g-values measured for this material are plotted in Fig. 4.8 along with the

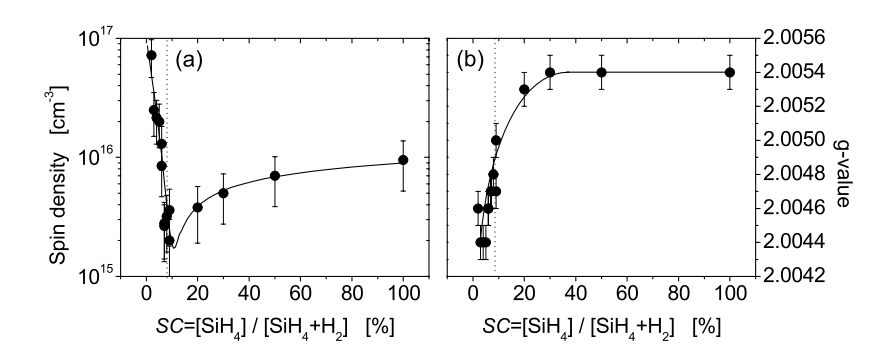


**Figure 4.8:** (a) Spin density and (b) g-value of material prepared by VHF-PECVD varying the silane concentration in the range between SC = 2 - 100%.

values previously plotted in Fig. 4.5 (a) and Fig. 4.6 (a). The dotted vertical line indicates the threshold to fully amorphous growth. For SC higher than this value, the Raman spectra show no contribution of the crystalline signal on both, material prepared on aluminum and glass substrates. As shown before, the spin density decreases monotonously between SC = 2 and 9% from  $N_S = 7.2 \times 10^{16}$  cm<sup>-3</sup> to very low values of  $N_S = 2 \times 10^{15}$  cm<sup>-3</sup>. With increasing silane concentration  $N_S$  increases again reaching a value of  $1 \times 10^{16}$  cm<sup>-3</sup> for a source gas mixture containing only SiH<sub>4</sub>, which is a typical value for high quality amorphous silicon [65]. Far more interesting is the development of the g-value shown in Fig. 4.8 (b). Right beyond the transition, although no contribution of a crystalline signal can be observed in the Raman spectra, the g-value is still at low values of g=2.0050. A further increased silane concentration then leads to a shift of the g-value towards g=2.0054 typically observed for a-Si:H.

# **4.4** Discussion - Relation between ESR- and Structural Properties

Independent of the particular deposition process, VHF-PECVD or HWCVD, the ESR signal of intrinsic  $\mu$ c-Si:H shows an asymmetric line, which could be well fitted by two Gaussian contributions, db<sub>1</sub> and db<sub>2</sub>, at g=2.0043 and g=2.0052 with line widths of  $\Delta H_{pp} = 5.6 \pm 0.3$  and  $\Delta H_{pp} = 9.7 \pm 0.5$  G, respectively. For structure compositions of the full range, from highly crystalline to fully amorphous, the highest spin densities  $N_S$  are always observed for material with the highest crystallinity, while an increasing amorphous content leads to a decreasing num-

ber of paramagnetic states. This also applies for the substrate temperature  $T_S$ , where an increasing  $T_S$  results in an increasing  $N_S$ . Interestingly, an increasing spin density also leads to a shift of the average g-value with respect to higher values, as has been shown in Fig. 4.6. As the ESR signal of  $\mu$ c-Si:H generally can be deconvoluted into two contributions  $db_1$  and  $db_2$ , it is tempting to relate the shift of the average g-value to variations of the intensity ratio of these two signals. Whereas the ESR spectra of highly crystalline, but well passivated material is dominated by the  $db_1$  resonance, additional defects result in the  $db_2$  resonance at g=2.0052 (compare also Fig. 4.4). On the other hand, an increasing amorphous phase content leads to a higher contribution of the  $db_2$  resonance to the overall signal. Interestingly, the peak to peak line width  $\Delta H_{pp}$  of the individual signals  $(db_1, db_2)$  changes only little upon variations of the defect density or the structure composition. If the line width is dominated by inhomogeneous broadening, i.e. disorder effects, this suggests little variation of the local disorder surrounding the DB-defects, for the various samples investigated.

There is still no conclusive evidence on what is the origin of the resonances db<sub>1</sub> (g=2.0043) and db<sub>2</sub> (g=2.0052), typically found in  $\mu$ c-Si:H. The particular structure of  $\mu$ c-Si:H allows for a number of places where dangling bond defects are possibly located: the crystalline regions; the grain boundaries; the amorphous phase or in connection with impurity atoms, e.g. oxygen. However, some conclusions can be drawn from these results. Assuming that the two resonances are the result of two independent states, which is not yet proven, the contribution of  $db_2$  resonance increases upon increasing  $T_S$  and amorphous phase content. Over this wide range of samples, the line width  $\Delta H_{pp}$  remains fairly constant at values of  $\Delta H_{pp} = 9.7 \pm 0.5$  G, which is close to the value of  $\Delta H_{pp} \approx 10$  G found in a-Si:H [85]. However, because of the two facts that (i) the overall  $N_S$  strongly decreases with increasing amorphous content and (ii) poor passivated highly crystalline material with no amorphous phase content is also dominated by the resonance at g=2.0052, it seems unlikely that the amorphous phase itself is the origin of the paramagnetic states. More likely, the defects are located at grain boundaries, whether on the crystalline grains forming the columnar structures or at the outside of the columns. From X-ray analysis one derives typical sizes of the crystalline grains between 4 – 20 nm [58]. Assuming an average size of a coherent region of 12 nm edge length, cubic grains, and a sample average spin density of  $N_S = 2 \times 10^{16} \text{ cm}^{-3}$ , there is only one defect per 30 grains. This is in agreement with the fact that the small crystalline grains are separated from each other by twin boundaries and stacking faults, which are known to preserve the local tetrahedral coordination and are not expected to lead to paramagnetic defects. It seems therefore more likely that the defects are located at the boundaries of the columnar clusters, as has been suggested before [161].

This is supported by the ESR data obtained for different substrate tempera-

tures. As observed in Fig. 4.5 (b),  $N_S$  increases as a function of  $T_S$ , independent of the structure composition. Infrared studies have shown that with increasing  $T_S$ , the amount of hydrogen incorporated in the material decreases significantly [13], which can be ascribed to an aggravated desorption of hydrogen during the growth process. The increasing  $N_S$ , which is accompanied by a shift of g to higher values, indicates that the increasing spin density is associated with an increasing number of db<sub>2</sub> states. Because the bonded hydrogen is located mainly at the column boundaries, which passivates dangling bonds, one can conclude that the desorption leads to un-terminated db<sub>2</sub> states residing at the column boundaries.

The question whether the ESR signal for both materials, prepared at high  $T_S$  or high amorphous phase content, is a result of the same paramagnetic states cannot be decided. In this context it is interesting that even fully amorphous material prepared at the microcrystalline/amorphous transition shows the resonance at g=2.0052, rather than the expected value of g=2.0055. Also, the observed line width of the  $db_2$  resonance is essentially the same as observed in the highly crystalline regime. The differences of the g-value, compared to that observed in a-Si:H might be a result of a different medium range order in this so-called "polymorphous", "protocrystalline", or "edge-material" [163]. Speculatively, one might conclude that the degree of disorder around the defects is comparable to that found around the paramagnetic states located at the column boundaries. To answer this question remains a challenge for future investigations.

Similarly to a-Si:H, in the microcrystalline regime ( $I_C^{RS} = 0.85 - 0.4$ ), the observed spin density correlates nicely with the energy conversion efficiency of the solar cells, containing the same absorber layer. Independent of the particular deposition process, it was found that not, as one might have expected, material with the highest crystalline volume fractions, but material prepared close to the transition to amorphous growth yields the highest solar cell conversion efficiencies. The performance of the solar cell increases slightly with increasing amorphous content from  $I_C^{RS} = 0.71 - 0.5$ . On the other hand, material with the highest crystalline volume fraction leads to very poor conversion efficiencies. Apparently, the highest crystallinity and the largest grain size is only obtained at the cost of a poor defect passivation. By contrast, the increasing amorphous phase content incorporated between the crystalline columns, is a highly efficient passivation layer and the increasing hydrogen content leads to a better termination of surface states. A critical relation between  $N_S$  and solar cell performance is also found for the variation of the substrate temperature. Again, material which shows the highest solar cell conversion efficiency is found to have the lowest spin density. It is likely, that the optimum of  $T_S$  is because of this hydrogen desorption problem, just as for a-Si:H deposition.

# 4.5 Summary

In the previous section, the results of the study on paramagnetic defects in undoped  $\mu$ c-Si:H were presented. For structure compositions ranging from highly crystalline to fully amorphous, the highest  $N_S$  is always found for material with the highest  $I_C^{RS}$ . While the preparation within this regime leads to the highest crystallinity and the largest grain sizes, this can be achieved only at the cost of a poor defect passivation. The increasing SC during the process leads to a better termination of the surface states caused by the increasing hydrogen content. On the other hand, additional amorphous phase content, incorporated between the crystalline columns, acts as a passivation layer and leads to a better termination of surface states. Very low  $N_S$  are found for material close to or beyond the transition to amorphous growth (see Fig. 4.5 (a)). For HWCVD material a strong dependence of the spin density  $N_S$  on the deposition temperature  $T_S$  was found. Generally, the increasing spin density, caused by either low SC or high  $T_S$  during the deposition process leads to an increasing contribution of the db2 resonance. On the other hand, the g-value shifts to higher values with increasing amorphous content. Surprisingly, even material prepared close to the structural transition, with no discernable crystalline signal in the Raman spectra, does not show the typical a-Si:H value of g=2.0055. In fact, the ESR signal is clearly dominated by the resonance at g=2.0052. Only for material prepared at yet higher silane concentrations can g=2.0055 be detected (see Fig. 4.8). Whether the differences of the g-value compared to that observed in a-Si:H are the result of a different medium range order [61] cannot be determined from these data and remains e a task for future investigation. A detailed study of material prepared at transition between microcrystalline and amorphous growth using TEM and ESR, could provide further information on how changes of the structure, in particular the medium range order, affect the position of the resonance line observed in ESR. This might also provide further details concerning the nature of defects in  $\mu$ c-Si:H.

# Chapter 5

# N-Type Doped $\mu$ c-Si:H

In section 4 results of intrinsic films of  $\mu$ c-Si:H with a systematic variation of material structure ranging from highly crystalline to amorphous growth were shown. ESR measurements have been used to determine the spin density  $N_S$ . However, from these investigations it is not clear how far  $N_S$  correlates with the defect density in the material and if the spin density  $N_S$  is a measure of the real defect density  $N_{DB}$ . This is the subject of the following section.

For this purpose, material prepared with different  $SC = [SiH_4]/([H_2] + [SiH_4])$  and phosphorous doping levels  $PC = [PH_3]/([PH_3] + [SiH_4])$  will be studied. The silane concentration was varied in the range from SC = 2% to 8%, resulting in structure compositions comparable to those studied in Chapter 4. The doping concentrations PC of 1, 5, and 10 ppm were chosen to be of the order of the intrinsic spin density  $N_S$  (see Fig. 4.5 (a)). To study effects of doping on the position of the Fermi level and the occupation of defect states, electrical dark conductivity  $\sigma_D$  and ESR measurements have been performed.

## 5.1 Structure Characterization

In order to obtain a measure of the crystalline volume content, Raman spectra were recorded on both glass and aluminum substrates. The results are summarized in Fig. 5.1 (a), showing the Raman intensity ratio  $I_C^{RS}$  plotted versus the silane concentration SC. For doping concentrations in the range of 1-10 ppm the transition from highly crystalline to predominantly amorphous growth can be observed. In the highly crystalline growth regime between SC=2% and 5%, the Raman intensity ratio decreases only slightly from  $I_C^{RS}=0.85$  to 0.74 and the spectra are dominated by the crystalline signal. Above SC=5% the transition to amorphous growth can be observed. An increasing amorphous phase contribution results in a fairly steep decrease of  $I_C^{RS}$  between SC=5% and 5%. For silane concentra-

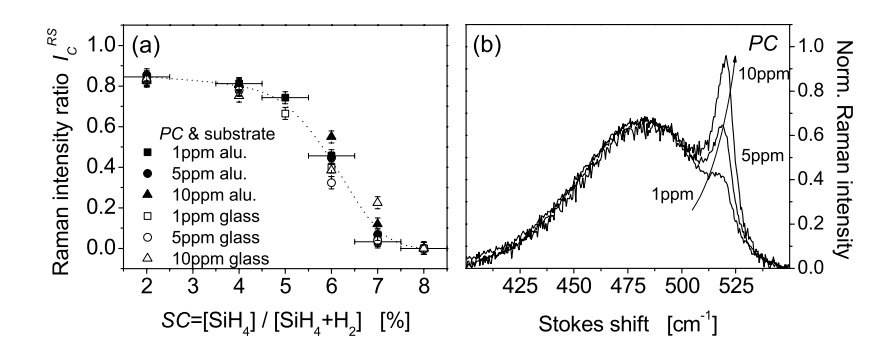


**Figure 5.1:** (a) Raman intensity ratio ( $I_C^{RS}$ ) for samples deposited on aluminum (closed symbols) and glass (open symbols). (b) Raman spectra of  $\mu$ c-Si:H prepared at SC = 7% with varying doping concentrations of PC = 1, 5, and 10 ppm). With increasing doping concentration the crystallinity increases.

tions higher than SC=7% the Raman spectra show only the amorphous peak at  $480~\rm cm^{-1}$ . Comparing samples deposited on glass and aluminum, the well known substrate dependence on the material structure can be observed (compare with Fig. 4.1). Samples deposited on glass in general show a higher amorphous phase contribution and therefore a smaller value of  $I_C^{RS}$  compared to material deposited on aluminum.

This has to be kept in mind as in the following section results from conductivity measurements as well as ESR measurements will be compared, where glass and aluminum substrates were used, respectively. Also with increasing doping concentration PC the Raman intensity ratio increases. This is shown in Fig. 5.1 (b), where for a given silane concentration SC the crystallinity increases with increasing doping concentration.

## 5.2 Electrical Conductivity

Conductivity measurements, as described in section 3.1.3, were performed on films deposited on glass substrates. The results are shown in Fig. 5.2 (a), where the dark conductivities  $\sigma_D$  of phosphorous doped material with PC=1,5, and 10 ppm are plotted together with conductivity data of undoped material taken from reference [18]. For the undoped material the conductivity  $\sigma_D$  decreases only slightly between  $I_C^{RS}=0.82$  and 0.47. As a consequence of the structural transition, for material with an  $I_C^{RS}$  lower than 0.4  $\sigma_D$  decreases by several orders of magnitude, resulting in values below  $10^{-10}$  S/cm typical for a-Si:H [65]. Doping effects can

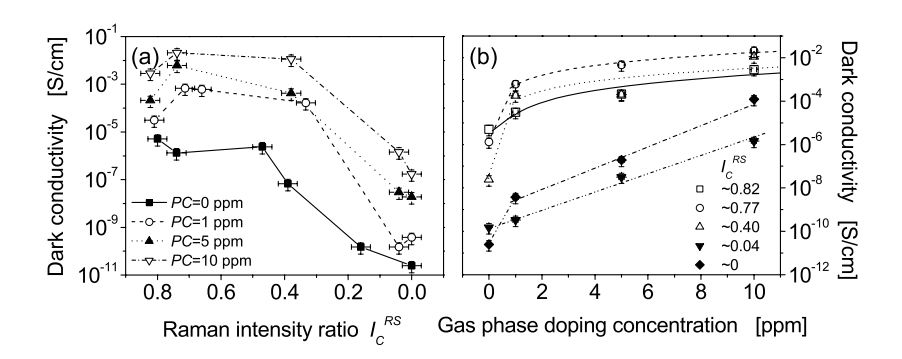


Figure 5.2: Room temperature conductivity  $\sigma_D$  of  $\mu$ c-Si:H films with doping concentrations of 0 ppm ( $\blacksquare$ ), 1 ppm ( $\circ$ ), 5 ppm ( $\blacktriangle$ ) and 10 ppm ( $\triangledown$ ) as a function of (a) Raman intensity ratio ( $I_C^{RS}$ ) and (b) gas phase doping concentration. The data of the undoped material were taken from reference [18].

be observed for all structure compositions from highly crystalline to amorphous. However, unlike the undoped material for the n-type doped samples the highest  $\sigma_D$  values are not found for the samples with the highest crystallinity. In fact, for all doping concentrations PC=1-10 ppm an increase of  $\sigma_D$  by more than one order of magnitude can be observed if the crystallinity decreases from  $I_C^{RS}=0.82$  to 0.77. This indicates that the doping induced free charge carrier concentration is considerably less for the highly crystalline material. Between  $I_C^{RS}=0.77$  and 0.4  $\sigma_D$  stays almost constant before it drops down by about 5 orders of magnitude as result of the structural transition to predominantly amorphous growth, independent of the particular doping concentration.

In Fig. 5.2 (b) the conductivity is plotted versus the gas phase doping concentration PC. In these plots the correlation between doping and conductivity becomes more obvious. Within the microcrystalline growth regime between  $I_C^{RS} \sim 0.82-0.40$  (upper three curves in the figure) the doping induced changes of  $\sigma_D$  are highest for samples with  $I_C^{RS} \sim 0.77$  and 0.4 and considerably less for the sample with the highest crystallinity. Applying a doping concentration of PC = 1 ppm, the dark conductivity of the  $I_C^{RS} = 0.77$  and  $I_C^{RS} = 0.4$  material changes by more than three orders of magnitude, compared to the undoped material. On the other hand, for the highest crystallinity, where the highest  $N_S$  is observed in the undoped material,  $\sigma_D$  increases by only a factor of 6. Plotting  $\sigma_D$  on a linear scale, one observes that for doping concentrations higher than PC = 1 ppm all microcrystalline samples ( $I_C^{RS} = 0.82 - 0.4$ ) show an almost linear increase of the conductivity with a structure independent slope. For amorphous or almost

amorphous samples ( $I_C^{RS}=0.04$  to 0) the dark conductivity shows much lower values over the whole doping range investigated. However, for the  $I_C^{RS}=0.04$  material  $\sigma_D$  increases exponentially by about 4 orders of magnitude, while for the fully amorphous material  $\sigma_D$  changes by almost 7 orders of magnitude from  $\sigma_D=2\times 10^{-11}$  S/cm to  $1\times 10^{-4}$  S/cm.

The dark conductivity follows nicely the expected behavior. Considering the characteristic of the spin density of the undoped material (see Fig. 4.5 (a)), the results are in agreement with the proposed doping mechanism of compensation of gap states as described in section 2.2.2. Doping induced changes are highest for material for which low spin densities are found in the undoped state. For highly crystalline material, which also exhibits the highest spin densities, the doping induced changes are considerably less, as more defect states have to be compensated before the Fermi level moves up into the conduction band-tail.

## 5.3 ESR Spectra

Samples prepared for ESR measurements have been deposited on aluminum substrates in the same run as that used for conductivity measurements. The material was then powdered using the procedure described in section 3.3.1. ESR measurements were performed at a temperature of  $T=40\mathrm{K}$ . All spectra were normalized to the same peak height and plotted in Fig. 5.3. Fig. 5.3 shows stack plots of samples with different crystallinity ranging from  $I_C^{RS}=0.82-0$  and doping concentrations of 1, 5, 10 ppm. The fact that the Raman intensity ratio for the predominantly amorphous material  $I_C^{RS}=0.08$  deviates slightly from that found in Fig. 5.2 ( $I_C^{RS}=0.04$ ) is a direct result of the substrate dependence. The vertical dotted lines in Fig. 5.3 indicate the resonances at g=2.0043, g=2.0052, and g=1.996-1.998, typically found in  $\mu$ c-Si:H (see section 2.2.2).

All spectra show contributions of the three well-known signals at g-values of 2.0043 (db<sub>1</sub>), 2.0052 (db<sub>2</sub>), and g=1.996-1.998 (CE) (for details see section 2.2.2), except for the spectra taken from the purely amorphous material ( $I_C^{RS} = 0$ ). Quite surprisingly, the CE resonance can be observed in all spectra of the doped samples, in the highly crystalline material as well as in material where very little Raman intensity due to the crystalline phase is found ( $I_C^{RS} < 10\%$ ). Only samples with no detectable contribution from the crystalline volume to the Raman signal show only the dangling bond signal at g=2.0052. For a given doping level, the intensity of the CE-line is highest for highly crystalline material with an  $I_C^{RS}$  of 0.77 or 0.47. The CE line is much less pronounced for the highest crystallinity ( $I_C^{RS} = 0.82$ ), which is in agreement with the high spin densities found in this material (see Fig. 4.5 (a)). As expected, the intensity of the CE resonance increases

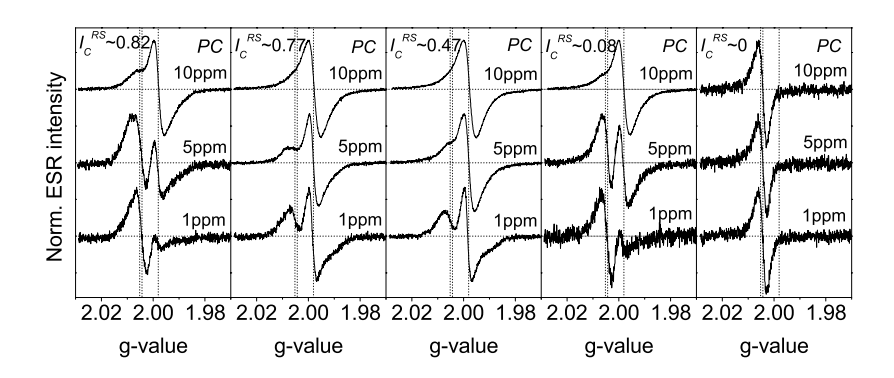


**Figure 5.3:** ESR spectra of samples with crystallinities of  $I_C^{RS} \approx 0.82$ , 0.72, 0.47, 0.08, and 0 with gas phase doping concentrations of PC = 1, 5, and 10 ppm measured at T = 40K. The vertical dotted lines indicate the position of db<sub>1</sub>, db<sub>2</sub>, and CE resonances at values of g = 2.0043, g = 2.0052, and g = 1.996-1.998, respectively, typically found in  $\mu$ c-Si:H.

with increasing doping level PC. In addition to the CE signal, the DB signal  $(db_1+db_2)$  is visible in all samples, although in the case in which the CE line is most dominating (e.g.  $I_C^{RS} = 0.77$  and with PC = 10 ppm) the DB signal is at the lower limit for a multi-peak de-convolution analysis to be feasible.

Doping induced effects can be observed in all spectra of material where a crystalline phase can be observed ( $I_C^{RS} > 0$ ). The existence of the resonance at g=1.996-1.998 is a direct result of a shift of  $E_F$  up into the conduction band-tail. With increasing doping concentration, more and more states in the conduction band-tail are getting occupied and contribute to the intensity of the resonance. The shift of the Fermi level, however, is governed by the compensation of gap states. For a fixed doping concentration, the high defect density in the  $I_C^{RS} \approx 0.82$  material leads to a considerable lower CE spin density  $N_{CE}$  compared to the low defect material  $I_C^{RS} \approx 0.77$  and 0.47. It is quite surprising, that even for material with crystalline grains that are highly diluted in an amorphous phase ( $I_C^{RS} \approx 0.08$ ) a strong CE line can be observed.

## 5.4 Dangling Bond Density

To obtain the spin density of each superimposed line shown in Fig. 5.3, a numerical fitting procedure was applied. The DB-signals at g=2.0043 and g=2.0052 could be well approximated by Gaussian lines. For the CE line at g=1.996-1.998 a convolution of a Gaussian and Lorentzian curve was used. However, a separa-

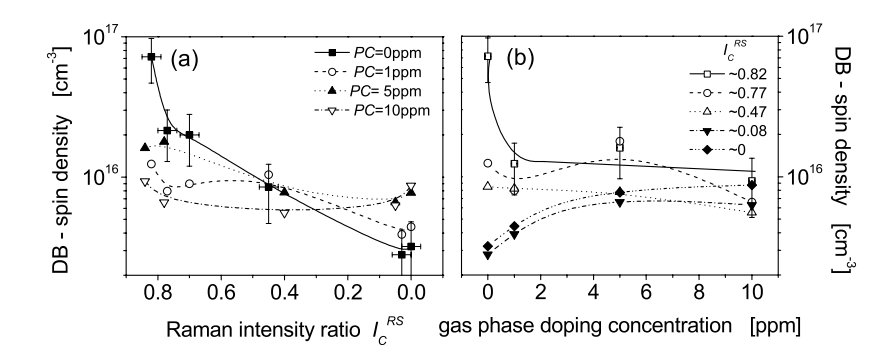


**Figure 5.4:** Dangling bond spin density versus  $I_C^{RS}$  obtained from numerical fitting of the ESR line shown in Fig. 5.3 (a) vs. the Raman intensity ratio  $I_C^{RS}$  and (b) vs. the gas phase doping concentration PC.

tion of the two DB signals is impossible from the spectra shown above; therefore only the sum of both will be analyzed in this section.

Fig. 5.4 (a) shows the dangling bond (DB) density obtained from this deconvolution procedure versus the Raman intensity ratio  $I_C^{RS}$ . Additionally, the DB density  $N_{DB}$  for the undoped material is shown. As already shown in Chapter 4 for the intrinsic material, the DB density  $N_{DB}$  decreases with increasing amorphous phase contribution. In principle one can observe the decrease of  $N_{DB}$  upon decreasing  $I_C^{RS}$  for all doping concentrations, but with increasing doping level this phenomena is less pronounced. It is surprising indeed that even for the highest doping concentrations of PC = 10 ppm, DB states can still be observed in all samples. However, depending on the crystallinity there are some distinct differences in how the dangling bond density  $N_{DB}$  changes as a function of PC. This is shown in Fig. 5.4 (b), where the spin density is plotted versus the gas phase doping concentration. For the highly crystalline sample ( $I_C^{RS} = 0.82$ ) the spin density decreases steeply from 0 ppm to 1 ppm and stays almost constant at  $N_{DB} \approx 10^{16} \, \mathrm{cm}^{-3}$  for higher doping concentrations. For the highly crystalline samples ( $I_C^{RS} = 0.77 - 0.47$ ) the spin density stays almost constant or slightly decreases from already low values of  $N_{DB} = 1 \times 10^{16}$  cm<sup>-3</sup> for PC = 0 ppm to  $N_{DB} = 6 \times 10^{15}$  ${\rm cm}^{-3}$  for PC=10 ppm. This is a result of compensation. For samples with an even higher amorphous phase contribution ( $I_C^{RS}$  < 0.10), an increasing dangling bond density can be observed. It seems unlikely that the reason for the increasing  $N_{DB}$  is caused by the doping induced dangling bond creation, known from hydrogenated amorphous silicon [89, 90], because these states can not be observed in ESR. It is more plausible that within the investigated doping range, the occupation

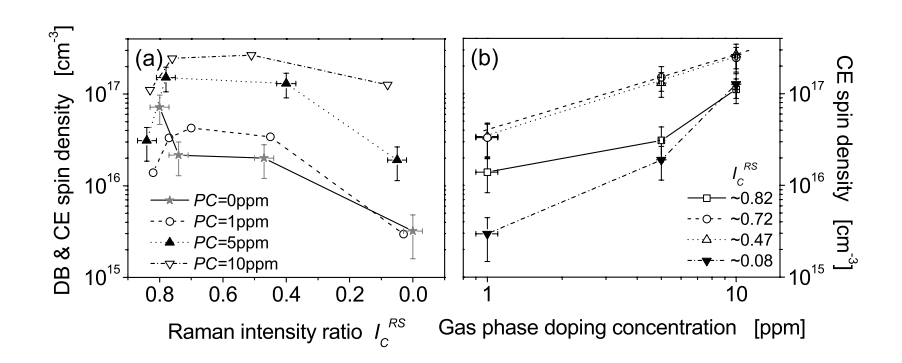


**Figure 5.5:** (a) Spin density of the CE resonance ( $N_{CE}$ ) in the doped samples and the DB resonance ( $N_{CE}$ ) in undoped material; (b) CE intensity of the microcrystalline phase as a function of conductivity.

of  $D^+$  states by an electron creating an  $D^0$  state exceeds the compensation of  $D^0$  states. This would be the case if in the undoped state the mean energy position of the defect is above  $E_F$ . Material prepared at yet higher doping concentration could give additional proof for this thesis.

The dangling bond signal can be detected in all spectra for all gas phase doping concentrations investigated. Within the highly crystalline regime,  $N_{DB}$  decreases between PC = 0 ppm and 1 ppm, but stays almost constant for higher doping concentrations.

#### 5.5 Conduction Band-Tail States

The deconvolution into the individual lines can also be used to determine the number of paramagnetic states in the conduction band-tail. The results for the calculated CE spin density  $N_{CE}$  for different doping levels are shown in Fig. 5.5 (a) as a function of  $I_C^{RS}$ . Additionally, the dangling bond densities  $N_{DB}$  for undoped material are plotted in the graph. The variation of  $N_{CE}$  as a function of  $I_C^{RS}$  and PC follows nicely the same qualitative behavior as the conductivity plotted in Fig. 5.2 (a). This confirms earlier studies on n-doped highly crystalline material [35, 39]. As expected, the intensity of the CE signal seems to be moderated by the dangling bond density. Material exhibiting the highest crystallinity  $I_C^{RS} = 0.82$  and also the highest  $N_{DB}$  shows lower CE line intensity compared to the  $I_C^{RS} = 0.72$  and  $I_C^{RS} = 0.47$  material, where lower  $N_{DB}$  are observed. For samples with a crystalline volume fraction lower than  $I_C^{RS} = 0.47$  the influence of  $N_{DB}$  on doping is masked by effects of the structural change. ESR as an integrating measurement

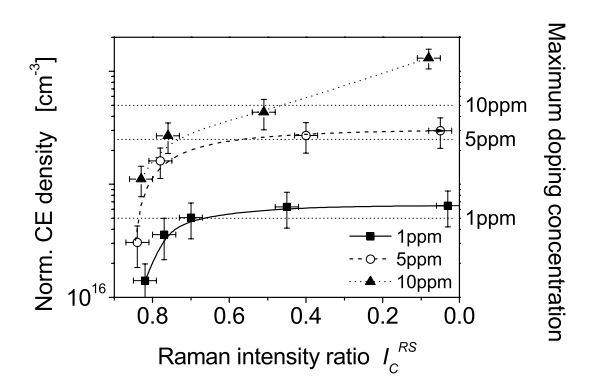


**Figure 5.6:** Normalized CE spin densities  $N_{CE(norm)}$  as a function of the Raman intensity ratio  $I_C^{RS}$ . Also indicated are the maximum doping concentrations evaluated from the gas phase doping concentrations PC using a built-in factor and a doping efficiency of one.

technique measures the number of spins in a particular amount of material. Because the CE resonance only originates from the crystalline phase, one would expect that the density decreases with increasing amorphous content. This can be seen for the low level doped samples, where the spin density  $N_{CE}$  decreases by about one order of magnitude with decreasing crystallinity from  $I_C^{RS} = 0.47$  to 0.08. Fig. 5.5 (b) shows  $N_{CE}$  against the gas phase doping concentration. For the crystalline low defect material ( $I_C^{RS} = 0.72 - 0.47$ )  $N_{CE}$  increases nearly linearly with a structure independent slope as a function of increasing gas phase doping concentration. On the other hand, the influence of the high dangling bond density  $N_{DB} = 7.2 \times 10^{16}$  cm<sup>-3</sup> (for  $I_C^{RS} = 0.82$  material) and the low crystalline volume fraction ( $I_C^{RS} = 0.08$ ) results in lower CE intensities. For higher doping concentrations these effects are less pronounced and result in higher CE spin densities.

To account for the fact that the CE signal originates only from the crystalline phase of the  $\mu$ c-Si:H material, the CE spin densities  $N_{CE}$  were normalized with respect to the crystalline volume content  $I_C^{RS}$ . The results are plotted in Fig. 5.6. Also indicated in Fig. 5.6 are the maximum dopant densities calculated with a built-in factor of one and a doping efficiency of unity, taken with respect to the atomic density of silicon of  $5\times10^{22}$  cm<sup>-3</sup>. For example, PC=1 ppm corresponds to a donor density of  $5\times10^{16}$  cm<sup>-3</sup>. Apparently, with this simple normalization procedure, the influence of the structural change on  $N_{CE}$  (Fig. 5.5 (a)) can completely be compensated. Independent of the structure composition,  $N_{CE(norm)}$  increases as a function of the doping concentration. On the other hand,  $N_{CE(norm)}$  increases with decreasing  $I_C^{RS}$ , saturating at the value of the maximum doping

concentration evaluated from the gas phase doping concentration *PC*. This is in agreement with the decreasing defect density observed in undoped material (compare Fig. 4.5 (a)), proving that the occupation of conduction band-tail states is governed by the compensation of gap states.

#### 5.6 Discussion

In section 4.4 the spin densities  $N_S$  of intrinsic microcrystalline material of various structure compositions were discussed. However, as ESR only detects single occupied states  $D^0$  it remains unclear to what extent the measured  $N_S$  is related to the real defect density of the material. In this Chapter, ESR in combination with conductivity measurements were applied on n-type  $\mu$ c-Si:H with different phosphorous doping concentrations PC and different structure compositions  $I_C^{RS}$  to study the density of gap states and the influence of these states on the free charge carrier density. PC was chosen to be close to the defect density, where the doping induced Fermi level  $(E_F)$  shift is determined by the compensation of gap states.

The results confirm that in  $\mu$ c-Si:H, like in a-Si:H, the doping induced Fermi level shift is governed by the compensation of gap states for doping concentrations up to the dangling bond density  $N_{DB}$ . Doping induced changes can be observed in both, the ESR signal and the electrical conductivity. While the electrical conductivity increases, in ESR the increasing intensity of the CE resonance indicates a shift of  $E_F$  as a function of PC. This confirms the close relation between the dark conductivity  $\sigma_D$  of  $\mu$ c-Si:H at 300K and the spin density of the CE resonance  $N_{CE}$ , that have led authors to assign the CE signal to localized states close to the conduction band [30, 29, 36, 72]. However, this is known for a long time. Far more interesting is the fact that both  $\sigma_D$  and  $N_{CE}$  are moderated in the same way by the defect density  $N_{DB}$ . Doping induced changes are highest for material where low spin densities are found in the undoped state. For highly crystalline material, that also exhibits the highest spin densities, the doping induced changes are considerably less. In other words, the higher DB density observed in highly crystalline material results in lower values of conductivity and lower  $N_{CE}$  as a function of the doping concentration. On the other hand, for samples with a low crystalline volume fraction of  $I_C^{RS} = 0.08$  the much lower DB density allows much higher  $\sigma_D$ and  $N_{CE}$ , the latter normalized to the crystalline volume fraction (Fig. 5.6).

It is surprising, that by doing this normalization the maximum  $N_{CE}$  obtained at  $I_C^{RS} = 0.08$  is in very good quantitative agreement with the values of the maximum dopant concentration calculated from the gas phase doping concentration, PC.

This suggests a built-in coefficient of phosphorous into the Si-matrix and active donor concentration of unity, if one excludes charge transfer from the amorphous phase. Keeping in mind the characteristic of the spin density  $N_{DB}$  of the undoped material, the results are in agreement with the proposed doping mechanism and confirm that the measured  $N_{DB}$  represents the defect density in the material. In a simple picture, defects in the gap of  $\mu$ c-Si:H, or more precisely, states in energy below the phosphorus donor states, have to be filled up first before the Fermi level can be shifted into conduction band-tail states, where the majority of the electrons is located which contribute to the CE resonance at 40 K. Tacitly also this assumes, that the phosphorus donor states are located in a position close to the conduction band like in crystalline silicon and that the majority of defects contributing to  $N_{DB}$ , no matter where they are located (inside the crystalline cluster columns; at the cluster boundaries; in the disordered regions) affect the  $E_F$  shift. It seems important to note, that the observed built-in ratio of P into the Si-matrix of unity somewhat differs from values observed in earlier investigations, where within some scatter a value of about 0.5 has been found [30, 32]. As these authors studied only highly crystalline material, the built-in ratio might vary upon different growth conditions.

From great importance is the energetic distribution of the paramagnetic states within the band gap of the  $\mu$ c-Si:H material. While the intensity of the CE resonance increases with increasing doping concentration, surprisingly the DB resonance is observable in all spectra. From the measurements presented in this chapter it is, however, not possible to distinguish between both DB centers (db<sub>1</sub> and db<sub>2</sub>) and therefore only their sum will be discussed here.

The rather strong overlap of more than 0.1 eV suggest that the CE and DB states are spatially separated from each other. This further supports the suggestions made in section 4.4, where the DB resonance, in particular the db<sub>2</sub>, was attributed to states located in hydrogen reach regions at the column boundaries. On the other hand, it is a widely accepted fact that the CE signal originates from the crystalline phase of  $\mu$ c-Si:H. Additional support for this thesis comes from Zhou et al., who used electron-spin-echo envelope modulation (ESEEM) to measure the interaction of the unpaired electron with its surrounding nuclear spins [165]. The finding was that the echo decay of the DB signal is modulated by the <sup>1</sup>H nuclei, while no modulation of the CE echo decay could be found. This suggests, that the DB centers are located in hydrogen rich regions, whereas the CE centers arise from hydrogen depleted parts of the  $\mu$ c-Si:H films. Although these results could not be confirmed yet, they still support the considerations made in this work.

Why does the spatial separation lead to an energetic overlap of the db<sub>2</sub> and the CE states? Keeping in mind that the column boundaries also represent the interface between the crystalline phase and the disordered material a schematic

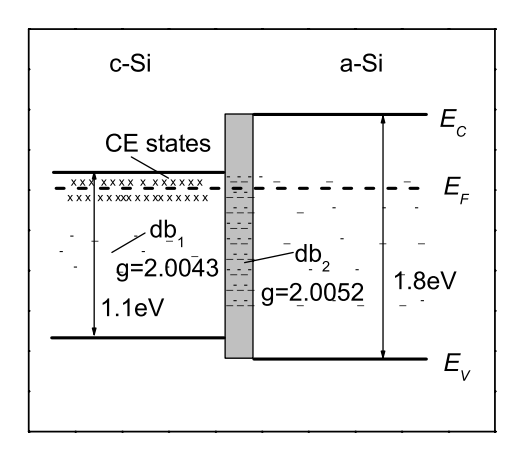


**Figure 5.7:** Schematic band diagram of the transition region between the crystalline and disordered phase in  $\mu$ c-Si:H.

band diagram as shown in Fig. 5.7 can be drawn. The results support an earlier suggestion that in  $\mu$ c-Si:H there should exist a considerable conduction band offset between the crystalline regions (for which the crystalline silicon band gap  $E_G=1.1$  eV is assumed) and the disordered regions (for which the a-Si:H gap  $E_G=1.8$  eV is assumed [65]). This would result in a significant overlap between the energy of DB and CE center as shown in Fig. 5.7. Otherwise the simultaneous occurrence of the CE and the DB signal for significant  $E_F$  shifts are difficult to explain if one does not allow for strong potential fluctuations in the material. Apparently, this earlier assumption concluded from dark and light induced ESR studies on highly crystalline material is valid even in material with very small crystalline volume fraction [30]. Even for material with  $I_C^{RS}=0.08$  containing only a minute amount of the crystalline phase, i.e., crystalline grains strongly diluted in the amorphous matrix, doping concentration as low as  $5\times10^{16}$  cm<sup>-3</sup> can shift the Fermi level into the conduction band-tail of the crystallites and activate a stable CE resonance.

# 5.7 Summary

The doping induced Fermi level shift in  $\mu$ c-Si:H, for a wide range of structural compositions, is governed by the compensation of defect states for doping concentrations up to the dangling bond spin density. For higher doping concentrations a doping efficiency close to unity is found. The close relationship between the CE resonance intensity and the conductivity is confirmed, which means the elec-

trons contributing to the CE signal represent the majority of the charge carriers contributing to electric transport. The fact, that for low defect material the  $N_{CE}$  approaches the value of the maximum doping concentration, proves the close relation between phosphorus concentration  $N_P$  and  $N_{CE}$ . However, while in earlier investigations a built-in factor of 0.5 and a doping efficiency of unity was found the results presented here suggest that both are of the order of unity, assuming that charge transfer from the amorphous phase can be excluded. Measuring the real phosphorous concentration using high resolution ion mass spectroscopy (SIMS)<sup>1</sup> could resolve this puzzle and will be a task for future experiments. A significant conduction band off-set between crystalline and disordered regions in  $\mu$ c-Si:H is suggested in agreement with earlier studies.

 $<sup>^{1}</sup>$ Note, that the sensitivity limit of a quadrupole mass spectrometer for the measurement of P-concentrations exceeds several  $10^{18}$  cm $^{-3}$ , due to the presence of silicon hydrides of nearly the same mass as the phosphorous ions. Using a high resolution mass spectrometer, the mass defect between  $^{31}$ P and the different silicon hydrides can be used to discriminate between the respective ions.

# Chapter 6

# Reversible and Irreversible Effects in $\mu$ c-Si:H

Even though highly crystalline  $\mu$ c-Si:H does not suffer from light induced degradation, known as Staebler-Wronski-Effect [7, 86], the particular structure properties, described in section 2.1, suggest that instabilities and metastable phenomena may also occur in this material. In particular,  $\mu$ c-Si:H grown at high hydrogen dilution, which yields the largest grain sizes and the highest crystalline volume fraction, shows a pronounced porosity. The existence of crack-like voids in this material facilitates the diffusion of atmospheric gases into the structure. Adsorption and/or chemical reactions, e.g. oxidation, at the column boundaries, might lead to the creation or termination of surface states and might significantly affect the electronic properties of the material.

In the following Chapter, we want to investigate and identify instability effects caused by adsorption and oxidation in  $\mu$ c-Si:H and want to relate them to changing structure compositions, ranging from highly crystalline porous, to highly crystalline compact and mixed phase amorphous/crystalline material.

## 6.1 Metastable Effects in $\mu$ c-Si:H

In this section, reversible phenomena in undoped  $\mu$ c-Si:H with various structure compositions are identified and their investigation by the use of electron spin resonance and electrical conductivity measurements is reported.

## **6.1.1** Influences of Sample Preparation

Material with different structure compositions deposited on both Al and Mo substrates was prepared using VHF-PECVD and studied extensively by ESR. The

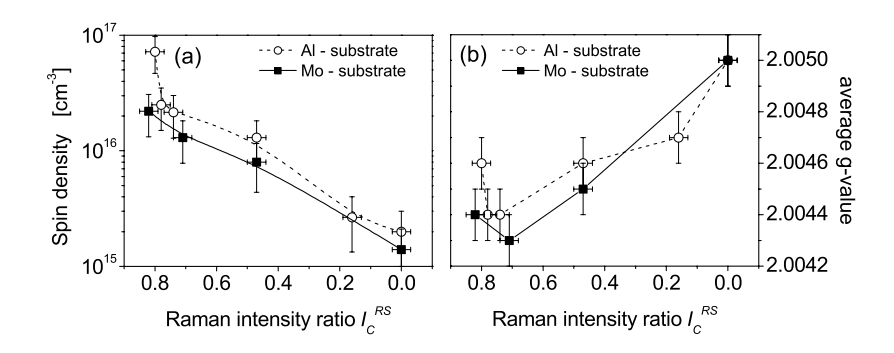


**Figure 6.1:** (a) Spin density  $N_S$  of  $\mu$ c-Si:H powder obtained from Al substrates  $(\bigstar)$  and Mo  $(\blacksquare)$ . In panel (b) the corresponding g-values are plotted.

use of these different substrates requires a different handling of the material as described in section 3.3.1. While material deposited on aluminum foil is in contact with acids, water, and air for a fairly long time, material prepared on molybdenum substrates can be peeled off and sealed into inert gas atmosphere immediately without any further treatment.

In Fig. 6.1 the spin densities  $N_S$  and average g-values of samples deposited on both aluminum and molybdenum substrates are shown. Material prepared on Al and Mo, shows the same characteristic upon decreasing  $I_C^{RS}$ . The highest  $N_S$ values are observed for the highly crystalline samples and  $N_S$  decreases monotonically with increasing amorphous phase content. However, there are some remarkable influences of the etching (HCl + H<sub>2</sub>O) and drying process on the spin density  $N_S$  and on the average g-value. Compared to samples deposited on Mo, for material prepared on Al substrates one observes a considerable increase of  $N_S$ (Fig. 6.1 (a)) accompanied by a shift of g to higher values (Fig. 6.1 (b)). Influences can be observed for all structure compositions from highly crystalline to amorphous. The changes in  $N_S$  and the g-value are highest for material with the highest crystallinity ( $I_C^{RS} = 0.81$ ), that also possesses the highest porosity (compare section 2.1). For highly crystalline porous material deposited on Al substrates, the spin density is a factor of three higher than compared to that deposited on Mo. The increasing  $N_S$ , from values of  $N_S = 2.2 \times 10^{16}$  cm<sup>-3</sup> (Mo substrates) to  $7.2 \times 10^{16}$  cm<sup>-3</sup> (Al substrates), is accompanied by a shift of the average g-value from g=2.0044 to 2.0046. For higher amorphous phase content the absolute changes in  $N_S$  are considerably less with  $\Delta N_S \approx 10^{16} \ {\rm cm}^{-3}$  for  $I_C^{RS}=0.71$  and they further decrease with increasing amorphous content.

To determine whether the HCl, the water, or the drying in air atmosphere causes the changes in  $N_S$ , powder obtained from samples deposited on Mo sub-

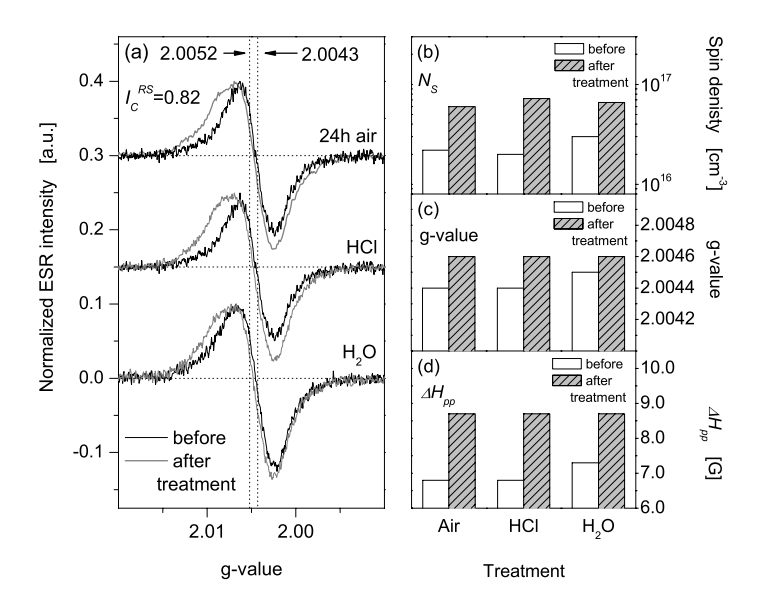


**Figure 6.2:** (a) ESR spectra of highly crystalline material ( $I_C^{RS} = 0.82$ ) before and after treatment in HCl, H<sub>2</sub>O, and storage in air atmosphere. Panel (b) shows the measured values of the spin densities, (c) the g-value, and (d) the peak to peak line width  $\Delta H_{pp}$  before and after treatment, respectively.

strates was rinsed in either H2O or HCl/H2O solution, or was just kept in air atmosphere for 24 hours. In each case ESR spectra were recorded before and after the treatment. The results are shown in Fig. 6.2 (a). The spectra were normalized to the same peak height allowing differences in the line shape to be compared. The vertical dotted lines indicate the resonances with g-values at g=2.0043 and g=2.0052, typically observed in  $\mu$ c-Si:H (see section 2.2.2). Independent of the particular treatment the line shape changes significantly. The intensity of the ESR signal increases for higher g, which is equivalent with the low magnetic field site. The increase of the signal intensity at higher g-values is accompanied by a shift of the zero crossing of the ESR line towards higher values, observable in all spectra. Besides these effects, which are similar for all sample treatments discussed here, slight differences occur for the case of the H<sub>2</sub>O treatment. Here the spectra taken before the treatment already show a higher intensity of the signal at high gvalues. However, the characteristic changes upon the treatment and the observed shift of the average g-value are a general trend for all treatments. This indicates that the pre-treatment differences in the "H<sub>2</sub>O"-spectra are a result of the fact that instability effects already affected the material before the first measurement has been performed. This is in agreement with the observed values of the spin density  $N_S$ , the electronic g-value, and the line width  $\Delta H_{pp}$  plotted in Fig. 6.2 (b, c, d). Independently of the particular treatment one observes an increase of all these three quantities. For all treatments (i) the spin density increases by up to a factor of three, saturating at values of  $N_S \approx 6 \times 10^{16}$  cm<sup>-3</sup>, (ii) the electronic g-value shifts to higher values starting from g=2.0044 (2.0045 for H<sub>2</sub>O) and final values of g=2.0046, and (iii) the line width increases from  $\Delta H_{pp} = 6.8 \pm 0.1$  G (7.3 ± 0.1 G for H<sub>2</sub>O) to 8.7 ± 0.1 G. Quite surprisingly, the final values of  $N_S$ , g, and  $\Delta H_{pp}$  are the same for all treatments.

This result clearly indicates that it is not the HCl etching step, which causes the additional increase in  $N_S$ , the shift of the electronic g-value, and the increased  $\Delta H_{pp}$ . In fact, the observed changes are essentially the same if the powder is just treated in water and even a simple storage of the material in air leads to a similar effect. The fact that the pre-treatment values of the "H<sub>2</sub>O"-material are slightly higher, compared to the material treated in HCl and air supports the assumption that in this case instability effects already set in before the first measurement could be performed.

The study of different treatments, described above, was performed on material with a pronounced crystallinity. The effects of an increasing amorphous phase is now discussed. For a better understanding of the results shown below, it is important to note, that with increasing amorphous content of the films the film structure may change as well as the film composition. While  $I_C^{RS} = 0.82$  material shows a high degree of porosity,  $I_C^{RS} = 0.71$  material is still highly crystalline, but compact. Finally  $I_C^{RS} = 0.47$  material is prepared at the transition between microcrystalline and amorphous growth and shows a rather compact structure with a high a-Si:H contribution (see section 2.1).

Fig. 6.3 (a) shows the ESR spectra of material with three different structure compositions ranging from highly crystalline porous ( $I_C^{RS} = 0.82$ ) over highly crystalline compact material ( $I_C^{RS} = 0.71$ ) to material at the threshold between crystalline and amorphous growth ( $I_C^{RS} = 0.47$ ). The spectra were taken before and after a H<sub>2</sub>O treatment and then normalized in order to show differences in the line shape. Also indicated as vertical dotted lines are the resonances with g-values at g=2.0043 and g=2.0052. Changes in the shape of the ESR spectra can be observed for the  $I_C^{RS} = 0.82$  and  $I_C^{RS} = 0.71$  material, while on the other hand the line shape of the  $I_C^{RS} = 0.47$  spectra remains unchanged upon the H<sub>2</sub>O treatment. As for the  $I_C^{RS} = 0.82$  material, which was discussed above (see Fig. 6.2), in the  $I_C^{RS} = 0.71$  samples the intensity at the high g-value site of the spectra has a larger contribution to the total ESR intensity after the treatment. In Fig. 6.3 (b, c, d)

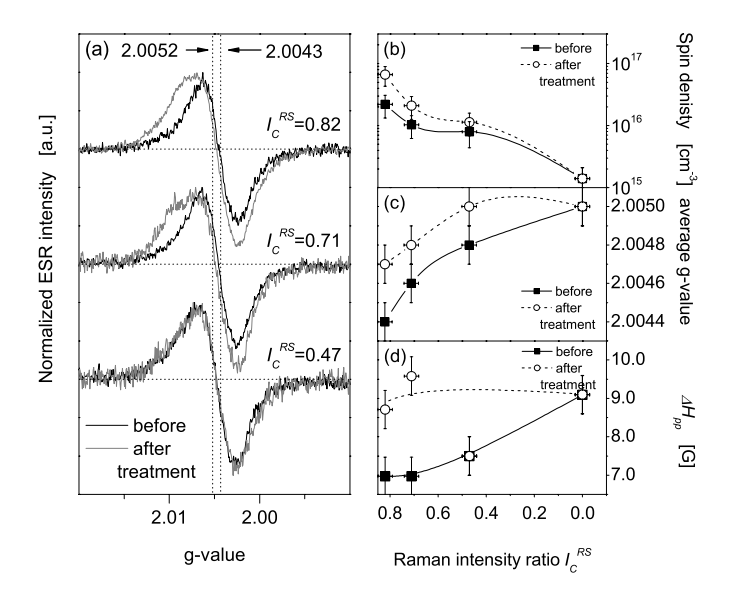


**Figure 6.3:** (a) ESR spectra of material with three different structure compositions ranging from highly crystalline porous over highly crystalline compact material to material at the threshold between crystalline and amorphous growth, before and after a  $H_2O$  treatment (see section 3.3.1 for details). Panel (b) shows the measured values of the spin densities, (c) the g-value, and (d) the peak to peak line width  $\Delta H_{pp}$  versus  $I_C^{RS}$ , before and after treatment.

the absolute values of  $N_S$ , the g-value, and  $\Delta H_{pp}$  versus  $I_C^{RS}$  before and after the treatment are shown. As can be seen from the figure, the magnitude of instability effects decreases with increasing amorphous phase content. While for the highest crystallinity ( $I_C^{RS} = 0.82$ )  $N_S$  increases by about a factor of three, the changes for the  $I_C^{RS} = 0.71$  material are considerably less and almost disappear for the material prepared at the transition between microcrystalline and amorphous growth. The same effect can be observed for the values of g and  $\Delta H_{pp}$ . Both quantities increase upon treatment, the absolute changes however are less pronounced for the transition material.

Because the ESR spectra of  $\mu$ c-Si:H can be described by two contributions at g=2.0043 (db<sub>1</sub>) and g=2.0052 (db<sub>2</sub>), it is interesting to see in which way and to what degree the respective spin states are involved in the increase of  $N_S$ ,  $\Delta H_{pp}$ , and the average g-value. The ESR spectra of Fig. 6.3 (a) therefore have been deconvoluted into these two contributions. The fits were performed using Gaussian lines with a line width of  $\Delta H_{pp} = 5.6$  G and  $\Delta H_{pp} = 9.7$  G for the db<sub>1</sub> and db<sub>2</sub>

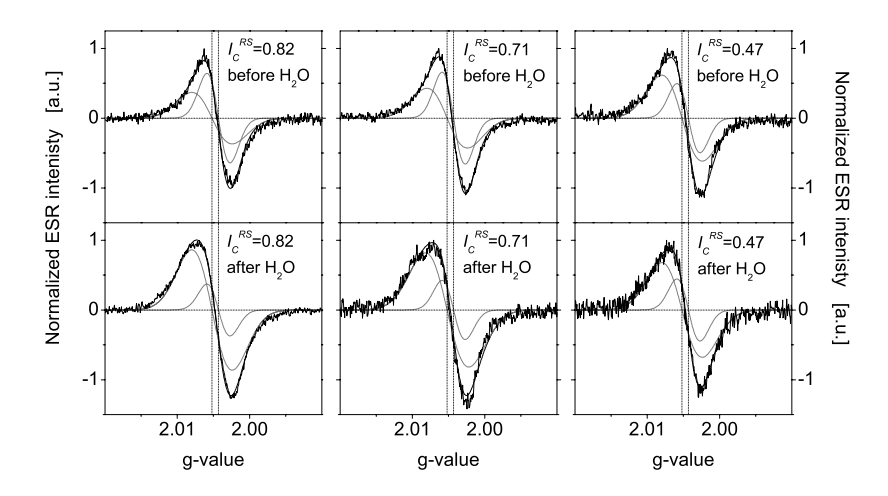


**Figure 6.4:** De-convolution of the ESR spectra already shown in Fig. 6.3 (a) into the two signals at g=2.0043 and 2.0052 before (upper traces) and after the treatment (lower traces).

resonance, respectively. For fitting, the line width and the peak position were kept fixed, and only the amplitude of the Gaussian was varied. The results are plotted in Fig. 6.4. In the figure the measured data, the fit curve as well as the individual resonances are shown. The vertical dotted lines indicate the g-values at g=2.0043 and g=2.0052. All spectra show the asymmetric  $\mu$ c-Si:H line shape and can be well approximated by the two resonance lines at g=2.0043 and g=2.0052. Unsurprisingly, for the transition material the relative contribution of both resonances changes only slightly. Before and after the treatment the spectra are dominated by the db<sub>2</sub> signal, which increases slightly after the treatment. Looking at the  $I_C^{RS} = 0.82$  material the picture changes considerably. While in the original state the spectrum is dominated by the db<sub>1</sub> signal, the post-treated spectrum is clearly determined by spin centers contributing to the db<sub>2</sub> signal. The same effect, but less pronounced, can be observed for the highly crystalline but compact material. To determine the absolute changes  $N_S$  was evaluated for each resonance (db<sub>1</sub> and db<sub>2</sub>) by integrating the individual fit and comparing the contributions to the total intensity of the spectra. The values of  $N_S$  determined by this procedure are shown in Fig. 6.5. The plot shows the spin density of the individual lines before and after the treatment in H<sub>2</sub>O for each crystallinity investigated. Quite surprisingly, the treatment only effects paramagnetic states resulting in the db2 resonance, while the line at g=2.0043 remains unaffected. For the  $I_C^{RS} = 0.82$  material  $N_S$  of the

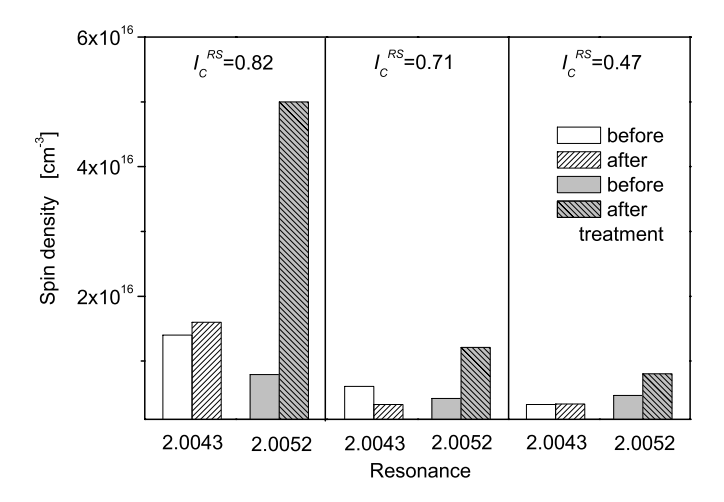


**Figure 6.5:** Spin density of the resonances at g=2.0043 and g=2.0052 before and after treatment in  $H_2O$ .

db<sub>2</sub> line increases by more than a factor of 6 from values of  $N_S = 8 \times 10^{15}$  cm<sup>-3</sup> to  $N_S = 5 \times 10^{16}$  cm<sup>-3</sup> while the db<sub>1</sub> resonance remains constant at values of about  $N_S = 1.5 \times 10^{16}$  cm<sup>-3</sup>. As expected from the overall spin density plotted in Fig. 6.3 (b) the absolute changes decrease with increasing amorphous content, the characteristic, however, remains the same. The line analysis shows that the increasing spin density can be attributed to an increase of the db<sub>2</sub> resonance while the  $db_1$  resonance at g=2.0043 stays constant.

In this section, it has been reported that the spin density of  $\mu$ c-Si:H increases as a result of contact with atmospheric gases or by a treatment in H<sub>2</sub>O. In particular, the number of spin states contributing to the db<sub>2</sub> resonance increases, while the spins of db<sub>1</sub> remain unaffected. The magnitude of the instability changes thus depends strongly on the particular structure. With increasing amorphous content and more compact structure the changes are reduced or may even disappear. However, so far the reason for these changes and the particular processes involved are unclear. It is interesting to consider if, and how, the material can be returned back to its initial state. The clear dependency of the magnitude of the changes in  $N_S$  on the structure, in particular the porosity, suggests that surface processes are involved. Assuming that the changes in the ESR signal intensity are a result of adsorption of atmospheric gases or water, annealing in inert gas atmosphere or vacuum might restore the initial material properties. This is the subject of the

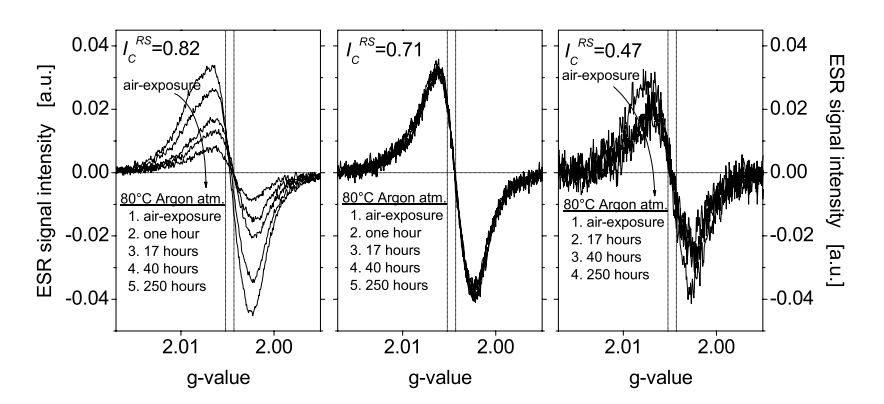


**Figure 6.6:** ESR signals of highly crystalline porous ( $I_C^{RS} = 0.82$ ), highly crystalline compact ( $I_C^{RS} = 0.71$ ), and from material at the transition from crystalline to amorphous growth ( $I_C^{RS} = 0.47$  for different annealing periods.)

following section.

#### 6.1.2 Reversible Effects in the ESR Signal

Material as studied above, i.e. with structure compositions including highly crystalline porous, highly crystalline compact, and transition material with a considerable amount of a-Si:H phase, has been stored in air for a prolonged period and afterwards sealed into argon atmosphere. The samples were then annealed at a temperature of 80°C for several hours. At regular intervals the annealing process was interrupted in order to measure ESR. The resulting spectra are plotted in Fig. 6.6. Unlike the ESR measurements shown before, these spectra are not normalized to the same peak height, but relative to the initial curve, denoted as (1.). Again the vertical lines indicate the position of the g-values at g=2.0043 and g=2.0052.

The most outstanding result in Fig. 6.6 is that quite moderate annealing temperatures of  $T=80^{\circ}\mathrm{C}$  strongly influence the ESR signal. As expected from the instabilities observed above, the magnitude of the effects is closely connected to the structure of the material. Significant changes can be observed for the highly crystalline porous material ( $I_C^{RS}=0.82$ ). The ESR signal decreases strongly after one hour annealing in argon atmosphere. With increasing annealing period  $t_{ann}$  the signal intensity decreases further. On the other hand, the ESR signal of the highly crystalline compact material ( $I_C^{RS}=0.71$ ) changes only slightly. This is quite surprising as instability effects could also be observed for these types of

sample<sup>1</sup> (see Fig. 6.3). Looking at the initial spectra of this sample, one can not see the typical shoulder at the high g-value site, expected for material exposed to air or water. The reason for the quite constant resonance upon annealing might therefore be a result of a higher stability of the material upon treatment in air or water. The transition material ( $I_C^{RS} = 0.47$ ) shows the same behavior like the  $I_C^{RS} = 0.82$  material. The ESR signal intensity decreases after annealing in argon atmosphere at  $T = 80^{\circ}$ C. As expected from the instability results described in section 6.1.1 the effect is less pronounced, compared to the highly crystalline porous material.

As already mentioned above, the decreasing ESR signal intensity directly scales with  $N_S$ . In fact, from Fig. 6.6 it is clear that the spin density decreases for the  $I_C^{RS} = 0.82$  and 0.47 material, as a function of annealing period  $t_{ann}$ . While the increase of the spin density exposure to air or water has been attributed to an increase of the number of spins with a g-value of g=2.0052, the annealing also just affects the db<sub>2</sub> resonance. This is shown in Fig. 6.7 (a, b), where the spin densities of the individual resonances  $db_1$  and  $db_2$  are plotted versus  $t_{ann}$ . Except for the  $I_C^{RS} = 0.71$  material,  $N_{db_2}$  decreases, while  $N_{db_1}$  remains constant. The decrease of the spin density at g=2.0052 is accompanied by a shift of the average g-value and a decrease of the line width  $\Delta H_{pp}$ . Both quantities are plotted in Fig. 6.7 (c) and (d), respectively. For the  $I_C^{RS} = 0.82$  material, annealing for 250 hours the spin density decreases from  $4 \times 10^{16}$  cm<sup>-3</sup> to  $9 \times 10^{15}$  cm<sup>-3</sup>, while the average g-value shifts from 2.0047 to 2.0044 and line width decreases from  $\Delta H_{pp} = 8.8$  G to 7.6 G. The final values after 250 hours annealing in argon atmosphere at 80°C are close to the initial values of the material before the exposure to air, as can be seen from Fig. 6.3 and 6.5. In fact, the increase of the spin density  $N_{db_2}$ , the shift of the g-value, and the increase of the line width  $\Delta H_{pp}$  can be reversed by a simple annealing step in argon atmosphere at temperatures of  $T = 80^{\circ}$ C. Interestingly, the reversible behavior in the ESR signal, particular the strong changes found in  $I_C^{RS} = 0.82$  material upon air-exposure and annealing can be repeated many times without any sign of fatigue.

However, while the spin density decreases upon annealing the question arises at what point the decrease will saturate. After 250 hours  $N_S$  shows an asymptotic behavior, but still does not saturate. Assuming the involved processes are thermally activated an increase of the temperature might accelerate the procedure. Annealing/air-exposure cycles have therefore been performed at a temperature of T = 160°C. The temperature was carefully chosen to considerably activate the process without leading to a desorption of hydrogen, which in term would lead to the creation of additional dangling bond defects. Fig. 6.8 shows the results

 $<sup>^{1}</sup>$ Note, that the samples used for annealing are not the same as the once used for the treatments in  $H_{2}O$ . However, the particular deposition parameters have been kept constant.

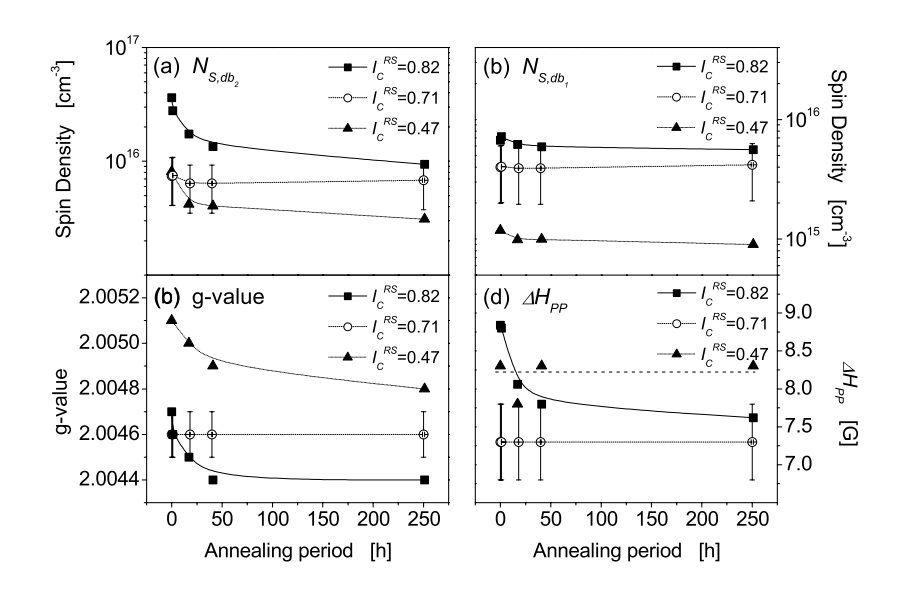


**Figure 6.7:** The absolute values of  $N_S$  for the individual lines at (a) g=2.0052 and (b) g=2.0043 were determined by deconvoluting the spectra shown in Fig. 6.6. In panel (c) and (d) the extracted values of g and  $\Delta H_{pp}$  are plotted versus the annealing period.

obtained from annealing the highly crystalline porous material ( $I_C^{RS} = 0.82$ ) in argon atmosphere. For the experiment the sample was stored in air for about 50 hours (upper trace in Fig. 6.8). After annealing the material at  $T = 160^{\circ}$ C for one hour, the ESR spectrum as shown as the middle trace in Fig. 6.8 was recorded. Quite surprisingly, the spectrum shows a strong contribution of the conduction electron resonance, after annealing (compare section 2.2.2). This suggests a considerable shift of the Fermi level up into the conduction band-tail. To determine  $N_S$  of the individual lines, the spectra were deconvoluted as indicated by the gray lines, shown in Fig. 6.8. The spin densities of the two resonances at g=2.0043 and g=2.0052 decrease as a result of the annealing. The particular values are plotted in table 6.1. The high number of electrons trapped in conduction band-tail states ( $N_{CE} = 6 \times 10^{16} \, \mathrm{cm}^{-3}$ ) suggests a considerable background doping in this sample. Quite surprisingly, these changes are reversible and the material can be treated back to its initial state by simply exposing it to air atmosphere, as shown in the lower trace of Fig. 6.8.

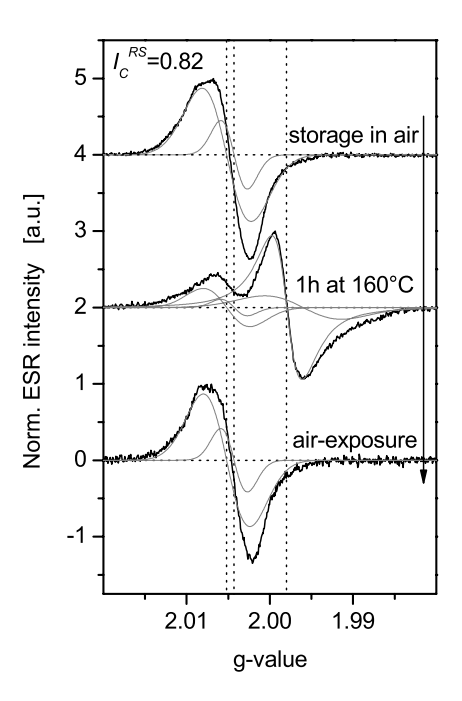


**Figure 6.8:** ESR signal of highly crystalline porous  $\mu$ c-Si:H after storage in air (upper trace), after annealing at  $T=160^{\circ}C$  for one hour (middle trace), and after an additional air-exposure. The vertical dotted lines indicate the g-values of g=2.0043 and g=2.0052 and g=1.998.

#### 6.1.3 Reversible Effects in the Electrical Conductivity

The changes in the ESR signal described above suggest that reversible effects might also affect the electrical transport. In particular, the emergence of a strong CE signal after annealing the highly crystalline porous material at elevated temperatures (see Fig. 6.8) suggests considerable shifts of the Fermi level, which might also be visible in the electrical conductivity. Fig. 6.9 shows a temperature cycle taken after the material was stored in air atmosphere for about one week. The samples were measured in a temperature range between  $T=100\mathrm{K}$  and  $450\mathrm{K}$  (•). The material was than kept in vacuum and annealed for 6 hours at T=450K. Afterwards the dark conductivity  $\sigma_D(T)$  has been measured again ( $\Delta$ ) in the temperature range between  $T=450\mathrm{K}$  and  $100\mathrm{K}$ . Reversible effects as a result of air-exposure and annealing cycles, as observed in ESR, can also be seen in  $\sigma_D$ . The dark conductivity of  $I_C^{RS}=0.82$  material, shown in Fig. 6.9 (a), shows

**Table 6.1:** Spin densities of the individual resonances of the  $I_C^{RS} = 0.82$  material after air-exposure and followed by annealing for one hour at 160°C in argon.

Resonance	$N_S$ (storage in air)	$N_S$ (after annealing)	$N_S$ (air exposure)
g=2.0043	$1 \times 10^{16} \text{ cm}^{-3}$	$2 \times 10^{15} \text{ cm}^{-3}$	$1 \times 10^{16} \text{ cm}^{-3}$
g=2.0052	$5 \times 10^{16} \text{ cm}^{-3}$	$1 \times 10^{16} \text{ cm}^{-3}$	$5 \times 10^{16} \text{ cm}^{-3}$
g=1.998-1.996	_	$6 \times 10^{16} \text{ cm}^{-3}$	_

considerably lower values after contact with air, over the entire temperature range investigated. After exposing to air the room temperature conductivity decreases by more than one order of magnitude. The conductivity can be restored to its initial values by annealing the material, just like for the changes observed in ESR. However, there is a distinct difference of the electrical dark conductivity  $\sigma_D$  between the porous and compact highly crystalline material upon storage in air and annealing steps. As for the highly crystalline porous sample ( $I_C^{RS}=0.82$ ) the room temperature dark conductivity decreases after storage in air, one can observe the opposite for the compact material, as shown in Fig. 6.9 (b). For the  $I_C^{RS}=0.71$  material the dark conductivity increases upon contact with air. Material prepared at the transition between microcrystalline and amorphous growth does not show any changes upon contact with air or annealing. Again the air-exposure/annealing cycles can be repeated many times without any sign of fatigue. The observed

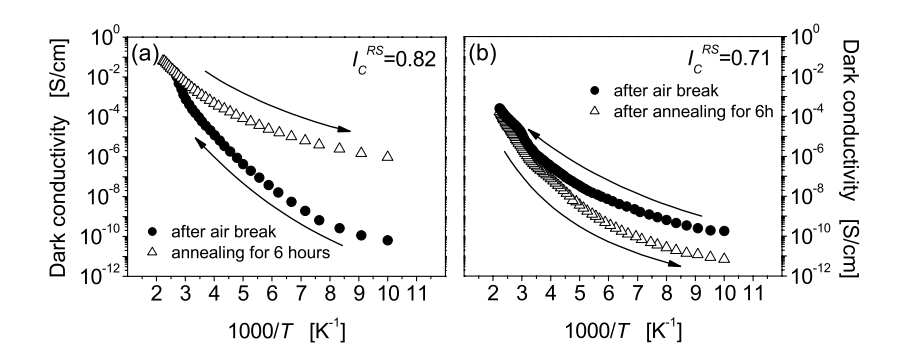


**Figure 6.9:** Dependence of the temperature dependent dark conductivity  $\sigma_D(T)$  on annealing/air-exposure cycles of (a) highly crystalline porous and (b) highly crystalline but compact material.

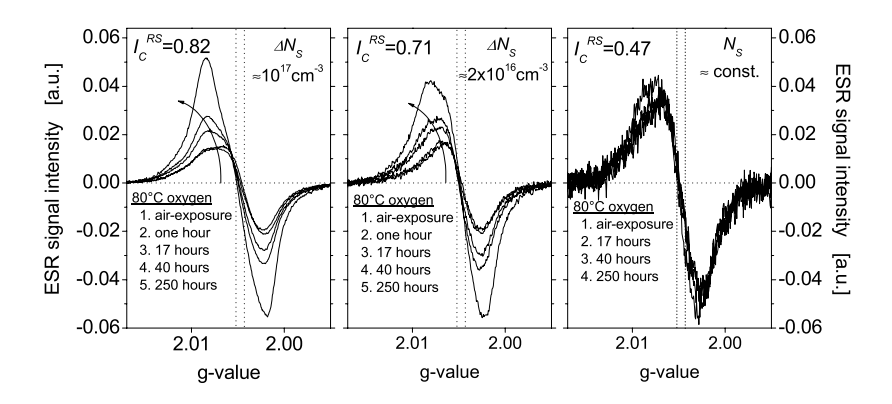


**Figure 6.10:** ESR signals of highly crystalline and porous ( $I_C^{RS} = 0.81$ ), highly crystalline compact ( $I_C^{RS} = 0.72$ ), and of material at the transition from crystalline to amorphous growth ( $I_C^{RS} = 0.47$ )

reversible effects in  $\sigma_D$  show many similarities to earlier investigations made on material which was grown using the chemical transport technique [20] or hot wire chemical vapor deposition [166].

#### **6.2** Irreversible Oxidation Effects

As shown above, storing highly crystalline  $\mu$ c-Si:H in air atmosphere results in a reversible increase of the spin density accompanied by a shift of the average g-value. However, it has been shown by e.g. infrared spectroscopy, that highly crystalline  $\mu$ c-Si:H is also susceptible to oxidation effects [11, 20, 51, 13], forming Si-O bonds at the grain boundaries, which are stable up to temperatures of T = 1050 K [20]. In the following section, effects of the oxidation of the grainor column boundaries on the ESR signal will be studied. Therefore, samples with different structure compositions, in fact material prepared in the same run as the one used for the air-exposure/annealing cycles (section 6.1), have been sealed into oxygen atmosphere and annealed at temperatures of  $T = 80^{\circ}C$ . After selected time intervals the annealing process was interrupted and ESR spectra were recorded. The spectra measured for the three structure compositions are shown in Fig. 6.10. As for the reversible changes discussed above, the magnitude of the observed changes strongly depends on the structure composition of the  $\mu$ c-Si:H. However, in contrast to the treatment in argon, annealing in oxygen atmosphere at a temperature of  $T = 80^{\circ}$ C leads to an increase of the ESR signal intensity. The observed line shape of the resonance differs significantly from that

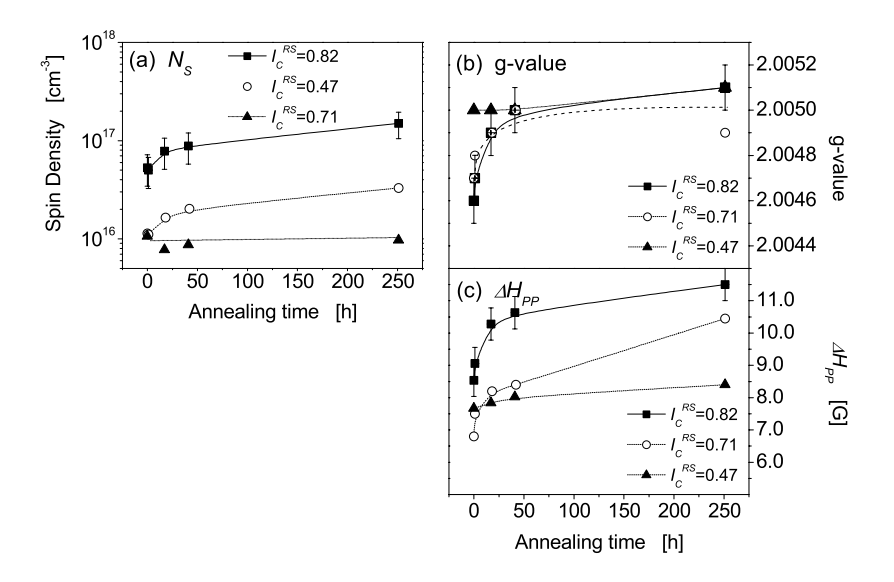


**Figure 6.11:** Absolute values of (a) the spin density, (b) the g-value, and (c) the peak to peak line width as a function of the annealing period.

observed in  $\mu$ c-Si:H. In fact, it is impossible to fit the measured data with any combination of the two resonances at g-values of g=2.0043 and g=2.0052. Fitting with three resonance lines might appear promising, but cannot be justified without more experimental evidence. On the other hand, a fit with three signals (either Gaussian or Lorentzian) using as many as 9 free parameters (peak position, width, amplitude for each signal) is most questionable. The absolute values of  $N_S$ , g, and  $\Delta H_{pp}$  shown in Fig. 6.11 are therefore extracted from the overall signal without deconvoluting the spectra. The spin density, plotted in panel (a), increases with increasing annealing period. The changes are highest for the highly crystalline porous material ( $I_C^{RS} = 0.82$ ), where the overall  $N_S$  increases from values of  $N_S(t=0) = 5 \times 10^{16}$  cm<sup>-3</sup> to  $N_S(t=250h) = 1.5 \times 10^{17}$  cm<sup>-3</sup>. With increasing amorphous content the porosity of the material and therefore the active surface area decreases. The increase of  $N_S$  within 250h is less pronounced, with  $\Delta N_S \approx 2 \times 10^{16} \text{ cm}^{-3} \text{ for } I_C^{RS} = 0.71 \text{ material, or even disappears for } I_C^{RS} = 0.47.$  The increase in the spin density is accompanied by a shift of the average g-value, which is shown in Fig. 6.11 (b). Again the changes are highest for the porous sample where the g-value increases from g=2.0046 to g=2.0051; the shift becomes less pronounced upon increasing amorphous content. As can be seen in Fig. 6.10, while the oxidation process proceeds, the peak to peak line width of the overall signal increases. The absolute values, plotted in Fig. 6.11 (c), confirm that the magnitude of the changes strongly depends on the structure of the material. While for the porous material the line width increases from values of  $\Delta H_{pp} = 8.5$  G to 11.5 G,  $\Delta H_{pp}$  of the transition material increases only slightly.

In contrast to the air-exposure/annealing cycles described in section 6.1, annealing of oxidized samples in argon at temperatures below  $T=200^{\circ}\mathrm{C}$  does not have any effect on the ESR signal. For higher temperatures than  $T=200^{\circ}\mathrm{C}$  bonded hydrogen, used to terminate vacant Si bonds, will desorb, resulting in a further increase of the dangling bond density. However, assuming that the increasing spin density, observed in Fig. 6.11, is a result of the oxidation, a dip into hydrofluoric acid (HF), well known from silicon wafer cleaning technology, provides a simple way to remove the oxide from the surface and by the way passivating dangling bonds by establishing Si-H bonds.

#### **6.2.1** Reversibility by Chemical Reduction

In order to remove the oxygen surface layer a 5% HF solution was used. The sample was etched in the acid for 30 seconds, carefully rinsed in distilled water, and dried by flushing with nitrogen. To avoid as much re-oxidation and post-contamination as possible the sample was immediately sealed in argon atmosphere and measured within 5 min after the cleaning process. For the ease of sample handling material has been prepared on glass substrates. The price to pay is a considerably lower signal to noise ratio due to the reduced sample volume. Additionally, the ESR spectra of the  $\mu$ c-Si:H is superimposed by signal traces from the borosilicate glass at g=2.001. However, still one can easily observe the effects as shown in Fig. 6.12 (a). The figure shows three spectra of highly crystalline porous material (i) taken right immediately after the deposition, (ii) after an annealing step in  $O_2$  atmosphere for two hours at  $T = 160^{\circ}$ C, and (iii) after the treatment in HF acid. The spectra shown are not normalized, so differences in the signal intensity are a result of a change in the spin density. After annealing in O<sub>2</sub> atmosphere for two hours the spectrum shows a higher intensity compared to the "as deposited" signal, indicating an increase of  $N_S$ . In fact, the spin density increases from values of  $N_S = 5 \times 10^{16} \text{ cm}^{-3}$  to  $N_S = 2 \times 10^{17} \text{ cm}^{-3}$ , resulting in the same line shape as observed for the O2-annealed material in Fig. 6.10. After the HF-dip the intensity decreases again and the line shape returns back to its initial form. Looking at the absolute values of  $N_S$ , the g-value, and  $\Delta H_{pp}$ , plotted in Fig. 6.12 (b, c, d) the success of the HF-dip becomes more obvious. While all three quantities increase after annealing in oxygen, which in fact is the same effect as observed for the powder samples, all three quantities restore back to their initial values, after the treatment in HF acid.

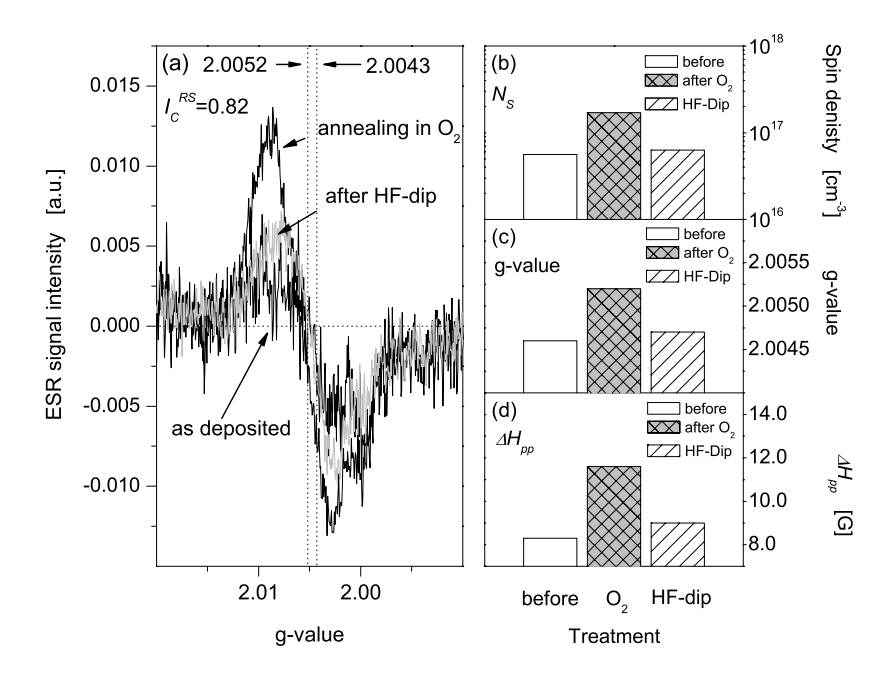


**Figure 6.12:** (a) ESR spectra of a porous  $\mu$ c-Si:H sample ( $I_C^{RS} = 0.82$ ) deposited on glass substrate measured right after deposition, annealing in  $O_2$ , and after etching in HF. In panel (b) the measured values of  $N_S$ , (c) the g-value, and (d)  $\Delta H_{pp}$  before and after the HF-dip are shown.

### 6.2.2 Charge Transfer caused by Oxidation of N-Type $\mu$ c-Si:H

As shown above, annealing  $\mu$ c-Si:H in oxygen atmosphere leads to an increase of the spin density. The fact that the corresponding resonance appears at higher g-values and exhibits a different line shape than observed for the resonances at g=2.0043 and g=2.0052 suggests that the additional spin states are somehow different. In Chapter 5 the use of phosphorous doping to probe the density of gap states was described and it was found that the shift of the Fermi level is governed by the compensation of gap states. In fact, states within the band gap have to be filled before states in the conduction band-tail can be occupied.

The aim of this section is to use the n-type doping experiment just in the opposite direction. The question is, if and how the spin states created by the oxidation of the surface affect the position of the Fermi level and lead to a depopulation of conduction band-tail states. Annealing experiments have therefore

been performed on  $I_C^{RS} = 0.82$  material with phosphorous doping concentrations of 10<sup>17</sup> cm<sup>-3</sup>. The highly crystalline porous material was chosen because it showed the biggest changes upon oxidation (see Fig. 6.10). The measured spectra taken after different stages of the oxidation process are shown in Fig. 6.13 (a). In the initial state the ESR signal is dominated by the CE resonance, which arises from electrons trapped in conduction band-tail states. As expected from the experiments on intrinsic material the intensity of the ESR signal around g=2.005 increases as a function of the annealing period. With the creation of additional states, the CE centers become depopulated resulting in a decrease of the signal intensity around g=1.998. This will happen when the states created by the oxidation are located lower in energy than the CE states. Providing that these states can accommodate additional electrons they will become occupied, while states in the conduction band become depopulated. The assumption that the electrons are transferred from CE states to states created by oxidation of the surface is supported by absolute values of the spin density plotted in Fig. 6.13 (b). The spin density was determined by integrating the ESR spectra over the entire range measured. It is surprising, that

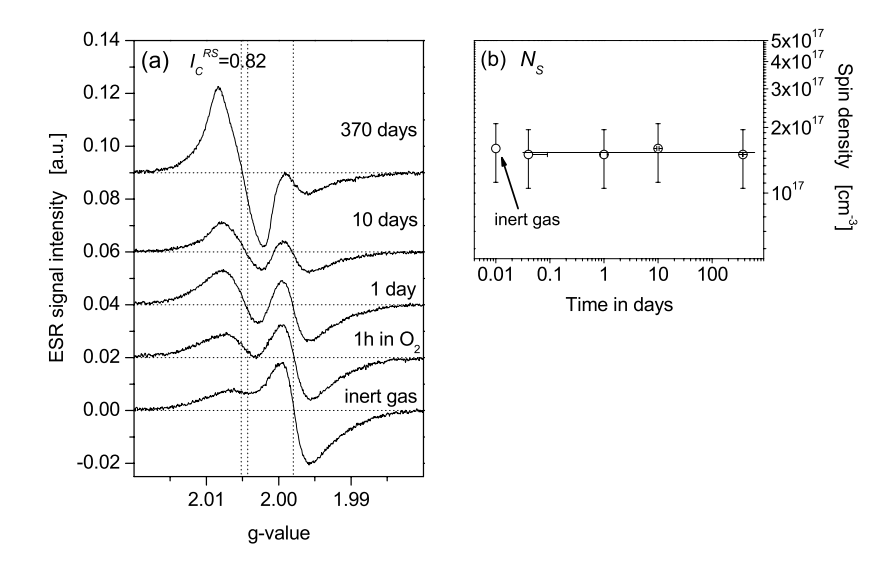


**Figure 6.13:** ESR signal of a n-type highly crystalline porous  $\mu$ c-Si:H sample with 10 ppm PH<sub>3</sub> doping for different periods of storage in oxygen atmosphere. The measurements were taken at T = 40K. In (b) the number of spins ( $N_S$ ), contributing to the spectra shown in panel (a) is shown; the spectrum taken in inert gas is arbitrarily set at 0.01 days.

upon annealing the total number of spins observed in ESR does not vary, while the g-value changes considerably. As the value of g is strongly connected to the microscopic environment surrounding the paramagnetic state, this indicates that only the microscopic location of the resonant electrons changes and defect states created by oxidation are not involved in compensation effects. The reason for this remains unclear and requires further investigation.

## 6.3 On the Origin of Instability Effects in $\mu$ c-Si:H

In- and out-diffusion of impurities and atmospheric gases leads to numerous instability and metastable phenomena on the ESR signal and the electrical conductivity in  $\mu$ c-Si:H at or close to room temperature. It appears, that the amplitude of these changes is connected to the surface area of the material. Reversible and irreversible changes in  $N_S$  are highly pronounced for  $I_C^{RS} = 0.81$  material which exhibit a very porous structure (compare section 2.1). In highly crystalline material with only a minute amount of amorphous phase content, which has shown to be compact, the effects are much less prominent and are almost absent for still lower  $I_C^{RS}$ . In the following section the observed meta-stable and irreversible effects in  $\mu$ c-Si:H of various structure compositions will be discussed. The main effects to consider are adsorption and oxidation on surfaces, caused by atmospheric gases.

#### 6.3.1 Adsorption of Atmospheric Gases

The results presented in section 6.1 show that the spin density  $N_S$ , the average g-value, as well as the electrical conductivity  $\sigma_D$  strongly depend on the particular treatment and the history of  $\mu$ c-Si:H material. While  $N_S$  increases upon storing in air atmosphere, the effect can be reversed by a simple annealing step in argon atmosphere. A detailed analysis of the ESR spectra shows that the changes in  $N_S$  can be traced back to a varying number of spins with a g-value of g=2.0052, while the db<sub>1</sub> resonance at g=2.0043 remains unaffected. On the other hand, for  $\sigma_D$  not only the amplitude, but also the direction of the changes depends on the structure of the material. While for the  $I_C^{RS} = 0.82$  material  $\sigma_D$  decreases, an increase is observed for the  $I_C^{RS} = 0.71$  material as a result of a storage in air atmosphere. The airbreak/annealing cycles can be observed still after many cycles with no fatigue or the appearance of any irreversible effect.

The question arises, how far the observed effects of the various structure compositions can be related to each other and/or have the same origin. Taking into account the low energies required for the air-exposure/annealing cycles one can exclude the possibility of breaking up and annealing of Si-DB as a possible origin for the varying  $N_S$ . One could also speculate that adsorption leads to a strong

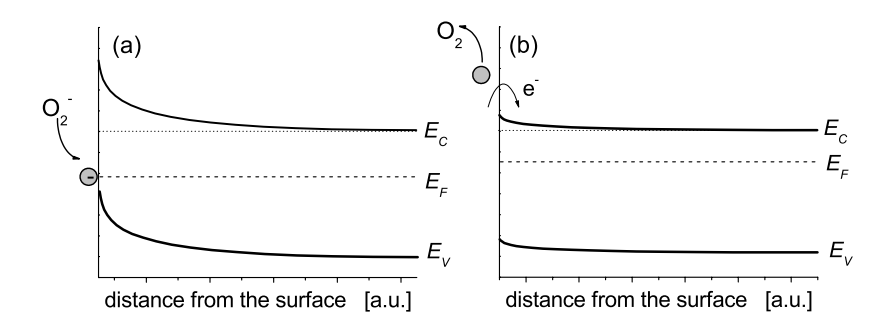


**Figure 6.14:** Energy band bending and Fermi level shift due to (a) the adsorption and the (b) desorption of oxygen on surface of  $\mu$ c-Si:H.

band bending, which could result in a bond breaking via weak-bond dangling bond (WB-DB) conversion, similar to the field effect and doping induced defect creation found in a-Si:H [167]. However, it is difficult to fit the reversibility of the observed effects with the WB-DB conversion. Taking the reversible changes of  $\sigma_D$  into account, the adsorption of oxygen seems to be a most likely candidate [20] to explain the observed metastable effects in ESR and electrical conductivity. In fact, while the material is in contact with air, additional surface states can arise due to the adsorption of atmospheric gases. The following models have been mainly developed and have widely been used to explain the gas sensing properties of semiconducting oxides, like SnO<sub>2</sub> and ZnO [168, 169, 170, 171, 172].

As determined by Hall measurements, for intentionally undoped  $\mu$ c-Si:H one generally observes n-type behavior. The in-diffusion of oxygen along the column boundaries and the adsorption of  $O_2$  on the surface of the crystalline columns will therefore capture an electron from the conduction band forming an  $O_2^-$  state. The capturing of the electron is equivalent to the occupation of a localized surface state, induced by the adsorption of  $O_2$ . This is possible, because the energy level of the  $O_2^-$  state is below the Fermi level of the material without the presence of oxygen. This can be described by the following reactions

$$\begin{aligned}
O_{2(gas)} &\Rightarrow O_{2(ads)} \\
e^- + O_{2(ads)} &\Rightarrow O_{2(ads)}^-.
\end{aligned} (6.1)$$

The transfer of charge carriers will lower the Fermi level and the accumulation of trapped charge carriers at the column boundary will lead to a band bending in the material. This is shown schematically in Fig. 6.14. The changes of the dark conductivity  $\sigma_D$  are therefore a result of two different, however interconnected effects. While the trapping of charge carrier at the surface leads to changes in

the free carrier concentrations, the increasing barrier height handicaps the charge carrier transport. As dark conductivity in  $\mu$ c-Si:H is usually measured perpendicular to the growth direction, a charge carrier has to cross a number of column boundaries before it reaches the other electrode (compare Fig. 2.1). To overcome the barriers formed at the column boundaries, a charge carrier has to be thermally excited. This model of barrier-limited transport is based on the ideas of Seto [41] and has been successfully applied to explain the transport behavior of polycrystalline silicon. In the case that the free charge carrier concentration in the columns is higher than the density of surface states induced by adsorption of  $O_2$  the current is given by

$$I = const \cdot \exp\left(\frac{-E_B}{kT}\right) \tag{6.2}$$

and is so extremely sensitive to the barrier hight  $E_B$ . This assumption is plausible if one bears in mind that a typical surface adsorption will exchange charge carriers of the order of  $10^{10} - 10^{12}$  e/cm<sup>2</sup> [173]. Taken a charge carrier concentration of  $N_D = 10^{17}$  cm<sup>-3</sup> in the bulk of  $\mu$ c-Si:H [96] and a column diameter of 200 nm the free charge carrier concentration is about one order of magnitude higher than the number of surface states created by adsorption. Upon annealing in argon atmosphere, the desorption of oxygen will lead to a re-emission of the trapped charge back into the bulk. The band bending will decrease to its initial state and restoring the values of the electrical conductivity.

The considerations made above can explain the reversible effects observed in highly crystalline porous material  $I_C^{RS}=0.82$  very well. For highly crystalline but compact material  $I_C^{RS}=0.71$ , on the other hand, the conductivity shown in Fig. 6.9 strongly deviates from the characteristic found in  $I_C^{RS}=0.82$  material. While for the later one  $\sigma_D$  decreases, for  $I_C^{RS}=0.71$  material  $\sigma_D$  increases upon contact with air

The key-issue for the different behavior is the porosity. While in highly crystalline porous material atmospheric gases can easily diffuse along the column boundaries leading to the creation of surface states, the compact structure of  $I_C^{RS}=0.71$  prevents the diffusion of atmospheric gases into the material. One would therefore not expect any strong influence on the barrier height at the column boundaries upon contact with air atmosphere. However, oxygen can still be adsorbed at the film surface. Providing that the charge carrier density within the film is small, i.e. the Fermi level position is close to the mid gap, the creation of  $O_2^-$  states at the film surface might lead to the induction of holes. In fact, due to the capture of an electron by the surface state, holes are induced into the film, resulting in an increasing  $\sigma_D$ . Adsorption processes could therefore also account for the meta-stability of  $\sigma_D$  in highly crystalline compact material. This assumes that the  $O_2^-$  surface states lies energetically below mid gap, which however re-

mains speculative. However, this process was recently suggested to account for the properties of porous silicon gas sensors [174].

Can this adsorption process, as described above, also account for the reversible effects found in the ESR signal? Caused by the band bending, states located in surface near regions become depopulated. The particular details are difficult to predict as they will depend on the relationship between the effective correlation energy, the energy position and the energy distribution of the defects. In a simple picture, if one starts from a negatively charged  $D^-$  state, depopulation will lead to a neutral  $D^0$  state and one would observe an increase of the ESR signal intensity. Upon annealing in argon atmosphere, the desorption of oxygen will lead to a reemission of the trapped electrons back into the film restoring the initial values of  $N_S$ .

Compatible with the change in occupation of near-surface states is the effect of annealing at  $160^{\circ}\text{C}$  in Ar. In highly crystalline porous material ( $I_C^{RS} = 0.82$ ) this leads to the appearance of a strong CE signal, resulting from a shift of the Fermi level into the conduction band-tail (compare Chapter 5). The observation is in agreement with the direction and magnitude of changes observed in  $\sigma_D$  and indicates considerable n-type background doping of this nominally un-doped sample. A comparison with the data measured in Chapter 5 the magnitude of the CE resonance will correspond to a doping concentration of about  $N_D \approx 7$  ppm. Because of the reversibility of these effect upon contact with air, one can exclude thermally induced dopant activation as the dominating process. However, the reason for this strong shift of  $E_F$  in  $I_C^{RS} = 0.82$  material remains yet unknown.

It is interesting, that the changes in  $N_S$  are due to an increasing number of spin states at g=2.0052 while the resonance at g=2.0043 remains unaffected. The data suggest that both states, db<sub>1</sub> and db<sub>2</sub>, are located in different microscopic environments, spatially separated from each other. In fact, from the study of intrinsic  $\mu$ c-Si:H material, it was concluded that the db<sub>2</sub> signal arises from states located at the column boundaries, while on the other hand, there are some indications that the db<sub>1</sub> is connected to the crystalline grains. Taking into account a Debye screening length of

$$L_D = \sqrt{\frac{\varepsilon \varepsilon_0 kT}{N_D q^2}} \approx 12.5 \text{ nm}$$
 (6.3)

and a diameter of the columnar clusters of 200 nm, the observed processes are restricted to the surface of the crystalline columns. In other words, the depopulation of  $D^-$  states, caused by the band bending upon contact with air, only occurs in regions close to the surface. Because the increasing ESR signal intensity is borne by the db<sub>2</sub> states, it is tempting to relate the db<sub>2</sub> signal to states located at the columnar surface. On the other hand, the fact that the db<sub>1</sub> states remain unaffected by

the treatment suggest that they are located within the crystalline columns.

#### **6.3.2** Irreversible Effects caused by Oxidation

Unlike the reversible adsorption effects, the effects of oxidation on the ESR signals are not reversible by moderate temperature annealing or long time storage in inert gas or in vacuum. The process seems to be thermally activated, starting already at room temperature. The non-reversible occurrence of additional spins by annealing in oxygen is linked to this oxidation process. The effect is again closely related to the size of the surface area and the fact that the increase of  $N_S$  after annealing in O<sub>2</sub> or air can be restored by an HF dip supports that the observed effect is a surface process. The depopulation of CE states due to creation of Si-O related defect states supports the assumption that the energy of additional states observed in ESR is below the energy of conduction band-tail states. In this context, it is remarkable that electrons located in conduction band-tail states seems to be transferred to states created by oxidation and are not involved in compensation effects, as reported in Chapter 5. However, more evidence from experimental data are need to resolve this issue. Infrared as well as secondary ion mass spectroscopy combined with ESR and electronic conductivity of material in various oxidation states seems a promising task for the future.

# 6.4 Summary

The instability and metastability phenomena in  $\mu$ c-Si:H are numerous and are a matter of great concern for the understanding of the material properties as well as for possible technological applications of these materials. It appears, that the amplitude of these changes is connected to the surface area of the material.  $N_S$ changes due to adsorption are highly pronounced for  $I_C^{RS} = 0.81$  material, which is known to be very porous. At lower  $I_C^{RS}$  the effects are much smaller or absent. With increasing amorphous content the material is getting more compact and the additional amorphous phase, incorporated between the crystalline columns, leads to a better termination of the crystal surfaces, which are therefore less susceptible for adsorption of impurities and atmospheric gases. Note, that the optimum  $\mu$ c-Si:H material for solar cells is found close to growth conditions of amorphous material. The fact, that the changes only affect the db<sub>2</sub> resonance (g=2.0052) supports an earlier assumption that the related defect is separated from the defect resulting in the db<sub>1</sub> line (g=2.0043). Most likely, the db<sub>2</sub> defect is located at or near the grain boundaries, while the db<sub>1</sub> states is located within the crystalline columns. An alternative explanation for the increase of the  $db_2$  resonance would relate the resonance with states of the adsorbed species.

# **Chapter 7**

# Transient Photocurrent Measurements

In the previous Chapters, the density and distribution of defects as well as bandtail states in  $\mu$ c-Si:H were studied. The presence of these localized states strongly influences the charge carrier transport in the material. Time resolved charge transport measurements are a powerful tool, which have been successfully applied to e.g. a-Si:H [97] to study charge transport mechanisms and electronic states associated with the transport. In  $\mu$ c-Si:H there is, of course, a wide range of possible structure compositions giving rise to the possibility that transport properties may also vary considerably. In this section, a study of hole drift mobility measurements performed on material prepared under conditions for optimum solar cell performance will be presented. Various samples, as listed in table 7.1, have been prepared as described in section 3.3.2 and charge carrier transport has been investigated by time-of-flight experiments. The specimens can be divided into two groups. While for samples C and D the depletion width  $d_w$  extends over the entire i-layer thickness  $d_i$ , for samples A and B this is not the case.

#### 7.1 Electric Field Distribution

The standard time-of-flight analysis requires a uniform distribution of the externally applied field within the specimen. The method relies on the fact, that a typical time-of-flight sample acts as a capacitor, thus Eq. 3.13 applies. Ideally, the film is fully depleted and the depletion layer  $d_w$  extends over the entire sample thickness  $d_i$ , indicating a uniformly distributed electric field within the specimen. While this behavior is typically observed for a-Si:H diodes, capacitance measurements performed on microcrystalline silicon diodes suggest that in  $\mu$ c-Si:H this is not always the case [143, 144].

**Table 7.1:** Properties of microcrystalline silicon *pin* diodes used in the TOF experiment. Listed are the Raman intensity ratio  $I_C^{RS}$ , the i-layer thickness  $d_i$ , the depletion width  $d_w$ , the capacitance C(4V,300K), and  $C_{geom}$  calculated from the geometry (see section 7.1).

Sample	$I_C^{RS}$	<i>d<sub>i</sub></i> [μm]	d <sub>w</sub> [μm]	C(4V,300K) [pF]	$C_{geom}$ [pF]
A	0.71	4.0	1.3	60	20
В	0.70	6.5	1.7	46	13
C	0.60	3.4	3.4	22	22
D	0.61	4.3	4.3	18	18

#### **Depletion Layer Capacitance**

Capacitance measurements have been performed on samples A-D (see table 7.1) for different applied voltages V and varying temperatures T, as described in section 3.13. The measured values of the capacitance are plotted in Fig. 7.1. Also indicated are the geometrical values  $C_{geom}$  calculated using Eq. 3.13 with  $d_w = d_i$ . In Fig. 7.1 (a) the measured values of the capacitance are plotted as a function of the applied voltage, measured at a temperature of 300K. One can observe that, from the characteristic of the capacitance the specimens can be divided into groups. While for sample C and D the capacitance is independent of the applied voltage and agrees very well with the values expected from the geometrical dimensions, samples A and B significantly deviate from this behavior. For samples A and

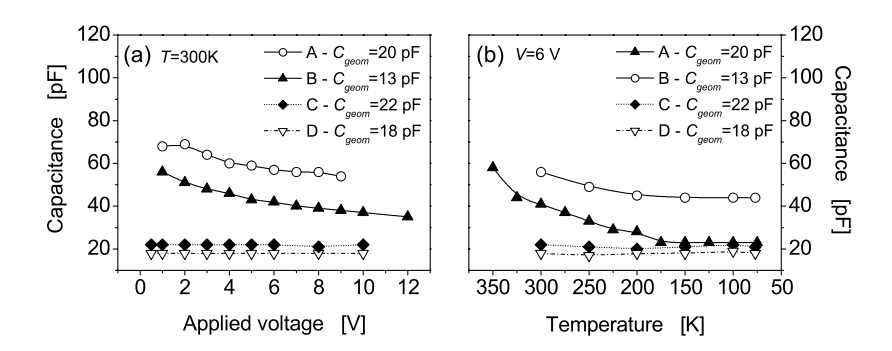


**Figure 7.1:** Sample capacitance of the samples A-D versus (a) the externally applied voltage and (b) the temperature. The geometrical capacitance  $C_{geom}$  shown in the legend has been calculated using Eq. 3.13 and  $d_w = d_i$ .

B the capacitance decreases with increasing specimen thickness  $d_i$ , as expected from Eq. 3.13 (see table 7.1). However, for both samples the measured values are higher than one would expect from the geometry of the structure. With increasing applied reverse voltage the capacitance decreases, indicating an increasing depletion layer width. The capacitance also decreases with decreasing temperature (see Fig. 7.1 (b)). However, even for the highest voltage of V = 12 V or the lowest temperature, the capacitance of samples A and B deviates considerably from  $C_{geom}$ . The excess of C indicates that the depletion width  $d_w$  (see table 7.1) does not extend over the whole sample thickness and the electric field is concentrated in only a fraction of the sample.

From the capacitance measurements the specimen investigated can be divided into two groups. For samples C and D the depletion width  $d_w$  is close to the physical layer thickness  $d_i$ . This criterion corresponds to a nearly uniform electric field across the intrinsic layer during the time-of-flight experiment. On the other hand, sample A, B do not satisfy this criterion. The shortage of the depletion width, compared to the i-layer thickness, indicates that the electric field is not uniformly distributed and rather concentrated to only a fraction of the sample.

#### 7.2 Transient Photocurrent Measurements

Transient photocurrent measurements were applied to all samples listed in table 7.1, in order to determine the properties of the drift of holes. The first part of this section deals with the transients taken of specimens A and B. Since a detailed analysis of these transients failed due to the unknown electric field distribution, results will be discussed qualitatively only. In the second part photocurrent transients of specimens C and D are presented. As shown above, for both samples the electric field, applied during in the TOF experiment, is uniformly distributed across the i-layer and the transients could be analyzed in terms of a standard time-of-flight analysis.

#### 7.2.1 Non-Uniform Electric Field Distribution

Although the electric field distribution within samples A and B is not uniform, which is a basic requirement for a TOF experiment to be suitable, transient photocurrent measurements were also done on these samples. In Fig. 7.2 photocurrent and photocharge transients for different applied voltages measured for specimens A and B are shown. All transient currents were taken at a temperature of 300K; the photocharge transients were determined by integrating the currents. The samples have been illuminated through the n-layer using an excitation wavelength of

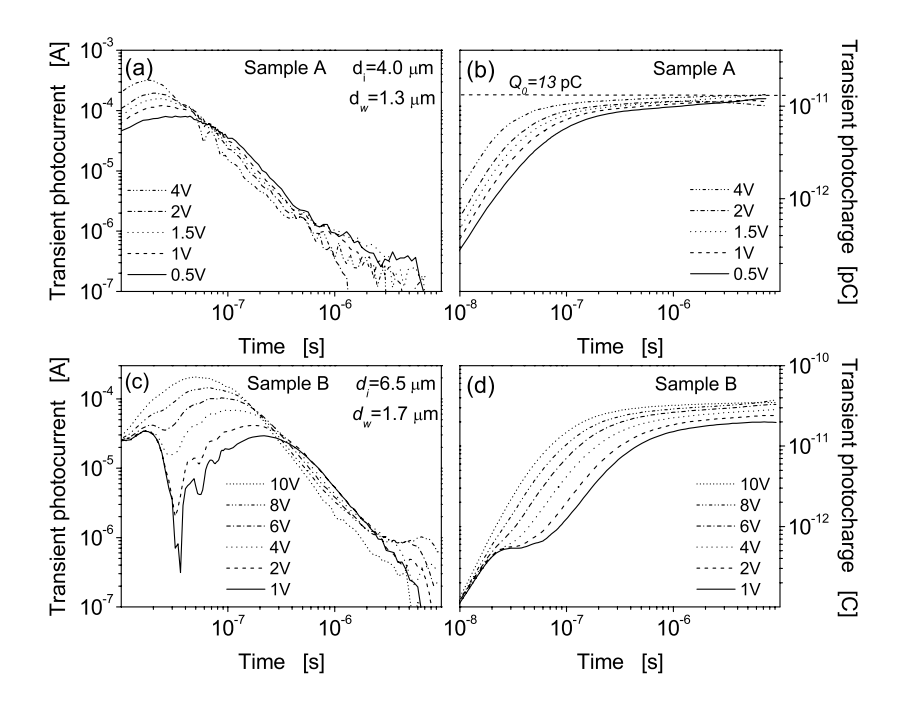


**Figure 7.2:** Transient photocurrent and photocharge measured for (a, b) sample A and sample B are shown (a, b) and (c, d), respectively. The transients were taken at a temperature of T = 300K for different applied voltages at room temperature.

 $\lambda$ =500 nm ( $E_{Photon}$ =2.48eV). For samples A and B with a Raman crystallinity of  $I_C^{RS}$  ~0.7 the absorption coefficient is  $\alpha \approx 5.5 \times 10^4$  cm<sup>-1</sup>, which corresponds to an absorption depth in the intrinsic layer of about 0.16  $\mu$ m [175]. While the electrons, generated very close to the n-layer, are swept away very quickly (within nanoseconds), the photogenerated holes have to traverse most of the thickness of the intrinsic layer before reaching the p-layer. Thus nearly the entire photocurrent corresponds to hole motion (see section 3.1.4 for a detailed description).

As discussed above, for both samples A and B the depletion layer width  $d_w$  is considerably lower than the real i-layer thickness  $d_i$  (see table 7.1). This indicates a nonuniform distribution of the electric field within the specimen and, therefore, unsurprisingly the transients do not show any typical shape, i.e. neither Gaussian nor dispersive transport behavior (compare section 2.3.2 and Fig. 2.4). In fact, an interpretation of the transients in terms of the properties of charge carrier transport is impossible, because of the unknown electric field distribution. However,

the transients show some interesting features which will be discussed below. In Fig. 7.2 (a) photocurrent transients of sample A are shown. Capacitance measurements have shown that the depletion layer has a width of  $d_w = 1.3 \, \mu \text{m}$  and extends to about 1/3 of the real i-layer thickness (see table 7.1). One can observe that, after an increase of the current ( $t < 2 \times 10^{-8} \, \text{s}$ ), which is caused by the RC-constant of the measurement circuit, the current starts to decrease with a power-law in time. The decrease starts at earlier times for increasing bias voltage and a "crossover" of the currents can be observed. The power-law decay is independent of the applied voltage and one does not observe any change in slope corresponding to a transit time, as expected for dispersive transport (compare section 2.3.2). The photocharge (panel (b)) determined by integrating the photocurrent transients approaches an asymptotic value at prolonged times, indicating that  $Q_0$  is still a good estimate of the photoinjected charge.

On the other hand, the transits measured on sample B show a quite unexpected behavior. The photocurrent transients and the photocharge are shown in Fig. 7.2 (c, d). For this sample, the depletion layer width extends only to one fourth of the i-layer thickness. The currents shown in panel (c) show a shape that strongly depends on the applied voltage. As for early times  $(t < 2 \times 10^{-8} \text{ s})$  the current is determined by the RC rise time of the measurement circuit, the current for e.g. the 1 V transient drops down to almost zero for about 80 ns before it increases again. The current peaks at about 200 ns before it starts to decrease with a power-law decay as observed for specimen A. In the photocharge transient plotted in panel (d) this effect is observable in a plateau at times between  $t = 2 \times 10^{-8}$  s and  $1 \times 10^{-7}$  s. With increasing voltage the time range of "zero current" becomes shorter, the effect is less pronounced and disappears for the highest voltage V = 10V. The "zero-current" and the plateau observed in the charge transients indicate that within the sample there are regions, where the energy of the externally applied field is smaller than kT and the charge carrier packet has to cross this section by diffusion. As diffusion is a statistical process no current can be observed. At the time the packet has crossed this low electric field region, the charge carrier drift can again be measured in the external circuit. With increasing applied voltage the depletion width increases and therefore the electric field penetrates deeper into the film; the effect becomes less pronounced.

Unfortunately, because of the unknown electric field distribution within the sample, the transients can not be readily analyzed to obtain drift-mobilities. Even if the field distribution were known, there are no established techniques for analyzing transients with nonuniform fields to obtain dispersive mobility parameters. The reason for the nonuniform electric field might be a high concentration of free charge carrier in this intentionally undoped material. A series of samples with different compensation levels could provide additional information [143].

#### 7.2.2 Uniform Electric Field Distribution

Unlike samples A and B, in samples C and D the depletion layer thickness  $d_w$  extends over the whole i-layer, indicating a uniform distribution of the electric field. Fig. 7.3 (a) and (c) show photocurrent transients taken at T=250K on specimens C and D for several applied bias voltages.

The transient photocurrents were measured for several bias voltages in the range between V=0 V and V=6 V. The transient at 0 V is due to the "built-in" electric field, and indeed such transients have been used to infer the internal fields (see e.g. [176]). Each transient shows two power-law segments, the "pretransit" with a fairly shallow power-law decay and the "posttransit" regime with a steep decay. This is a signature of dispersive transport (compare section 2.3.2). The currents, obtained for different voltages, do intersect, which indicates a voltage dependent transit time  $t_{\tau}$ . In other words, with increasing voltage the change in the power law occurs earlier, resulting in a "crossover" of the currents. Because the time where the change in the power law occurs is interpreted as  $t_{\tau}$ , this indicates a decreasing transit time upon increasing V. Fig. 7.3 (b, d) show the transient photocharge Q(t, V) for varying externally applied voltage obtained by integrating the transient photocurrent I(t) (shown in Fig. 7.3 (a, c)). The photocharge at longer times and for higher voltages approach a constant value, denoted as  $Q_0$ , which was used to estimate the total photogenerated charge. The fact, that the charge measurement for the higher voltages approach the same asymptotic value for the total charge of  $Q_0$ =25 pC and  $Q_0$ =20 pC for sample C and D, respectively, indicates that  $Q_0$  is likely a good estimate of the charge of photogenerated holes. It seems important to note, that the difference of  $Q_0$  between both samples is due to different laser intensities and not due to any loss of photoexcited charge carriers within the intrinsic layer. This is different for the 0 V applied voltage. Even though the photocurrent transient has the form expected for time-of-flight, it does not show the correct asymptotic photocharge. In this case holes are indeed trapped, presumably in dangling bonds, before they could reach the collecting electrode. The time required for a charge carrier to reach the collecting electrode is of the order of the deep trapping life time  $t_D$ , hence not all the photoinjected charge can be collected. In Fig. 7.4 the collected photocharge  $\mathcal{Q}(\infty)$  for sample C and D is plotted versus the externally applied voltage V. The value of  $Q(\infty)$  was determined after  $t = 6 \times 10^{-6} s$  for both samples; for higher voltages  $Q(\infty)$  saturates indicating that all the photoinjected charge has been collected. Determining the photoinjected charge from the high voltage transients, the deep trapping mobility-lifetime product  $\mu \tau_{h,t}$  can be evaluated using

$$\mu \tau_{h,t} = \frac{Q(\infty)}{Q_0} \frac{d_i^2}{(V + V_{int})},\tag{7.1}$$

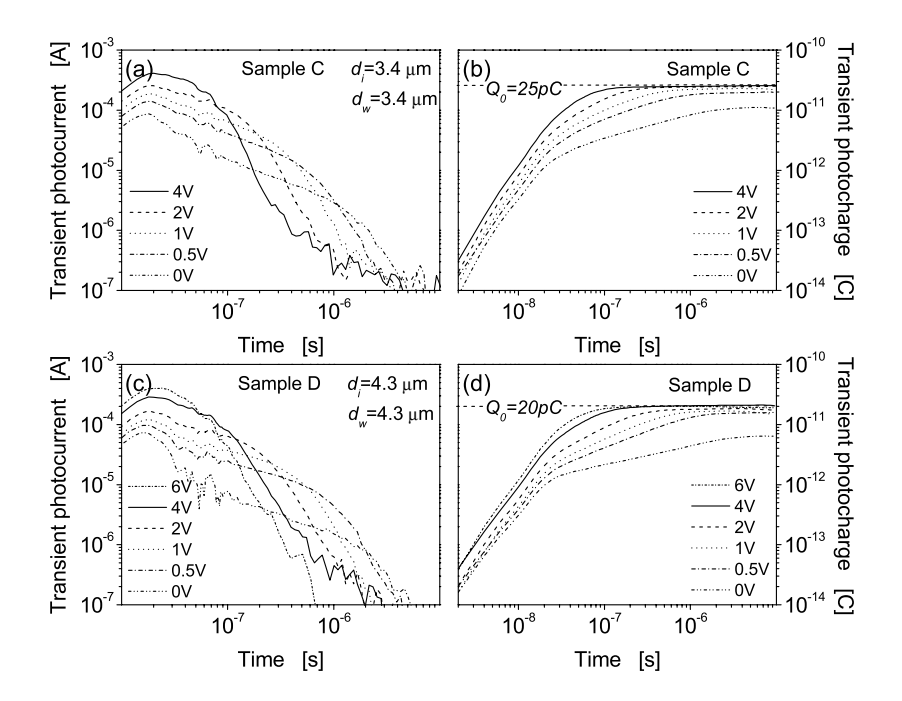


**Figure 7.3:** Panel (a) and (c) show transient photocurrents taken at T = 250K on specimen C and D for several applied bias voltages. The corresponding Q(t) (b, d) were determined by integrating the transient photocurrent. The asymptotic value  $Q_0$  is a measure of the photogenerated charge.

where V is the externally applied and  $V_{int}$  the voltage due to the built-in field of the pin structure [177]. For low voltages  $Q(\infty)$  increases linearly and from the slope a  $\mu\tau_{h,t}$  product of  $\mu\tau_{h,t}=1\times10^{-7}~{\rm cm^2/V}$  for specimen C and  $\mu\tau_{h,t}=2\times10^{-7}~{\rm cm^2/V}$  for D can be extracted. The crossing point of this line with the x-axis is an estimate of the internal voltage  $V_{int}$  caused by the built-in field of the pin-structure, which amounts to  $V_{int}=0.4~{\rm V}$  for specimen C and  $V_{int}=0.3~{\rm V}$  for specimen D. This analysis assumes that the internal field is uniform for an external voltage of V=0 V. Evidence for this assumption comes from the normalized photocurrents discussed below.

For Fig. 7.5 the transient photocurrents of Fig. 7.3 were normalized using  $I_{norm} = I(t)d_i^2/(Q_0(V+V_{int}))$ .  $Q_0$  is the total charge generated in the structure,  $d_i$  is the i-layer thickness, V is the externally applied voltage, and  $V_{int}$  is the correction for the built-in field. This normalization procedure eliminates the simple Ohmic

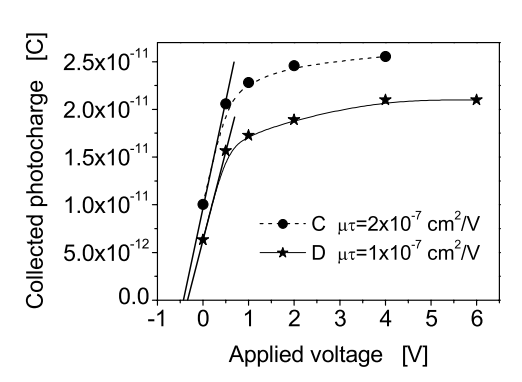


**Figure 7.4:** Total photocharge  $Q(\infty)$  of holes collected after  $t = 6 \times 10^{-6} s$  as a function of applied voltage ("Hecht Plot"). The data points were taken from Fig. 7.3 (b) and (d).

scaling of I(t) prior the transit time. If one allows for the built-in field by adding a correction of  $V_{int}$ =0.40 V and  $V_{int}$ =0.30 V to the applied voltage for sample C and D, respectively, the currents prior to the transit of the charge carriers depend linearly on the total voltage  $(V + V_{int})$ . The various transients establish what has been termed an "envelope" curve [131], illustrated as the slow decreasing line in Fig. 7.5.

Such envelope curves indicate that transport is "ohmic" and for a given time t, the drift velocity of holes in  $\mu$ c-Si:H is proportional to the electric field (Note, that the normalized photocurrent has the dimensions of a mobility (cm²/Vs)). The fact that even the 0 V transients agrees with the envelop curve indicates that the

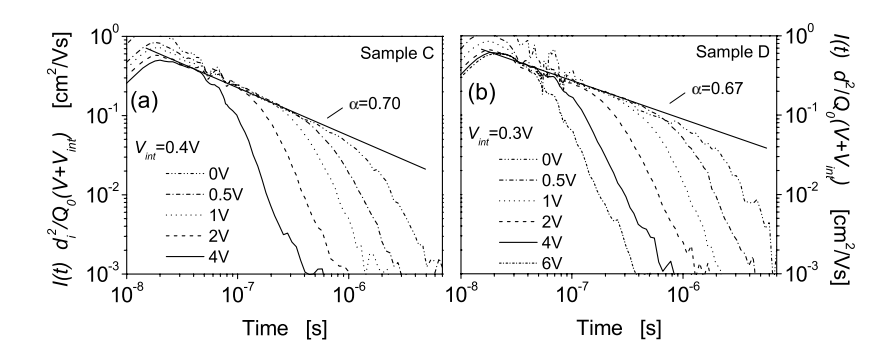


**Figure 7.5:** Normalized transient photocurrents of (a) sample C and (b) sample D. The original, as measured, transients are shown in Fig. 7.3.

assumption of an uniformly distributed internal field, made above, is valid. At this temperature, the envelope declines as a power-law  $(t^{-1+\alpha})$  where  $\alpha$ =0.70 and  $\alpha$ =0.67 are the dispersion parameter for sample C and D, respectively. From the "pretransit" regime the individual transits break at increasingly earlier times with increasing voltage. These breaks can be used to obtain a rough estimate of the transit times. For e.g. sample C the current transients exhibit "transit times" varying from about 500 ns (for 0.5 V) to 70 ns (for 4V). For earlier times there is a noticeable increase of the photocurrent above this envelope, especially for the lower voltages. As already discussed above the absorption depth of the laser light was about 160 nm, which is about 5% of the sample thickness; electron motion is thus responsible for about 5% of the total photocharge. The excess current between  $2 \times 10^{-8}$  s and  $6 \times 10^{-8}$  s is consistent with a rapid collection of this charge of electrons.

To summarize: Allowing to correct the externally applied voltage by a voltage due to the internal field the photocurrent transients show typical features expected for conventional time-of-flight interpretation. (i) Each transient can be divided in a "pretransit" with shallow and "posttransit" region with fairly steep power-law decay. (ii) The current transients exhibit "transit times" increasing with decreasing applied electric field. (iii) The charge measurement for the high voltages approach the same asymptotic value for the total photocharge, indicating that  $Q_0$  is likely a good estimate of the charge of photogenerated holes.

# 7.3 Temperature Dependent Drift Mobility

To get a closer insight into the processes determining the transport, transient photocurrents were measured in a range of temperatures between 125K and 300K. Fig. 7.6 displays, as an example, the transient photocurrent of sample C taken at V = 1V for several temperatures T in the range between 300K and 200K. The photocurrent transients show typical signs for temperature activated hole drift mobilities  $\mu_{h,T}$ . With decreasing temperature a declining magnitude of the current and a shift of the "kink" to higher values can be observed. The photocharge transients Q(t), determined by integrating the currents I(t), approach the same asymptotic value for all temperatures. This indicates that the photogeneration quantum efficiency is independent of temperature and deep trapping is negligible in the measured temperature range. The dashed line in Fig. 7.6 (b) indicates the value of half the total collected photocharge  $Q_0/2$ . The times, where the photocharge transits cross this line can be interpreted as the time where half the charge has been collected (see section 3.1.4.3 for a detailed discussion). This value will be used as an estimate for the transit time  $t_T$  used to calculate hole drift mobilities.

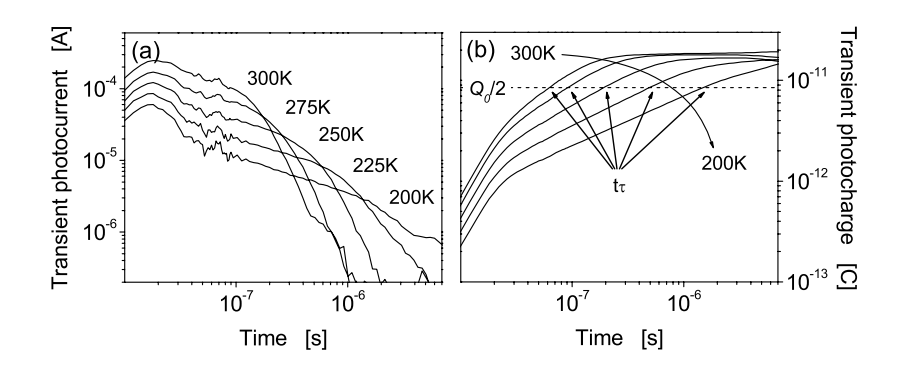


**Figure 7.6:** (a) Temperature dependence of the transient photocurrent of sample C and (b) of the transient photocharge calculated by integrating the corresponding currents in panel (a).

In Fig. 7.7 the temperature dependence for the average drift mobility of holes determined for sample C and D is illustrated. This average drift mobility is calculated as

$$\mu_{d,h} = \frac{L}{Ft_{\tau}} \tag{7.2}$$

where  $t_{\tau}$  is the transit time for a particular ratio of a hole displacement L and the electric field F. Within this work

$$\frac{L}{F} = \frac{d^2}{2(V + V_{int})} = 7 \times 10^{-8} \text{ cm}^2/\text{V}$$
 (7.3)

was used. Note, that for dispersive transport systems, drift mobilities for different materials must be compared at a specific value of L/F [131]. The straight line is a fit to the data of sample D, for which the measurement had the least scatter. However, sample C and D have essentially the same average hole drift mobility. The drift mobilities are simply activated with an activation energy of  $E_A = 0.13 \text{eV}$ .

# 7.4 Multiple Trapping in Exponential Band-Tails

For sample C and D the model of multiple trapping in an exponential band-tail [100, 101, 98, 102, 103] was applied to the drift mobility data presented in section 7.2.2. The basic features of the model, which has been successfully applied to amorphous semiconductors, are discussed in section 2.4 and appendix A. In the multiple trapping model electronic states are simply divided into transport states (where the charge carriers are mobile) and traps, which simply immobilize the

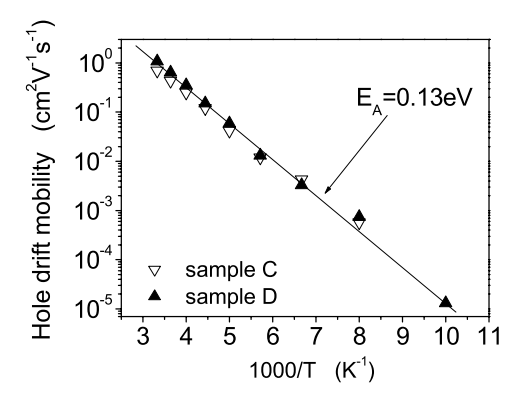


**Figure 7.7:** Temperature dependence of the average hole drift mobility  $\mu_D$  for samples C and D;  $\mu_D$  was evaluated at a displacement/field ratio  $L/F = 7 \times 10^{-8} cm^2/V$ .

charge carriers until they are thermally re-emitted into transport states. Although the physical mechanism of multiple trapping in exponential band-tails is rather complicated and involves a number of processes, the charge transport is mainly determined by the properties of the band-tail. In fact, the transport mechanism can be described by a set of only three parameters describing the band-tail. The model assumes a "band mobility"  $\mu_0$  for the holes. Measured drift mobilities are lower than this value because of the multiple-trapping of holes by localized states distributed as an exponential band-tail. The width of this band-tail, which lies just above the valence band edge, is denoted  $\Delta E_V$ . The third parameter is the "attempt-to-escape" frequency  $\nu$ , that characterizes thermal re-emission of holes from a band-tail trap back to the valence band. For fitting, the following function derived from the exponential band-tail model (see appendix A) was used:

$$\frac{L(t)}{F} = \frac{\sin(\alpha \pi)}{\alpha \pi (1 - \alpha)} \left(\frac{\mu_0}{\nu}\right) (\nu t)^{\alpha} \quad \text{with} \quad \alpha = \frac{kT}{\Delta E_V}. \tag{7.4}$$

Here L(t) is the carrier displacement after a delay time t in an electric field F. In Fig. 7.8 the open symbols represent normalized transient photocharge measurements  $Q(t)d^2/(Q_0(V+V_{int}))$  for several temperatures. It has been shown by Wang et al. [131], that for times prior  $t_\tau$  ( $t \ll t_\tau$ ) the normalized charge  $(Q(t)d^2/(Q_0(V+V_{int})))$  equals L(t)/F. The physical meaning of the applied normalization is to consider the time t which is required for a carrier to be displaced by a distance L in an electric field F. The normalized photocharge transits have been recorded at bias voltages of V=0.5 V and V=1 V for specimen C and D, respectively, and were corrected by the internal voltage  $V_{int}$ . As already discussed,

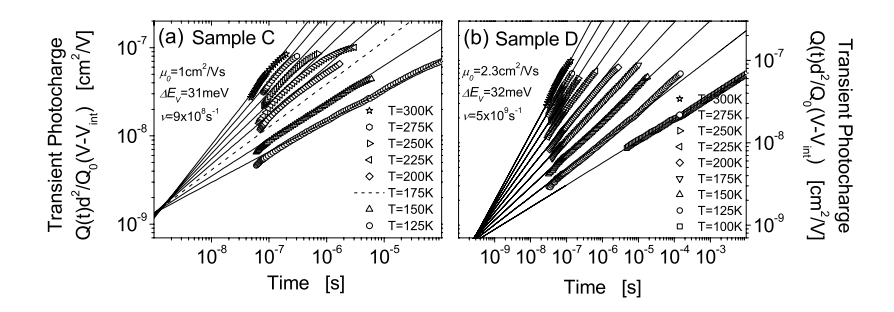


**Figure 7.8:** Symbols are the normalized photocharge measurements taken on (a) sample C (V = 0.5 V) and (b) sample D (V = 1 V) at the indicated temperatures. The solid lines are the corresponding calculations using Eq. 7.4 with the parameters indicated.

due to the absorption depth of the laser, which is 160 nm, about 5% of the charge is attributed to electron motion<sup>1</sup> and has been subtracted from the transient photocharge. The portions of these transients at early times close to the electronic rise-time ( $t < 5 \times 10^{-8}$  s) have been excised, as have the late-time portions where most holes have been collected. The solid lines in Fig. 7.8 are a fit to the experimental measurements using the parameters listed in table 7.2. Additionally, the multiple trapping parameter of a typical a-Si:H sample taken from Dinca et al. [142] are shown. From the fitting a valence band-tail width of  $\Delta E_V = 31$  meV for sample C ( $\Delta E_V = 32$  meV for sample D) was derived, which is much narrower than the widths of  $\Delta E_V = 40 - 50$  meV reported for amorphous silicon [140, 142], but is still substantially larger than the values as low as 22 meV that are reported for the conduction band-tail in amorphous silicon [131]. Remarkably, the values for the band mobility of  $\mu_0 = 1 \text{ cm}^2/\text{Vs}$  for sample C and  $\mu_0 = 2.3 \text{ cm}^2/\text{Vs}$  for D, are essentially the same as has been reported in amorphous silicon (for both electrons and holes) [131, 140, 142]. In this context it is interesting to note, that the attempt to escape frequency  $v = 9 \times 10^8 \text{ s}^{-1}$  ( $v = 5 \times 10^9 \text{ s}^{-1}$ ) is approximately two to three orders of magnitude smaller than values that have been reported for holes in a-Si:H [140, 142].

#### 7.5 Discussion

Transient photocurrent measurements have been performed on microcrystalline material prepared under plasma-deposition conditions similar to those where best solar cell performance can be achieved. As pointed out above, for conventional

<sup>&</sup>lt;sup>1</sup>For a detailed discussion of the topic see section 3.1.4

**Table 7.2:** Multiple trapping fitting parameters

Multiple trapping Parameter	μc-Si:H sample C	μc-Si:H sample D	a-Si:H ref. [142]
Valence band mobility $\mu_0$ [cm <sup>2</sup> /Vs]	1.0	2.3	0.7
Band-tail width $\Delta E_V$ [meV ]	31	32	45
Attempt-frequency $\nu$ [s <sup>-1</sup> ]	$9 \times 10^{8}$	$5 \times 10^{9}$	$1 \times 10^{12}$

time-of-flight measurements, estimation of drift mobilities is best done in samples for which the depletion width  $d_w$  is close to the physical layer thickness  $d_i$ , which corresponds to a nearly uniform electric field across the intrinsic layer during the time-of-flight experiment. As can been seen in table 7.1 this criterion is not always fulfilled for the specimens investigated. In this section, the data of the samples where a standard time-of-flight analysis could be successfully applied will be summarized and discussed in more detail.

#### 7.5.1 Photocurrent and Photocharge Transients

The photocurrent and photocharge transients presented in section 7.2.2 show several features expected for a conventional time-of-flight interpretation. First, the charge measurements for the higher voltages approach the same asymptotic value for the total photocharge  $Q_0$ . This indicates that  $Q_0$  is likely a good estimate of the charge of photogenerated holes and that for the higher voltages no loss of photoexcited charge carriers occurs, e.g. due to deep trapping. Plotting the currents on a log-log scale, the photocurrent decays consist of two linear branches, indicating a power-law behavior typical for dispersive transport. Additionally, the current transients exhibit "transit times" (where the power-law decay steepens markedly) varying from about 500 ns (for 0.5 V) to 70 ns (for 4 V). Even the 0 V transient has the form expected for time-of-flight, but does not have the correct asymptotic photo-charge. It seems reasonable that for 0V bias voltage applied the holes were ultimately trapped by deep levels (not band-tail states) during transit. Plotting the collected photocharge versus the voltages, a deep-trapping mobility-lifetime product for holes  $\mu \tau_{h,t}$  of about  $1 \times 10^{-7}$  cm<sup>2</sup>V could be evaluated. This value is in quite good agreement with earlier reports from Brueggemann et al. [23]; however, Juška and coworkers found a value which is about one magnitude lower than the one reported here [178]. These Hecht plots (see Fig. 7.4) have also been used to determine the internal field caused by the pin structure of the specimen. The obtained values of  $V_{int} = 0.3 \text{ V}$  and 0.4 V are quite reasonable and expected for a semiconductor device with a band gap of  $E_G = 1.1$  eV. Considering the internal electric field, the normalized currents shown in Fig. 7.5 establish an "envelope" curve, indicating that, for a given time, the drift of holes depends linearly on electric field.

#### 7.5.2 Hole Drift Mobilities

The drift mobilities have been evaluated using Eq. 3.9. At room temperature hole drift mobilities of  $\mu_{d,h} \approx 1 \text{ cm}^2/\text{Vs}$  are obtained from these results. Additionally, temperature dependent photocurrent transients have been recorded in a range between 100K and 300K. The average drift mobility was evaluated at a particular "displacement/field" ratio of  $L/F = 7 \times 10^{-8}$  cm<sup>2</sup>/V. The hole drift mobilities derived are much larger than that of a-Si:H, where typical values are about two orders of magnitude smaller [142]. However, a direct experimental comparison at the same value for L/F is not possible, because the transit times  $t_{\tau}$  in amorphous silicon expected for this L/F value would by far exceed the deep trapping life time  $\tau_d$ . Thus, holes would already be captured by deep traps without any chance of release before they can reach the collecting electrode. Plotting  $\mu_{d,h}$  in an Arrhenius plot shows that the hole drift mobility is simply activated with an activation energy of  $E_A = 0.13$  eV. The physical meaning of  $E_A$  for multiple trapping in an exponential distribution of traps is still unclear. It has been suggested that  $E_A$  corresponds to an average energy required for a charge carrier trapped to release it above the mobility edge [100], but does not describe any particular feature, like a band-tail width or the depth of any particular trap.

Although electron and hole transport are crucial properties of these films, there are only few conclusive data regarding the drift mobilities of these carriers in  $\mu$ c-Si:H, and even less understanding of the physics governing carrier drift. The main experimental problem has been the high dark conductivity of many of the microcrystalline materials, which militates against conventional photocarrier time-of-flight estimation of drift mobilities. Mobility estimates have been reported using time-of-flight on specially compensated samples [143] and also using a novel "photo-CELIV" approach [179]. The results presented here differ qualitatively from these works performed on different samples of  $\mu$ c-Si:H, which found only a weak temperature-dependence [143, 179] and a strong electric-field dependence of the hole drift mobility [179]. The previous work differs from this both in samples measured and methods applied. However, recent work also performed on one sample prepared under conditions for optimized solar cells agrees in both the magnitude of the hole drift mobility and activation energy of  $\mu_{d,h}$  [49].

#### 7.5.3 The Meaning of Multiple Trapping

One approach to analyzing mobilities in polycrystalline materials is to invoke the effective masses, that would obtain for electrons and holes in the single crystal, and assume that the grain boundaries act as scatterers or barriers and as the locus for traps for the carriers [42]. It is instructive to use this approach crudely to calculate an "effective-mass carrier mobility" for holes  $\mu_h^{e.m.}$  utilizing the expression  $\mu_h^{e.m.} = v_{th} l/(kT/e)$ , where  $v_{th}$  is the "thermal velocity" for holes (about  $10^7$  cm/s in c-Si near room-temperature)<sup>2</sup> and l is a scattering length. If the scattering length is identified with a typical crystallite size of 3 nm, one infers  $\mu_h^{e.m.} = 120$  cm<sup>2</sup>/Vs, which is about 100 times larger than the estimate in Table 7.2. The effects of traps and barriers do not seem to explain the discrepancy for the samples, since these were already (implicitly) incorporated in the analysis that led to the estimate  $\mu_0 = 1$  cm<sup>2</sup>/Vs.

It is therefore most likely that the existence of band-tail states strongly effects the charge carrier transport. The disorder within the investigated material is sufficient to strongly alter the band edge states from their crystalline counterparts. In particular, a mobility-edge has been formed within the band-tail<sup>3</sup> (i.e. states lying deeper in the energy gap are localized).

The mobility-edge has been widely applied to amorphous semiconductors [97, 131], and has recently been applied to microcrystalline samples with a large fraction of amorphous "tissue" [73]. Here the suggestion is that it also applies to samples that are predominantly crystalline. In the mobility-edge model, hole states with energy levels below the mobility-edge ( $E < E_V$ ) are completely delocalized (by definition), although with very different wave functions than the effective-mass states of crystals. Hole states lying above the mobility-edge ( $E > E_V$ ) are localized. Both analytical and computational studies of mobility-edges [164, 180] indicate that the localization radius for a hole state grows very rapidly, and may even diverge, as the energy state approaches the mobility-edge. It is not clear theoretically how particular atomic-scale features such as "strained bonds" are incorporated into the band-tail states.

The estimates of 31 meV and 32 meV (see table 7.2) for the microcrystalline material seem unremarkable in the context of work on holes in amorphous silicon, which yields values in the range 40 - 50 meV. It is worth noting, that disorder affects holes and electrons very differently. The conduction band-tail in amorphous silicon has a width around 22 meV [97, 131]. Electron properties in samples quite

<sup>&</sup>lt;sup>2</sup>The concept of a "thermal velocity"  $v_{th} = (2k_BT/me)^{1/2}$  is based on effective-mass theory, and has no meaning in other transport models.

<sup>&</sup>lt;sup>3</sup>The multiple-trapping model invokes a "transport edge" that most workers associate with Nevill Mott's "mobility-edge;" however, alternate views have been proposed, in particular "hopping only" and "potential fluctuation" models.

similar to the present ones have been studied using post-transit time-of-flight [73]. However the finding was that band-tail multiple-trapping did not apply for these transients. An interesting possibility is therefore that electron transport may be governed by effective masses in exactly the same material for which holes require a mobility-edge approach. The fact that the hole band-mobility  $\mu_0$  is about the same in the present microcrystalline samples and in amorphous silicon seems to support the mobility-edge interpretation, and more broadly suggests that a value near 1 cm<sup>2</sup>/Vs may be a universal property of a mobility edge. Such "universality" is also suggested by the fact that electron band-mobilities in amorphous silicon are also around 1 cm<sup>2</sup>/Vs [97, 131]. Interestingly, a band mobility of 1 cm<sup>2</sup>/Vs is not an obvious implication of the existing theoretical treatments of mobility-edges.

It is quite interesting, that the value of the attempt-to-escape frequency for microcrystalline silicon is substantially (about 100 times) smaller than the lower values reported for a-Si:H. However, even for a-Si:H, there is no well-accepted physical interpretation for this parameter. One often-mentioned interpretation is that  $\nu$  be identified as a "typical phonon frequency," but this association fails to explain either the very low magnitudes or the enormous range of magnitudes that have been reported experimentally [181, 182]. Yelon and Movaghar have suggested that multi-phonon effects lead to the variations and this perspective has been applied by Chen et al. to drift mobility measurements [183]. Another possibility originating with high-field drift mobility measurements in a-Si:H has been that  $\nu$  reflects the bandedge density-of-states  $g(E_V)$  [184], which suggests that the present measurements be interpreted as indicating a substantially lower value for  $g(E_V)$  in microcrystalline than in amorphous silicon. Plainly, one needs more clues from experiment about the meaning of this parameter, however it seems possible that its dramatic lowering in microcrystalline silicon could be providing it.

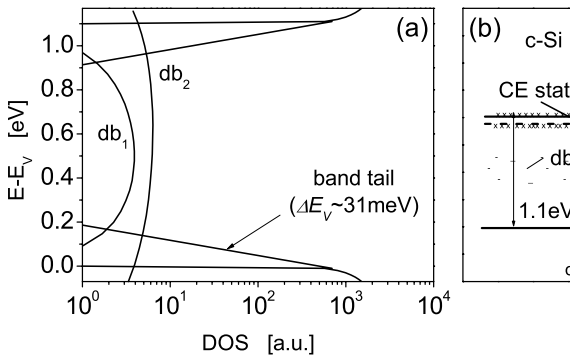
## **Chapter 8**

## **Schematic Density of States**

In Chapter 4-7, a study of electronic states located in the band gap of  $\mu$ c-Si:H using different experimental techniques and conceptional methods was described. However, all these experiments have certain limitations and therefore provide information only in a limited range. The aim of this section is to combine this information into a schematic picture of the density of states in both a spatial and energetic sense.

From the results obtained in the study of hole drift-mobilities in highly crystalline  $\mu$ c-Si:H it could be deduced that the disorder within the investigated material is sufficient enough to strongly alter the band-edge states and affects the charge carrier transport. Applying the model of multiple trapping it could be shown that the band-tail falls exponentially towards the gap with a band width of  $\Delta E_V \approx 31$  meV. The existence of conduction band-tail states could be observed by the well known CE resonance found in n-doped  $\mu$ c-Si:H material, but neither the shape nor a typical width can be derived from these data. However, recent investigations using photoluminescence suggest that an exponential distribution also applies for the conduction band-tail [75].

The ESR signal of intrinsic microcrystalline silicon shows an asymmetric line shape which can be described by two Gaussian distributions  $db_1$  and  $db_2$  at g-values of g=2.0043 and g=2.0052, respectively. The results presented in this work suggest that these contributions are independent states located in different microscopic environments. So far the exact location of the states remains unknown. However, combining the results obtained in this work some speculations can be made. The energetic position within the band gap can be determined from the study of n-type material presented in Chapter 5. Together with the data derived from transient photocurrent measurements presented in Chapter 7, a schematic picture of the density of states for highly crystalline material can be drawn, as shown in Fig. 8.1 (a). To provide a comprehensive view on the DOS, the energetic distribution of the  $db_1$  and  $db_2$  states within the band gap has been included,



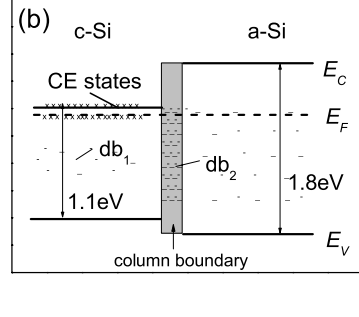


**Figure 8.1:** (a) Schematic picture of the DOS of highly crystalline material as derived from the results of this work. The distribution of the  $db_1$  and  $db_2$  states below mid-gap has been taken from reference [30] and [40]. (b) Schematic band diagram of the transition region between the crystalline and disordered phase in  $\mu$ c-Si:H (see the text for details).

that have been taken from reference [30] and [40], respectively. It can be seen that the energy distribution of the db<sub>1</sub> signal is rather concentrated within the crystalline gap of  $E_G = 1.1$  eV, while the db<sub>2</sub> resonance strongly overlaps with the conduction band-tail. It was therefore suggested, that the db<sub>2</sub> resonance in highly crystalline material are spatially separated from CE states presumably located at the columnar boundaries. This was also concluded in earlier investigations [165]. Additional support for this thesis comes from the study of intrinsic  $\mu$ c-Si:H prepared at different  $T_S$ . Due to the higher deposition temperatures hydrogen desorbs during the process. As there are a number of indications that the bonded hydrogen is located at the column boundaries, terminating dangling bond defects, it is therefore tempting to relate the higher  $N_S$  to a poor surface passivation caused by the hydrogen desorption. In Chapter 4 it was argued that the increasing  $N_S$ is borne by an increasing number of db<sub>2</sub> states, suggesting that these states are located at the column boundaries. The assignment of the db2 resonance to surface states located at the column boundaries is supported by the reversible effects on the ESR signal investigated in Chapter 6. These processes were attributed to the adsorption of oxygen at the columnar clusters. As the adsorption mainly effects the occupation of near surface states, the change of the db<sub>2</sub> resonance indicates that the origin of this line are states within this region. Quite surprisingly, the db<sub>1</sub> resonance at g=2.0043 stays unaffected by these processes. On might therefore conclude that the origin of these states is within the crystalline columns, which is in agreement with an energetic distribution confined within the crystalline band gap. In conclusion, one can draw a schematic band diagram for microcrystalline silicon as shown in Fig. 8.1 b, which illustrates the transition between crystalline and amorphous phase in  $\mu$ c-Si:H. It is important to note, that the amount of both phases varies considerably as a function of the deposition conditions. While in material exhibiting the highest crystallinity no amorphous phase can be observed and the structure consists only of crystalline columns and column boundaries, well beyond the transition to amorphous growth crystallites are highly diluted in an amorphous matrix.

All results summarized in this section indicate that majority of  $db_2$  states are located at the columnar surfaces, while the states resulting in the  $db_1$  resonance are located within the crystalline grains. With increasing hydrogen or amorphous content the spin density decreases, indicating that  $db_2$  states can be passivated by hydrogen, with an amorphous tissue around the crystallites acting as a passivation layer.

## **Chapter 9**

#### Summary

In the present work, the electronic properties of microcrystalline silicon films have been studied by using various experimental techniques and a number of concepts and models used to explain them. Paramagnetic states in  $\mu$ c-Si:H have been investigated for a large variety of structure compositions ranging from highly crystalline, with no discernable amorphous content, to predominantly amorphous material, with no crystalline phase contributions. For this material range, the density of states within the band gap was studied by electron spin resonance (ESR) and electrical conductivity. Moreover, the hole transport properties in highly crystalline material were studied by transient photocurrent measurements and have been successfully interpreted by the model of multiple trapping in an exponential band-tail.

The spin density  $N_S$  in  $\mu$ c-Si:H films is strongly dependent on the structure composition of the material. The highest  $N_S$  is always found for material with the highest crystalline volume fraction. With increasing SC during the process, the spin density decreases, which was attributed to an increasing hydrogen content, terminating unsaturated dangling bonds. Moreover, the additional amorphous phase content incorporated between the crystalline columns acts as a passivation layer, leading to a better termination of unsatisfied bonds at the surface. The strong dependence of  $N_S$  on the deposition temperature  $T_S$ , found in HWCVD material, was attributed to an increasing desorption during the deposition.

Generally, the ESR signal of intrinsic microcrystalline material shows contributions of two resonances at g-values of 2.0043 (db<sub>1</sub>) and 2.0052 (db<sub>2</sub>), independent of the particular deposition process and structure composition. The relative contributions of the individual lines changes as a function of the crystalline volume content. While the ESR spectra of low defect material in the highly crystalline regime are dominated by the resonance at g=2.0043, with increasing amorphous content the intensity ratio is clearly shifted towards the db<sub>2</sub> resonance. An

increasing intensity of the  $db_2$  resonance is also observed as a result of increasing  $T_S$ .

Reversible and irreversible changes in the ESR signal and the conductivity found in  $\mu$ c-Si:H due to atmospheric effects are closely connected to the structure composition, in particular the active surface area. The porous structure of highly crystalline material leads to the in-diffusion of atmospheric gases, strongly affecting the density of surface states. Two processes have been identified, namely adsorption and oxidation. Both processes lead to an increase of  $N_S$ . In the case of adsorption the increase could be identified as arising from changes of the db<sub>2</sub> resonance, while the intensity of the db<sub>1</sub> resonance remains constant. With increasing amorphous content the magnitude of both adsorption and oxidation induced changes decreases as a result of a higher compactness of the films. The adsorption of  $O_2$  may be reversed by moderate temperature annealing, while a chemical treatment in HF is required to reverse the effects caused by oxidation.

Measurements on n-doped  $\mu$ c-Si:H films were used as a probe for the density of gap states. The results confirm that the doping induced Fermi level shift in  $\mu$ c-Si:H, for a wide range of structural compositions, is governed by compensation of defect states for doping concentrations up to the dangling bond spin density. For higher doping concentrations a doping efficiency close to unity is found. It could be shown that in  $\mu$ c-Si:H the measured spin densities represent the majority of gap states ( $N_S = N_{DB}$ ). The close relationship between the CE resonance intensity and the conductivity is confirmed, which means the electrons contributing to the CE signal represent the majority of the charge carriers contributing to electrical transport.

Transient photocurrent measurements were carried out on  $\mu$ c-Si:H material prepared in the highly crystalline regime. It was found that in these materials conventional time-of-flight interpretation is consistent and may be applied to obtain hole drift mobilities. It has been shown that in this material hole transport is dominated by effects associated with multiple trapping in valence band-tail states. Analyzing the transient photocurrents it was found that the density of valence band-tail states falls exponentially towards the gap with a typical band-tail width of  $\Delta E_V \approx 31$  meV.

Combining the information derived in this work a schematic picture of the density of states in both a spatial and energetic sense has been obtained.

## Appendix A

# Algebraic Description of the Multiple Trapping Model

Dispersive transport is a characteristic observed in many disordered semiconductors and can be described by simple models of trap-controlled charge carrier transport (see e.g. [97, 185] for a review). Within this section, the special case of multiple trapping in an exponentially decaying band-tail is described analytically. The calculations are adopted from Schiff [186], while the algebra is based on the "TROK" approximations established by Tiedje, Rose, Orenstein and Kastner [187, 188]. The model assumes that states in the valance band-tail are separated by an mobility edge  $E_V$ , where transport takes place only in the extended states located below  $E_V$ . Charge carriers trapped in states above  $E_V$  are totally immobile. In this section, an approximate expression for the experimentally accessible value of the displacement/electric field ratio L/F is given. For an exponentially decaying distribution of traps the density of states g(E) in the valence band-tail can be written as

$$g(E) = g_0 \cdot \exp\left(-\frac{E}{\Delta E_V}\right),$$
 (A.1)

where  $g_0$  is the density of states at the mobility edge  $E_V$  (note that E is defined as the zero of energy, which increases in the direction of the bandgap) and  $\Delta E_V$  the width of the valance band-tail. One "TROK" approximation assumes that the capture cross section of the localized states is energy independent and states above  $E_V$  will initially be populated uniformly by carriers which are trapped following the excitation. Somewhat later, charge carriers in shallow states will be released thermally, while trapping processes remains random. The demarcation level  $E_D(t)$  can be defined as the energy which separates those states who are so deep that charge carriers trapped in them have not yet been thermally excited even once, from those who are in thermal equilibrium with the conducting states.  $E_d$  can be

written as

$$E_d(t) = E_V + kT \ln(\nu t), \tag{A.2}$$

where kT is the temperature in energy units and  $\nu$  an attempt-to-escape frequency. It has been shown by Tiedje, Rose, Orenstein, and Kastner that at any time prior to the transit time and in the absence of recombination the carrier distribution is determined by the demarcation energy as

$$N = F(t) \int_{-\infty}^{+\infty} \frac{g_0 \cdot \exp\left(-\frac{E}{\Delta E_V}\right)}{1 + \exp\left(\frac{E - E_d}{kT}\right)} dE. \tag{A.3}$$

where F(t) is an occupation factor which acts to conserve the excitation density N. For the occupancy factor F(t) one derives

$$F(t) = \frac{N}{kT_0 g_0} \frac{\sin(\alpha \pi)}{\alpha \pi} (\nu t)^{\alpha}, \tag{A.4}$$

where  $\alpha = kT/\Delta E_V$ , while the time dependent drift mobility can be written as

$$\mu(t) \equiv \mu_0 \frac{n(t)}{N} = \mu_0 \frac{N_V}{kT_0 g_0} \cdot \frac{sin(\alpha \pi)}{\alpha \pi} (vt)^{-1+\alpha}, \tag{A.5}$$

where  $N_V$  is the effective density of states at the mobility edge, n(t) is the density of mobile charge carriers, and  $\mu_0$  is their mobility. Since  $\mu(t)$  is defined as

$$\mu(t) = \frac{\bar{\mathbf{v}}(t)}{F},\tag{A.6}$$

where v(t) is the mean drift-velocity and F is the electric field, one can find the displacement L(t) by integration:

$$\frac{L(t)}{F} = \frac{N_V}{kTg_0} \cdot \frac{\sin(\alpha\pi)}{\alpha\pi} \left(\frac{\mu_0}{\nu}\right) (\nu t)^{\alpha}$$
(A.7)

Using Eq. A.1, the effective DOS in the valence band can be written as

$$N_V = \int_{-\infty}^{0} g(E) \cdot \exp\left(\frac{E}{kT}\right) \tag{A.8}$$

For  $kT < \Delta E_V$  and assuming that the integral is dominated by an exponential region of g(E) below  $E_V$  one obtains for  $N_V$ 

$$N_V = \frac{kTg_0}{1 - \frac{kT}{\Delta E_V}}. (A.9)$$

Eq. A.7 then becomes

$$\frac{L(t)}{F} = \frac{\sin(\alpha \pi)}{\alpha \pi (1 - \alpha)} \left(\frac{\mu_0}{\nu}\right) (\nu t)^{\alpha} \quad \text{with} \quad \alpha = \frac{kT}{\Delta E_V}. \tag{A.10}$$

Using this equation the displacement/field ratio only depends on three parameters, the width of the exponential band-tail  $\Delta E_V$ , the band mobility  $\mu_0$  describing the mobility of charge carriers in extended states and the attempt to escape frequency  $\nu$ , all describing crucial properties of band-tail.

The analysis of the multiple trapping model presented above is based on the (plausible) assumption that a Fermi-Dirac type of distribution applies to the carriers in traps [186, 128, 188]. This "TROK" approximation has been shown by Monte-Carlo calculations to be quite good for exponential band-tails, and can be shown to be exact for the special case  $\alpha = 1/2$  [189]. For non-exponential densities-of-states, the TROK approximation is unreliable.

# Appendix B

# **List of Samples**

**Table B.1:** Parameters of intrinsic  $\mu$ c-Si:H prepared using a HWCVD process. The filament temperature was  $T_F = 1650^{\circ}$ C, while the deposition pressure was p = 3.5 Pa, except for samples 02C261-02C297 with p = 5 Pa.

	Sample	[SiH <sub>4</sub> ]	m [mg]	$\sigma_D$ [S/cm]	$I_C^{RS}$	$N_S$	g-value
185°C	01c297	5.0	34.8	$5.21 \times 10^{-08}$	0.6	$4.70 \times 10^{+15}$	2.0046
	01c298	5.7	35.8	$4.40 \times 10^{-09}$	0.51	$5.10 \times 10^{+15}$	2.0046
	01c299	5.7	37.5	$5.38 \times 10^{-07}$	0.4	$4.30 \times 10^{+15}$	2.0045
	02C261	5.0	54.6		0.63	$1.67 \times 10^{+16}$	2.0047
	02C260	6.3	63.3			$7.57 \times 10^{+15}$	2.0048
	02C287	5.5	31.1		0.58	$7.01 \times 10^{+15}$	2.0043
	02C288	4.7	16.4		0.67	$9.79 \times 10^{+15}$	2.0048
	02C292	6.0	15.7		0	$1.66 \times 10^{+16}$	2.0047
	02C291	7.0	20.7		0.23	$8.29 \times 10^{+15}$	2.0048
	02C297	9.0	13.9		0	$1.03 \times 10^{+16}$	2.0049
250°C	02c128	3.0	34.8		0.74	$8.82 \times 10^{+16}$	2.0047
	02c117	4.0	45.5		0.7	$3.18 \times 10^{+16}$	2.0049
	02c125	5.0	41.3		0.63	$1.98 \times 10^{+16}$	2.0049
	02c113	6.0	41.5		0.59	$7.76 \times 10^{+15}$	2.0046
	02c121	7.0	56.3		0.5	$8.87 \times 10^{+15}$	2.0047
	02c134	9.0	46.3		0	$1.17 \times 10^{+16}$	2.0052

**Table B.2:** Parameters of intrinsic  $\mu$ c-Si:H prepared using a HWCVD process. The filament temperature was  $T_F = 1750$ °C for samples prepared at  $T_S = 450$ °C and  $T_F = 1650$ °C for the other. The pressure was p = 5 Pa.

	Sample	[SiH <sub>4</sub> ]	m [mg]	$\sigma_D$ [S/cm]	$I_C^{RS}$	$N_S$	g-value
285°C	01c050	3.0	23.0	$1.38 \times 10^{-06}$	0.77	2.13×10 <sup>+17</sup>	2.0480
	01c045	5.0	24.0	$2.42 \times 10^{-06}$	0.65	$1.36 \times 10^{+16}$	2.0050
	01c052	6.3	22.1	$1.12 \times 10^{-05}$	0.54	$8.67 \times 10^{+15}$	2.0048
	01c047	7.5	15.3	$1.03 \times 10^{-06}$	0.4	$2.28 \times 10^{+16}$	2.0052
	01c051	8.8	15.0	$6.69 \times 10^{-07}$	0.29	$1.46 \times 10^{+16}$	2.0051
	01c048	10.0	14.1	$1.05 \times 10^{-10}$	0	$4.84 \times 10^{+16}$	2.0050
	01c074	10.0	29.3		0.1	$1.42 \times 10^{+16}$	2.0049
	01c077	11.3	24.8		0	$1.18 \times 10^{+16}$	2.0050
	01c075	12.5	28.9		0	$1.23 \times 10^{+16}$	2.0049
330°C	01c067	5.0	31.6	$2.74 \times 10^{-07}$		$2.60 \times 10^{+17}$	2.0050
	01c073	5.0	35.6	$2.74 \times 10^{-07}$	0.63	$2.84 \times 10^{+17}$	2.0050
	01c064	7.5	25.6	$1.15 \times 10^{-05}$	0.58	$1.29 \times 10^{+17}$	2.0053
	01c066	10.0	28.1	$1.13 \times 10^{-06}$	0.42	$7.70 \times 10^{+16}$	2.0053
	01c072	11.3	27.1	$5.13 \times 10^{-08}$	0.31	$3.08 \times 10^{+16}$	2.0051
	01c068	12.5	29.5	$9.38 \times 10^{-12}$	0.15	$4.37 \times 10^{+16}$	2.0053
	01c065	15.0	17.9	$1.95 \times 10^{-11}$	0	$1.40 \times 10^{+17}$	2.0038
	01c070	19.0	19.5		0	$8.30 \times 10^{+16}$	2.0051
450°C	00C247	5.0		$2.38 \times 10^{-07}$	0.76	$4.80 \times 10^{+18}$	2.0050
	00C235	7.5		$6.94 \times 10^{-07}$	0.66	$1.70 \times 10^{+18}$	2.0048
	00C264	10.0		$5.01 \times 10^{-07}$	0.75	$4.30 \times 10^{+18}$	2.0056
	00C241	12.5		$3.30 \times 10^{-07}$	0.69	$1.00 \times 10^{+18}$	2.0053
	00C258	15.6		$3.05 \times 10^{-07}$	0.74	$8.10 \times 10^{+17}$	2.0050
	00C266	15.6		$2.46 \times 10^{-08}$	0.48	$1.30 \times 10^{+18}$	
	00C242	18.8		$7.64 \times 10^{-08}$	0.58	$5.20 \times 10^{+17}$	2.0050
	00C256	21.9		$1.59 \times 10^{-08}$	0.55	$1.00 \times 10^{+18}$	2.0053
	00C261	25.0		$7.09 \times 10^{-11}$	0.1	$9.00 \times 10^{+16}$	2.0057

**Table B.3:** Parameters of n-type  $\mu$ c-Si:H prepared using VHF-PECVD. The process parameters were  $T_S = 200^{\circ}$ C, the pressure was p = 40 Pa and the plasma power density P = 0.07 W/cm<sup>2</sup>.

Sample	[SiH <sub>4</sub> ]	m [mg]	$\sigma_D$ [S/cm]	$I_C^{RS}$ (glass)	$I_C^{RS}$ (Al)	$N_S$
1 ppm						
$\overline{01B467}$	2.0	72.2	$3.11 \times 10^{-05}$	0.81	0.82	$2.36 \times 10^{+16}$
01B363	4.0	69.3	$6.78 \times 10^{-04}$	0.71	0.77	$4.12 \times 10^{+16}$
01B357	5.0	78.5	$6.04 \times 10^{-04}$	0.66	0.7	$5.17 \times 10^{+16}$
01B399	6.0	91.9	$1.66 \times 10^{-04}$	0.33	0.45	$4.24 \times 10^{+16}$
01B361	7.0	67.2	$1.49 \times 10^{-10}$	0	0.03	$6.87 \times 10^{+15}$
01B466	8.0	91.1	$3.76 \times 10^{-10}$	0	0	$4.44 \times 10^{+15}$
5 ppm						
$\overline{01B390}$	2.0	42.0	$2.11\times10^{-04}$	0.83	0.84	$4.71 \times 10^{+16}$
01B364	4.0	44.0	$6.19 \times 10^{-03}$	0.78	0.78	$1.69 \times 10^{+17}$
01B385	6.0	83.4	$4.24 \times 10^{-04}$	0.12	0.4	$1.38 \times 10^{+17}$
01B391	7.0	81.2	$2.94 \times 10^{-08}$	0	0.05	$2.56 \times 10^{+17}$
01B468	8.0	93.3	$1.90 \times 10^{-08}$	0	0	$7.74 \times 10^{+15}$
10 ppm						
01B415	2.0	79.0	$2.87 \times 10^{-03}$	0.82	0.83	$1.20 \times 10^{+17}$
01B402	4.0	60.0	$2.06 \times 10^{-02}$	0.74	0.76	$2.52 \times 10^{+17}$
01B410	6.0	83.0	$1.12 \times 10^{-02}$	0.38	0.51	$2.72 \times 10^{+17}$
01B413	7.0	109.0	$1.45 \times 10^{-06}$	0	0.08	$1.33 \times 10^{+17}$
01B472	8.0	87.7	$1.72 \times 10^{-07}$	0	0	$8.71 \times 10^{+15}$

**Table B.4:** Parameters of intrinsic  $\mu$ c-Si:H prepared using a PECVD process. The process parameters were  $T_S = 200$ °C, the pressure was p = 300 mTorr, and the was plasma power density P = 0.07 W/cm<sup>2</sup>.

	Sample	[SiH <sub>4</sub> ]	m [mg]	$\sigma_D$ [S/cm]	$I_C^{RS}$	$N_S$	g-value
							ŭ
<u>VHF</u>	00B501	2.0	75.0	$5.09 \times 10^{-06}$	0.78	$7.20 \times 10^{+16}$	2.0046
	00B493	3.0	70.0	$3.47 \times 10^{-06}$	0.68	$2.50 \times 10^{+16}$	2.0044
	00B489	4.0	80.0	$1.34 \times 10^{-06}$	0.61	$2.15 \times 10^{+16}$	2.0044
	00B483	5.0	58.0	$2.40 \times 10^{-06}$	0.53	$2.00 \times 10^{+16}$	2.0044
	00B487	6.0	80.0	$6.81 \times 10^{-08}$	0.43	$1.30 \times 10^{+16}$	2.0046
	01B098	6.0	104.0		0.39	$8.50 \times 10^{+15}$	2.0046
	01B103	7.0	88.0		0.16	$2.80 \times 10^{+15}$	2.0047
	00B497	7.0	91.0	$1.50 \times 10^{-10}$	0	$2.66 \times 10^{+15}$	2.0047
	00B509	8.0	81.0	$2.45 \times 10^{-11}$	0	$3.20 \times 10^{+15}$	2.0048
	01B096	9.0	123.7		0	$3.60 \times 10^{+15}$	2.0050
	00B512	9.0	93.0	$2.00 \times 10^{-11}$	0	$2.00 \times 10^{+15}$	2.0047
	03B274	20.0	67.4		0	$3.80 \times 10^{+15}$	2.0053
	03B275	30.0	92.9		0	$5.00 \times 10^{+15}$	2.0054
	01B163	50.0	158.0		0	$7.00 \times 10^{+15}$	2.0054
	03B277	100.0	65.5		0	$9.50 \times 10^{+15}$	2.0054

# **Appendix C**

# **Abbreviations, Physical Constants** and **Symbols**

#### **Abbreviations**

a-S1:H	Hydrogenated amorphous silicon
c-Si	Crystalline silicon

c-Si Crystalline silicon
CE Conduction electron

D<sup>+</sup> Positively charged dangling bond defect

D<sup>0</sup> Neutral dangling bond defect

D Negatively charged dangling bond defect

 $\begin{array}{lll} DB & Dangling \ Bond \\ db_1 & ESR \ line \ at \ g=2.0043 \\ db_2 & ESR \ line \ at \ g=2.0052 \\ DOS & Density \ of \ states \\ ESR & Electron \ spin \ resonance \end{array}$ 

HWCVD Hot-wire chemical vapor deposition

IR Infrared spectroscopy

 $\mu$ c-Si:H Hydrogenated microcrystalline silicon

MT Multiple trapping

PECVD Plasma enhanced chemical vapor deposition

SWE Staebler-Wronski-Effect
TCO Transparent conductive oxide
TEM Transmission electron microscopy

TOF Time-of-flight XRD X-ray diffraction

## Symbols

α	Dispersion parameter
A	Contact area
h	Electrode spacing
$B_0$	Flux density
C	Capacitance
D	Diffusion constant
d	Thickness
$d_i$	
	Thickness of the i-layer
$d_w \ \Delta E_C$	Depletion layer width Conduction band-tail width
	Valence band-tail width
$\Delta E_V$	
$\Delta g$	g-tensor
$\Delta H_{pp}$	Peak to Peak line width
$\eta$	Energy conversion efficiency
E	Band gap
$E_A$	Activation energy
$E_B$	Barrier hight
$E_0$	Energy of the groundstate
$E_C$	Conduction band mobility edge
$E_F$	Fermi level
$E_G$	Energy band gap
$E_{Tr}$	Energy of the transport path
$E_V$	Valence band mobility edge
$oldsymbol{arepsilon}$	Relative dielectic constant
F	Electric Field
g	Electronic g-value
$g_0$	Electronic g-value of the free electron
g(E)	Density of states
L	Orbital angular moment
Ι	Current
$\eta$	Solar cell efficiency
$\mathcal{H}_{pg}$	Hamilton operator
$I_C^{RS}$	Raman intensity ratio
$J_{SC}$	Short circuit current density
l	width of electrode
L	Displacement
$L_D$	Debye screening length
λ	excitation wavelength
$\mu_0$	Band mobility

 $\mu_d$  Drift mobility

 $\mu_{d,h}$  Hole drift mobility

 $\mu \tau_{h,t}$  Deep trapping mobility-lifetime product

 $N_{CE}$  Spin density of CE resonance

 $N_D$  Number of active donors

 $N_{DB}$  Spin density of DB resonance  $(N_{db_1}+N_{db_2})$ 

 $N_{db_1}$  Spin density of db<sub>1</sub> resonance  $N_{db_2}$  Spin density of db<sub>2</sub> resonance  $N_P$  Phosphorous doping concentration

 $N_T$  Concentration trapped charge carrier

 $N_S$  Spin density

v "Attempt-to-escape" frequency

p Pressure

PC Phosphorous doping concentration

 $egin{array}{ll} q & ext{Charge density} \\ Q_0 & ext{Photoinjected charge} \\ Q(t) & ext{Transient photocharge} \\ Q(\infty) & ext{Collected Photocharge} \\ \end{array}$ 

r, R Separation

 $ar{R}$  Mean intersite distance  $R_0$  Localization Radius  $\sigma$  Conductivity  $\sigma_D$  Dark conductivity  $\sigma_D$  Spin operator  $\sigma_D$  Temperature

 $T_S$  Substrate temperature

t Time

t<sub>ann</sub> annealing period

 $T_1$  Spin-lattice relaxation time  $T_2$  Spin-spin relaxation time

 $t_{\tau}$  Transit time

 $T_S$  Substrate temperature

au Lifetime

 $au_D$  Deep trapping life time  $au_{rel}$  Dielectric relaxation time  $au_{corr}$  Correlation energy  $au_{relax}$  Relaxation energy

 $U_{eff}$  Effective correlation energy

V Applied voltage

#### Chapter C: Abbreviations, Physical Constants and Symbols

 $\begin{array}{ll} V_{int} & \text{Internal voltage} \\ v_d & \text{Drift velocity} \\ \omega & \text{Lamor frequency} \\ w & \text{Dispersion} \end{array}$ 

#### **Physical Constants**

e	$1.602 \times 10^{-19}$	C	Elementary charge
$\varepsilon_0$	$8.8542 \times 10^{-12}$	A s $V^{-1} m^{-1}$	Dielectric constant
k	$1.38066 \times 10^{-23}$	$\mathrm{J}~\mathrm{K}^{-1}$	Boltzmann's constant
$\mu_B$	$9.274 \times 10^{-24}$	$ m J~T^{-1}$	Bohr Magneton

## **Bibliography**

- E. Becquerel. Mémoire sur les effets électriques produits sous l'influence des rayons solaires. Comptes Rendus de l'Academie de Science, 9:561, 1839.
- [2] D. M. Chapin, C. S. Fuller, and G. L. Pearson. A new silicon p-n junction photocell for converting solar radiation into electrical power. *Journal of Applied Physics*, 25:645, 1954.
- [3] M.A. Green, K. Emery, D.L. King, S. Igari, and W. Warta. Solar cell efficiency tables (version 19). *Prog. Photovolt.*, *Res. Appl*, 10(1):55–61, 2002.
- [4] B. Rech and H. Wagner. Potential of amorphous silicon for solar cells. *Appl. Phys. A*, A69(2):155–167, 1999.
- [5] W. Hoffmann. Pv solar electricity: One among the new millennium industries. *Proceedings of the 17<sup>th</sup> EPVSEC, Munich*,, 395:851, 2001.
- [6] A. Kreutzmann. Photon, 2:55, 2002.
- [7] D.L. Staebler and C.R. Wronski. Reversible conductivity charge in discharge-produced amorphous si. *Appl. Phys. Lett.*, 31(4):292, 1977.
- [8] S. Vepřek and V. Mareček. The preparation of thin layers of ge and si by chemical hydrogen plasma transport. *Solid-State Electronics*, 11:683, 1968.
- [9] S. Usui and M. Kikuchi. Properties of heavily doped gd-si with low resistivity. *J. Non-Cryst. Solids*, 34(1):1–11, 1979.
- [10] L. Houben, M. Luysberg, P. Hapke, R. Carius, F. Finger, and H. Wagner. Structural properties of microcrystalline silicon in the transition from highly crystalline to amorphous growth. *Phil. Mag. A*, 77:1447, 1998.

- [11] M. Tzolov, F. Finger, R. Carius, and P. Hapke. Optical and transport studies on thin microcrystalline silicon films prepared by very high frequency glow discharge for solar cell applications. *J. Appl. Phys.*, 81:7376, 1997.
- [12] O. Vetterl. On the Physics of Microcrystalline Silicon Thin Film Solar Cells. PhD thesis, Heinrich-Heine Universität Düsseldorf, 2001.
- [13] S. Klein. *Microcrystalline Silicon Prepared by Hot Wire CVD: Preparation and Characterisation of Material and Solar Cells*. PhD thesis, Technische Universität München, 2003.
- [14] M. M. Goerlitzer, N. Beck, P. Torres, U. Kroll, H. Keppner, J. Meier, J. Koehler, N. Wyrsch, and A. Shah. Electronic transport and structure of microcrystalline silicon deposited by the vhf-gd technique. *Mater. Res. Soc. Proc.*, 467:301, 1997.
- [15] N. Wyrsch, C. Droz, L. Feitknecht, M. Goerlitzer, U. Kroll, J. Meier, P. Torres, E. Vallat-Sauvain, A. Shah, and M. Vanecek. Hydrogenated microcrystalline silicon: from material to solar cells. *Mater. Res. Soc. Proc.*, 609:A15.1.1, 2000.
- [16] O. Vetterl, A. Gross, T. Jana, S. Ray, A. Lambertz, and F. Carius, R. Finger. Changes in electric and optical properties of intrinsic microcrystalline silicon upon variation of the structural composition. *Journal of Non-Crystalline Solids*, 299-302:772, 2002.
- [17] A.L. Baia Neto, A. Lambertz, R. Carius, and F. Finger. Spin density and conductivity in thin silicon films upon transition from microcrystalline to amorphous growth. *Phys. Stat. Sol. A*, 186(1):R4, 2001.
- [18] A.L. Baia Neto, A. Lambertz, R. Carius, and F. Finger. Relationships between structure, spin density and electronic transport in 'solar-grade' microcrystalline silicon films. J. Non-Cryst. Solids, 299-302(A):274, 2002.
- [19] J. Meier, R. Flückiger, H. Keppner, and A. Shah. Complete microcrystalline p-i-n solar cell-crystalline or amorphous cell behavior? *Appl. Phys. Lett.*, 65(7):860, 1994.
- [20] S. Veprek, Z. Iqbal, R.O. Kuhne, P. Capezzuto, F.-A. Sarott, and J.K. Gimzewski. Properties of microcrystalline silicon. iv. electrical conductivity, electron spin resonance and the effect of gas adsorption. *Journal of Physics C*, 16(32):6241, 1983.

- [21] D. Will, C. Lerner, W. Fuhs, and K. Lips. Transport and recombination channels in undoped microcrystalline silicon studied by esr and edmr. *Mater. Res. Soc. Proc.*, 467:361, 1997.
- [22] A. Mück, U. Zastrow, O. Vetterl, and B. Rech. *SIMS Depth Profile Analysis of Oxygen Contermination in Hydrogenated Amorphous and Microcrystalline Silicon*, page 689. Elsevier Science B.V., Amsterdam, 2000.
- [23] R. Brüggemann, A. Hierzenberger, H.N. Wanka, and M.B. Schubert. Electronic properties of hot-wire deposited nanocrystalline silicon. *Mater. Res. Soc.*, 507:921, 1998.
- [24] M. Stutzmann and D. Biegelsen. The microscopic structure of defects in a-si:h and related materials. In *Amoprhous Silicon and Related Materials*, pages 557–594. World Scientific, Singapore, 1988.
- [25] M. Stutzmann. On the structure of dangling bond defects in silicon. *Z. Phys. Chem. Neue Folge*, 151(1-2):211, 1987.
- [26] S. Yamasaki, Jung-Kyu Lee, T. Umeda, J. Isoya, and K. Tanaka. Spatial distribution of phosphorus atoms surrounding spin centers of p-doped hydrogenated amorphous silicon elucidated by pulsed esr. *J. Non-Cryst. Solids*, 198-200(1):330–333, 1996.
- [27] S. Hasegawa, S. Narikawa, and Y. Kurata. Esr and electrical properties of p-doped microcrystalline si. *Philos. Mag. B*, 48(5):431–447, 1983.
- [28] S. Hasegawa, S. Narikawa, and Y. Kurata. Dependences of esr and electrical properties on p doping ratio for microcrystalline si. *Physica B & C*, 117-118B+C(2):914–916, 1983.
- [29] F. Finger, C. Malten, P. Hapke, R. Carius, R. Fluckiger, and H. Wagner. Free electrons and defects in microcrystalline silicon studied by electron spin resonance. *Philos. Mag. Lett*, 70(4):247–254, 1994.
- [30] J. Müller. Electron Spin Resonance Studies on Microcrystalline Semiconductors. Berichte des Forschungszentrum Jülichs 3615, ISSN 0944-2952, 1998.
- [31] M. Kondo, S. Yamasaki, and A. Matsuda. Microscopic structure of defects in microcrystalline silicon. *J. Non-Cryst. Solid*, 266-269:544, 2000.
- [32] K. Lips, P. Kanschat, and W. Fuhs. Defects and recombination in microcrystalline silicon. *Solar Energy Materials and Solar Cells*, 78:513, 2003.

- [33] F. Finger, J. Müller, C. Malten, and H. Wagner. Electronic states in hydrogenated microcrystalline silicon. *Philos. Mag. B*, 77:805, 1998.
- [34] P. Kanschat, K. Lips, R. Brüggemann, A. Hierzenberger, I. Sieber, and W. Fuhs. Paramagnetic defects in undoped microcrystalline silicon deposited by the hot-wire technique. *Mater. Res. Soc.*, 507:793, 1998.
- [35] J. Müller, F. Finger, R. Carius, and H. Wagner. Electron spin resonance investigation of electronic states in hydrogenated microcrystalline silicon. *Phys. Rev. B*, 60:11666, 1999.
- [36] P. Kanschat, H. Mell, K. Lips, and W. Fuhs. Defect and tail states in microcrystalline silicon investigated by pulsed esr. *Mater. Res. Soc. Proc.*, 609:A27.3, 2000.
- [37] M. Kondo, T. Ohe, K. Saito, T. Nishimiya, and A. Matsuda. Morphological study of kinetic roughening on amorphous and microcrystalline silicon surface. *J. Non-Cryst. Solids*, 227-230(B):890–895, 1998.
- [38] P. Kanschat, K. Lips, and W. Fuhs. Identification of non-radiative recombination paths in microcrystalline silicon (μc-si:h). *J. Non-Cryst. Solids*, 266-269:524–528, 2000.
- [39] F. Finger, J. Müller, C. Malten, R. Carius, and H. Wagner. Electronic properties of microcrystalline silicon investigated by electron spin resonance and transport measurements. *Journal of Non-Crystalline Solids*, 226-269:511, 2000.
- [40] P. Kanschat. *ESR und spinabhängige Rekombination in mikrokristallinem Silizium*. PhD thesis, Philipps-Universität Marburg, 2000.
- [41] J.W. Seto. The electrical properties of polycrystalline silicon films. *Journal of Applied Physics*, 46:5247, 1975.
- [42] T. Weis, R. Lipperheide, U. Wille, and S. Brehme. Barrier-controlled carrier transport in microcrystalline semiconducting materials: Description within a unified model. *J. Appl. Phys.*, 92(3):1411, 2002.
- [43] S. Brehme, P. Kanschat, T. Weis, K. Lips, and W. Fuhs. Barrier-controlled transport in highly doped microcrystalline silicon: role of interface states. *Diffus. Defect Data B, Solid State Phenom.*, 80-81:225, 2001.
- [44] R. Carius, F. Finger, U. Backhausen, M. Luysberg, P. Hapke, L. Houben, M. Otte, and H. Overhof. Electronic properties of microcrystalline silicon. *Mater. Res. Soc. Proc.*, 467:283, 1997.

- [45] H. Overhof and M. Otto. Theoretical investigations of models for the electronic transport in microcrystalline silicon films. In J.M. Marshall, N. Kirov, A. Vavrek, and J.M. Maud, editors, *Thin Film Materials and De*vices - Developments in Science and Technology, page 23. World Scientific, Singapore, 1997.
- [46] R. Carius, J. Müller, F. Finger, N. Harder, and P. Hapke. Photo- and dark conductivity of μc-si:h thin films. In J.M. Marshall, N. Kirov, A. Vavrek, and J.M. Maud, editors, *Thin Film Materials and Devices - Developments* in Science and Technology, page 157. World Scientific, Singapore, 1999.
- [47] W. Fuhs, P. Kanschat, and K. Lips. Bandtails and defects in microcrystalline silicon (μc-si:h). *Journal of Vacuum Science & Technology B*, 18(3):1792–1795, 2000.
- [48] N. Harder. Elektrischer transport in dotierten und undotierten mikrokristallinen siliziumschichten. Master's thesis, Universität Leipzig, 1998.
- [49] M. Serin, N. Harder, and R. Carius. Investigation of the transport properties of microcrystalline silicon by time-of-flight (tof). *Journal of Material Science: Material in Electronics*, 14(10-12):733, 2003.
- [50] M. Luysberg, P. Hapke, R. Carius, and F. Finger. Structure and growth of hydrogenated microcrystalline silicon: investigation by transmission electron microscopy and raman spectroscopy of films grown at different plasma excitation frequencies. *Phil. Mag. A*, 75:31, 1997.
- [51] F. Finger, R. Carius, P. Hapke, L. Houben, M. Luysberg, and M. Tzolov. Growth and structure of microcrystalline silicon prepared with glow discharge at various plasma excitation frequencies. *Mat. Res. Soc. Symp. Proc.*, 452:725, 1997.
- [52] L. Houben. Plasmaabscheidung von mikrocrystallinem Silizium: Merkmale der Mikrostruktur und deren Deutung im Sinne von Wachstumsvorgängen. PhD thesis, Heinrich-Heine-Universität Düsseldorf, 1998.
- [53] T. Roschek. *Microcrystalline Silicon Solar Cells prepared by 13.56 MHz PECVD*. PhD thesis, Heinrich-Heine-Universität Düsseldorf, 2003.
- [54] R.W. Collins and B.Y. Yang. In situ ellipsometry of thin-film deposition: Implications for amorphous and microcrystalline si growth. *J. Vac. Sci. Technol. B*, 7(5):1155, 1989.

- [55] C.C. Tsai, G.B. Anderson, and R. Thompson. Low temperature growth of epitaxial and amorphous silicon in a hydrogen-diluted silane plasma. *J. Non-Cryst. Solids*, 137-138(2):673, 1991.
- [56] E. Vallat-Sauvain, U. Kroll, J. Meier, N. Wyrsch, and A. Shah. Microstructure and surface roughness of microcrystalline silicon prepared by very high frequency-glow discharge using hydrogen dilution. *Journal of Non-Crystalline Solids*, 266-269:125, 2000.
- [57] I. Sieber, N. Wanderka, Kaiser, I., and Fuhs. Electron microscopic characterization of microcrystalline silicon thin films deposited by ecr-cvd. *Thin Solid Films*, 403-404:543, 2002.
- [58] L. Houben, M. Luysberg, and R. Carius. Microtwinning in microcrystalline silicon and its effects on grain size measurements. *Physical Review B*, 67:045312, 2003.
- [59] W. Beyer and A. Ghazala. Absorption strengths of si-h vibrational modes in hydrogenated silicon. *Mat. Res. Soc. Symp. Proc.*, 507:601, 1998.
- [60] W. Beyer. private communication, 2002.
- [61] P.M. Voyles, M.M.J. Treacy, H.C. Jin, J.R. Abelson, J.M. Gibson, J. Yang, S. Guha, and R.S. Crandall. Comparative fluctuation microscopy study of medium-range order in hydrogenated amorphous silicon deposited by various methods. *Mater. Res. Soc. Proc.*, 664:A2.4.1, 2001.
- [62] C. Longeaud, J.P. Kleider, P. Roca i Cabarrocas, S. Hamma, R. Meaudre, and M. Meaudre. Properties of a new a-si:h-like material: hydrogenated polymorphous silicon. *Journal of Non-Crystalline Solids*, 227-230(A):96, 1998.
- [63] R. Koval, Xinwei Niu, J. Pearce, Lihong Jiao, G. Ganguly, J. Yang, S. Guha, R.W. Collins, and C.R. Wronski. Kinetics of light induced changes in protocrystalline thin film materials and solar cells. *Mater. Res. Soc. Proc.*, 609:A15.5.1, 2001.
- [64] H. Stiebig. Entwicklung und Beschreibung von optoelektronischen Bauelementen auf der Basis von amorphen Silizium. Berichte des Forschungszentrum Jülichs 3464, ISSN 0944-2952, 1997.
- [65] R.A. Street. *Hydrogenated Amorphous Silicon*. Cambridge University Press, Cambridge, 1991.

#### **BIBLIOGRAPHY**

- [66] P.W. Anderson. Absence of diffusion in certain random lattices. *Phys. Rev.*, 109:1492, 1958.
- [67] N.F. Mott. Electrons in disordered structures. Adv. Phys., 16(61):49, 1967.
- [68] N.F. Mott and E.A. Davis. *Electronic Processes in Non-crystalline Materials*. Oxford University Press, Oxford, 2nd edition, 1979.
- [69] J. Werner and M. Peisl. Exponential band tails in polycrystalline semiconductor films. *Phys. Rev. B*, 31(10):6881, 1985.
- [70] J. Werner and M. Peisl. Exponential band tails at silicon grain boundaries. *Mater. Res. Soc*, 46:575, 1985.
- [71] J. Werner. *Band tailing in polycrystalline and disordered silicon*, volume 35 of *Proceedings of Physics*, pages 345–351. Springer, Berlin, 1989.
- [72] K. Lips, P. Kanschat, S. Brehme, and W. Fuhs. Band tail states and free electrons in phosphorus doped microcrystalline silicon studied by esr. *Thin Solid Films*, 403-404:47, 2002.
- [73] S. Reynolds, V. Smirnov, C. Main, R. Carius, and F. Finger. Localised states in microcrystalline silicon photovoltaic structures studied by posttransit time-of-flight spectroscopy. *Mater. Res. Soc. Proc.*, 762:327, 2003.
- [74] R. Carius, T. Merdzhanova, and F. Finger. Electronic properties of microcrystalline silicon investigated by photoluminescence spectroscopy on films and devices. *Mater. Res. Soc. Proc.*, 762:321, 2003.
- [75] T.R. Merdzhanova. *Microcrystalline Silicon Films and Solar Cells Investigated vy Photoluminescence Spectroscopy*. PhD thesis, Bulgarian Academy of Science, Sofia, 2004.
- [76] T. Tiedje. Information about band tail states from time-of-flight experiments. Semiconductors and Semimetals, 21(Part C):207, 1984.
- [77] T. Dylla, E.A. Schiff, and F. Finger. Hole drift-mobility measurements and multiple-trapping in microcrystalline silicon. *Mater. Res. Soc. Proc.*, 2004 in press.
- [78] B.I. Halperin and M. Lax. Impurity-band tails in the high-density limit. i. minimum counting methods. *Phys. Rev.*, 148:722, 1966.
- [79] C.M. Soukoulis, M.H. Cohen, and E.N. Economou. Exponential band tails in random systems. *Phys. Rev. Lett.*, 53:616, 1984.

- [80] C.M. Soukoulis, M.H. Cohen, E.N. Economou, and A.D. Zdetsis. Electronic structure at band edges. *Journal of Non-Crystalline Solids*, 77-78:47, 1985.
- [81] E.N. Economou and N. Bacalis. Exponential tails in the density of states. *Journal of Non-Crystalline Solids*, 97-98:101, 1987.
- [82] E.N. Economou, C.M. Soukoulis, M.H. Cohen, and S. John. page 681. Plenum Press, New York, 1987.
- [83] R.A. Street and N.F. Mott. States in the gap in glassy semiconductors. *Phys. Rev. Lett.*, 35(19):1293, 1975.
- [84] M.M. de Lima, P.C. Taylor, S. Morrison, A. LeGeune, and F.C. Marques. Esr observations of paramagnetic centers in intrinsic hydrogenated microcrystalline silicon. *Phys. Rev. B*, 65(23):235324/1, 2002.
- [85] M. Stutzmann, M.S. Brandt, and M.W. Bayerl. Spin-dependent processes in amorphous and microcrystalline silicon: a survey. *J. Non-Cryst. Solids*, 266-269:1, 2000.
- [86] M. Stutzmann. Weak bond-dangling bond conversion in amorphous silicon. *Philos. Mag. B*, 56(1):63, 1987.
- [87] S. Klein, F. Finger, R. Carius, T. Dylla, B. Rech, M. Grimm, L. Houben, and M. Stutzmann. Intrinsic microcrystalline silicon prepared by hot-wire chemical vapour deposition for thin film solar cells. *Thin Solid Films*, 430(1-2):202, 2003.
- [88] M. Kondo, T. Nishimiya, K. Saito, and A. Matsuda. Light induced phenomena in microcrystalline silicon. *J. Non-Cryst. Solids*, 227-230(B):1031, 1998.
- [89] R.A. Street and D.K. Biegelsen. Distribution of recombination lifetimes in amorphous silicon. *Solid State Communications*, 44(4):501, 1982.
- [90] W.B. Jackson and N.M. Amer. Direct measurement of gap-state absorption in hydrogenated amorphous silicon by photothermal deflection spectroscopy. *Physical Review B*, 25(8):5559, 1982.
- [91] S.M. Sze. *Physics of Semiconductor Devices*. John Wiley & Sons, New York, 2nd edition, 1981.
- [92] G. Baccarani, B. Riccó, and G. Spadini. Transport properties of polycrystalline silicon films. *Journal of Applied Physics*, 49(11):5565, 1978.

#### **BIBLIOGRAPHY**

- [93] J.W. Orton and M.J. Powell. The hall effect in polycrystalline and powdered semiconductors. *Rep. Prog. Phys.*, 43(11):1263, 1980.
- [94] W.E. Spear, A.C. Hourd, and D.L. Melville. Electronic properties of amorphous and microcrystalline silicon prepared in a microwave plasma from sif<sub>4</sub>. *Phil. Mag. B*, 64(5):533, 1991.
- [95] G. Willeke. *Physics and Electronic Properties of Microcrystalline Semi-conductors*. Artech House, London, 1992.
- [96] D. Ruff. Elektrischer Transport in mikrokristallinem Silizium. PhD thesis, Philipps-Universität Marburg, 1999.
- [97] T. Tiedje. *Physics of hydrogenated amorphous silicon II. Electronic and vibrational properties*, chapter Time-resolved charged transport in hydrogenated amorphous silicon, pages 261–300. Springer-Verlag, 1984.
- [98] F.W. Schmidlin. Theory of trap-controlled transient photoconduction. *Phys. Rev. B*, 16(6):2362, 1977.
- [99] H. Scher and E.W. Montroll. Anomalous transit-time dispersion in amorphous solids. *Physical Review B*, 12(6):2455, 1975.
- [100] J.M. Marshall. A trap-limited model for dispersive transport in semiconductors. *Philos. Mag.*, 36(4):959, 1977.
- [101] M. Silver and L. Cohen. Monte carlo simulation of anomalous transit-time dispersion of amorphous solids. *Phys. Rev. B*, 15(6):3276, 1977.
- [102] J. Noolandi. Multiple-trapping model of anomalous transit-time dispersion in alpha-se. *Phys. Rev. B*, 16(10):4466, 1977.
- [103] J. Noolandi. Equivalence of multiple-trapping model and time-dependent random walk. *Phys. Rev. B*, 16(10):4474, 1977.
- [104] C.H. Henry and D.V. Lang. Nonradiative capture and recombination by multiphonon emission in gaas and gap. *Phys. Rev. B*, 15(2):989, 1977.
- [105] D.A. Long. *Raman Spectroscopy*. McGraw-Hill International Book Company, 1977.
- [106] M. Cardona. Light Scattering in Solids. Springer, Berlin, 1982.
- [107] H. Richter. Elektronen und Phononen in mikrokristallinem Silizium. PhD thesis, Universität Stuttgart, 1983.

- [108] P. Hapke. VHF-Plasmaabscheidung von mikrokristalinem Silizium (µc-Si): Einfluss der Plasmaanregungsfrequenz auf die strukturellen und elektrischen Eigenschaften. PhD thesis, Rheinisch-Westfälische Technische Hochschule Aachen, 1995.
- [109] L. Houben. Strukturelle Eigenschaften von mikrokristallinen Silizium im Übergangsbereich zwischen mikrokristallinem und amorphem Wachstum. Diploma thesis, Heinrich-Heine-Universität Düsseldorf, 1995.
- [110] H. Richter, Z.P. Wang, and L. Ley. The one phonon raman spectrum in microcrystalline silicon. *Solid State Communications*, 39:625, 1981.
- [111] R. Kobliska and S. Solin. Raman spectrum of wurzit silicon. *Physical Review B*, 8(8):3799, 1973.
- [112] R. Tsu, J. Gonzalez-Hernandez, S. Chao, S. Lee, and K. Tanaka. Critical volume fraction of crystallinity for conductivity percolation in phosphorus-doped si:f:h alloys. *Applied Physics Letters*, 40(534), 1982.
- [113] S. Vepřek, F. Sarrot, and Z. Iqbal. Effect of grain boundaries on the raman spectra, opical absorption and the elastic scattering in nanometersized crystalline silicon. *Physical Review B*, 36(6):3344, 1987.
- [114] C. Ossadnik, S. Veprek, and I. Gregora. Applicability of raman scattering for the characterization of nanocrystalline silicon. *Thin Solid Films*, 337:148, 1999.
- [115] L. Houben. Morphological and crystallographic defect properties of microcrystalline silicon: a comparison between different growth modes. *Journal of Non-Crystalline Solids*, 227-230:896, 1998.
- [116] R. Carius and S. Klein. unpublished results.
- [117] E. Zavoisky. Spin-magnetic resonance in paramagnetics. *J. Phys. USSR*, 9:211, 1945.
- [118] P.W. Atherton. *Principles of electron spin resonance*. Ellis Horword, PTR Prentice Hall, Chichester, 1993.
- [119] C.P. Poole. Electron Spin Resonance. Wiley-Intersience, New York, 1982.
- [120] J. Malten. Pulsed Electron Spin Resonance of Amorphous and Microcrystalline Semiconductors. Berichte des Forschungszentrum Jülichs 3273, ISSN 0944-2952, 1996.

#### **BIBLIOGRAPHY**

- [121] J.R. Haynes and W. Shockley. The mobility and life of injected holes and electrons in germanium. *Physical Review*, 81(5):835, 1951.
- [122] R. Lawrance and A.F. Gibson. The measurement of drift mobility in semi-conductors. *Proc. Phys. Soc*, 65B:994, 1952.
- [123] W.E. Spear. Transit time measurements of charge carriers in amorphous selenium films. *Proc. Phys. Soc.*, 77:1157, 1957.
- [124] W.E. Spear. The hole mobility in selenium. Proc. Phys. Soc., 76:826, 1960.
- [125] W.E. Spear. Drift mobility techniques for the study of electrical transport properties in insulating solids. *Journal of Non-crystalline Solids*, 1(3):197, 1969.
- [126] W.E. Spear and H.L. Steemers. The interpretation of drift mobility experiments on amorphous silicon. *Philosophical Magazine B*, 47(5):L77, 1983.
- [127] M.A. Lampert and P. Mark. Current Injection in Solids. Academic Press, New York, 1970.
- [128] T. Tiedje, T.D. Moustakas, and J.M. Cebulka. Temperature dependence of the electron drift mobility in hydrogenated a-si prepared by sputtering. *Journal de Physique Colloque*, 42(C-4):155, 1981.
- [129] T. Tiedje, C.R. Wronski, B. Abeles, and J.M. Cebulka. Electron transport in hydrogenated amorphous silicon: drift mobility and junction capacitance. *Solar Cells*, 2(3):301, 1980.
- [130] W.E. Spear and H.L. Steemers. The reversal of drifting excess carriers in an amorphous silicon junction. *Philosophical Magazine B*, 47(6):L107, 1983.
- [131] Q. Wang, H. Antoniadis, E.A. Schiff, and S. Guha. Electron drift mobility measurements and conduction bandtails in hydrogenated amorphous silicon-germanium alloys. *Physical Review B*, 47(15):9435, 1993.
- [132] M.E. Scharfe. Transient photoconductivity in vitreous as<sub>2</sub>se<sub>3</sub>. *Physical Review B*, 2(12):5025, 1970.
- [133] D.M. Pai and M.E. Scharfe. Charge transport in films of amorphous arsenic triselenide. (dc dark current and transient photoconductivity studies). *Journal of Non-Crystalline Solids*, 8-10:752, 1972.
- [134] J.M. Marshall, R.A. Street, and M.J. Thompson. Electron drift mobility in amorphous si:h. *Philos. Mag. B*, 54(1):51, 1986.

- [135] C.E. Nebel, H.C. Weller, and G.H Bauer. Extended state mobility and tail state distribution of a-si<sub>1-x</sub>ge<sub>x</sub>:h alloys. *Mater. Res. Soc. Proc.*, 118:507, 1988.
- [136] C.E. Nebel. *Ladungsträgertransport und Rekombination in a-SiGe:H.* PhD thesis, Universität Stuttgart, 1990.
- [137] N. Kopidakis, E.A. Schiff, N.-G. Park, J. Van De Lagemaat, and A.J. Frank. Ambipolar diffusion of photocarriers in electrolyte-filled, nanoporous tio<sub>2</sub>. *J. Phys. Chem. B*, 104(16):3930, 2000.
- [138] P.N. Rao, E.A. Schiff, L. Tsybeskov, and P. Fauchet. Photocarrier drift-mobility measurements and electron localization in nanoporous silicon. *Chemical Physics*, 284(1-2):129, 2002.
- [139] D. Han, D.C. Melcher, E.A. Schiff, and M. Silver. Optical-bias effects in electron-drift measurements and defect relaxation in a-si:h. *Physical Review B*, 48(12):8658, 1993.
- [140] Q. Gu, Q. Wang, E.A. Schiff, Y.M. Li, and C.T. Malone. Hole drift mobility measurements in amorphous silicon carbon alloys. *J. Appl. Phys.*, 76(4):2310, 1994.
- [141] P. Rao, E.A. Schiff, L. Tsybeskov, and P.M. Fauchet. Electron time-of-flight measurements in porous silicon. *Mater. Res. Soc. Proc.*, 452:613, 1997.
- [142] S. Dinca, G. Ganguly, Z. Lu, E.A. Schiff, V. V. Vlahos, C.R. Wronski, and Q. Yuan. Hole drift-mobility measurements in contemporary amorphous silicon. *Mater. Res. Soc. Proc.*, 762:345, 2003.
- [143] N. Wyrsch, M. Goerlitzer, N. Beck, J. Meier, and A. Shah. Transport properties of compensated µc-si:h. *Mater. Res. Soc. Proc.*, 420:801, 1996.
- [144] A. Fejfar, N. Beck, H. Stuchlikova, N. Wyrsch, P. Torres, J. Meier, A. Shah, and J. Kocka. On the transport properties of microcrystalline silicon. *Journal of Non-Crystalline Solids*, 227-230:1006, 1998.
- [145] B. Chapman. Glow Discharge Processes. John Wiley & Sons, 1980.
- [146] R.A. Haefer. Oberflächen- und Dünnschicht-Technologie Teil I, Beschichtungen von Oberflächen. Springer Verlag, Berlin, 1987.
- [147] H. Frey and G. Kienel. Dünnschichttechnologie. VDI-Verlag, 1987.

- [148] W. Luft and Y.S. Tsuo. *Hydrogenated Amorphous Silicon Alloy Deposition*. Marcel Dekker Inc., New York, Basel, Hong Kong, 1993.
- [149] J. Perrin, O. Leroy, and M.C. Bordage. Cross-section, rate constants and transport coefficients in silane plasma. *Contributions to Plasma Physics*, 36:3, 1996.
- [150] A. Matsuda. Formation kinetics and control of microcrystallite in μc-si:h from glw discharge plasma. *Journal of non-crystalline Solids*, 59-60:767, 1983.
- [151] H. Matsumura. Catalytic chemical vapor deposition (ctl-cvd) method producing high quality hydrogenated amorphous silicon. *Jpn. J. Appl. Phys.* 2, *Lett.*, 25(12):L949, 1986.
- [152] R.E.I. Schropp, K.F. Feenstra, E.C. Molenbroek, H. Meiling, and J.K. Rath. Device-quality polycrystalline and amorphous silicon films by hot-wire chemical vapour deposition. *Philos. Mag. B*, 76(3):309, 1997.
- [153] A.H. Mahan, J. Carapella, B.P. Nelson, R.S. Crandall, and I. Balberg. Deposition of device quality, low h content amorphous silicon. *J. Appl. Phys.*, 69(9):6728, 1991.
- [154] J. Cifre, J. Bertomeu, J. Puigdollers, M.C. Polo, J. Andreu, and A. Lloret. Polycrystalline silicon films obtained by hot-wire chemical vapour deposition. *Appl. Phys. A*, A59(6):645, 1994.
- [155] R.E.I. Schropp, Y. Xu, E. Iwaniczko, G.A. Zaharias, and A.H. Mahan. Microcrystalline silicon for solar cells at high deposition rates by hot wire cvd. *Mater. Res. Soc. Proc.*, 715:623, 2002.
- [156] A. Ledermann, U. Weber, C. Mukherjee, and B Schroeder. Influence of gas supply and filament geometry on the large-area deposition of amorphous silicon by hot-wire cvd. *Thin Solid Films*, 395:61, 2001.
- [157] S. Tange, K Inoue, K. Tonokura, and M. Koshi. Catalytic decomposition of sih<sub>4</sub> on a hot filament. *Thin Solid Films*, 395:42, 2001.
- [158] O. Kluth. *Texturierte Zinkoxidschichten für Silizium-Dünnschichtsolarzellen*. PhD thesis, Rheinisch-Westfählische Technische Hochschule Aachen, 2001.
- [159] O. Vetterl, R. Carius, L. Houben, C. Scholten, M. Luysberg, A. Lambertz, F. Finger, P. Hapke, and H. Wagner. Effects of structural properties of

- $\mu$ c-si:h absorber layers on solar cell performance. *Mater. Res. Soc. Proc.*, 609:A15.2.1, 2000.
- [160] A.L.B. Neto, T. Dylla, S. Klein, T. Repmann, A. Lambertz, R. Carius, and F. Finger. Defects and structure of hydrogenated microcrystalline silicon films deposited by different techniques. *J. Non-Cryst. Solids*, 338-340:168, 2004.
- [161] F. Finger, S. Klein, T. Dylla, A.L. Baia Neto, O. Vetterl, and R. Carius. Defects in microcrystalline silicon prepared with hot wire cvd. *Mater. Res. Soc. Proc.*, 715:123, 2002.
- [162] S. Klein, J. Wolff, F. Finger, R. Carius, H. Wagner, and M. Stutzmann. Microcrystalline silicon prepared by hot-wire chemical vapour deposition for thin film solar cell applications. *Jpn. J. Appl. Phys. Part II: Letters*, 41:L10, 2002.
- [163] R.J. Koval, Chi Chen, G.M. Ferreira, A.S. Ferlauto, J.M. Pearce, P.I. Rovira, C.R. Wronski, and R.W. Collins. Maximization of the open circuit voltage for hydrogenated amorphous silicon n-i-p solar cells by incorporation of protocrystalline silicon p-type layers. *Appl. Phys. Lett.*, 81(7):1258, 2002.
- [164] H. Overhof and P. Thomas. Electronic Transport in Hydrogenated Amorphous Silicon. Springer, New York, 1989.
- [165] Jiang-Huai Zhou, S. Yamasaki, J. Isoya, K. Ikuta, M. Kondo, A. Matsuda, and K. Tanaka. Pulsed esr study of the conduction electron spin center in μc-si:h. *Mater. Res. Soc. Proc.*, 452:821, 1997.
- [166] F. Finger, R. Carius, T. Dylla, S. Klein, S. Okur, and M. Gunes. Stability of microcrystalline silicon for thin film solar cell applications. *IEE Proceedings-Circuits, Devices and Systems*, 150(4):300, 2003.
- [167] M. Stutzmann. The defect density in amorphous silicon. *Philos. Mag. B*, 60(4):531, 1989.
- [168] D.H. Lee and J.D. Joannopoulos. Renormalization scheme for the transfer-matrix method and the surfaces of wurtzite zno. *Phys. Rev. B*, 24(12):6899, 1981.
- [169] H. Eicker. Method and apparatus for determining the concentration of one gaseous component in a mixture of gases. *U.S. patent 4012692*, 1977.

- [170] G.N. Advani, R. Beard, and L. Nanis. Gas measurement method. *U.S. patent* 4399684, 1977.
- [171] H.D. Le Vine. Method and apparatus for operating a gas sensor. *U.S. patent* 3906473, 1975.
- [172] Y.M. Cross and D.R. Pyke. An x-ray photoelectron spectroscopy study of the surface composition of tin and antimony mixed metal oxide catalysts. *Advances in Catalysts*, 30:97, 1981.
- [173] S.R. Morrison. Semiconductor gas sensors. *Sensors and Actuators*, 2:329, 1982
- [174] S. Green and P. Kathirgamanathan. Effect of oxygen on the surface conductance of porous silicon: towards room temperature sensor applications. *Mater. Lett.*, 52(1-2):106, 2002.
- [175] R. Carius. private communication, 2004.
- [176] N. Wyrsch, N. Beck, J. Meier, P. Torres, and S. Shah. Electric field profile in  $\mu$ c-si:h p-i-n devices. *Mater. Res. Soc. Proc.*, 420:181, 1998.
- [177] H. Antoniadis and E.A. Schiff. Isotropy of drift mobilities in hydrogen amorphous silicon. *Phys. Rev. B*, 44(8):3627, 1981.
- [178] G. Juska, K. Arlauskas, K. Genevicius, and J. Kocka. Charge carrier transport in μc-si:h. *Mater. Sci. Forum*, 297-298:327, 1999.
- [179] G. Juška, M. Viliūnas, K. Arlauskas, N. Nekrasas, N. Wyrsch, and L. Feitknecht. Hole drift mobility in  $\mu$ c-si:h. *Journal of Applied Physics*, 89(9):4971, 2001.
- [180] R. Atta-Fynn, P. Biswas, P. Ordejn, and D.A. Drabold. Systematic study of electron localization in an amorphous semiconductor. *Phys. Rev. B*, 69:085207, 2004.
- [181] A. Yelon, B. Movaghar, and H.M. Branz. Origin and consequences of the compensation (meyer-neldel) law. *Phys. Rev. B*, 46:12244, 1992.
- [182] A. Yelon and B. Movaghar. Reply to "comment on 'origin and consequences of the compensation (meyer-neldel) law". *Phys. Rev. B*, 65:077202, 2002.
- [183] L.C. Chen, L.A. Hamel, and A. Yelon. Monte carlo simulations of meyerneldel effect on carrier time-of-flight in a-si:h. *J. Non-Cryst. Solids*, 220:254, 1997.

- [184] Q. Gu, E.A. Schiff, J.B. Chevrier, and B. Equer. High-field electron-drift measurements and the mobility edge in hydrogenated amorphous silicon. *Phys. Rev. B*, 52:5695, 1995.
- [185] J.M. Marshall. Carrier diffusion in amorphous semiconductors. *Reports on Progress in Physics*, 46(10):1235, 1983.
- [186] E.A. Schiff. Trap-controlled dispersive transport and exponential band tails in amorphous silicon. *Phys. Rev. B*, 24(10):6189, 1981.
- [187] T. Tiedje and A. Rose. A physical interpretation of dispersive transport in disordered semiconductors. *Solid State Communications*, 37(1):49, 1981.
- [188] J. Orenstein and M. Kastner. Photocurrent transient spectroscopy: measurement of the density of localized states in a-as<sub>2</sub>se<sub>3</sub>. *Phys. Rev. Lett.*, 46(21):1421, 1981.
- [189] J. Orenstein, M.A. Kastner, and V. Vaninov. Transient photoconductivity and photo-induced optical absorption in amorphous semiconductors. *Philos. Mag. B*, 46(1):23, 1982.

### **List of Publications**

- 1. T. Dylla, R. Carius, and F. Finger. Electron spin resonance and electronic conductivity in moderately doped n-type microcrystalline silicon as a probe for the density of gap states. *Mater. Res. Soc. Proc.*, 715:333, 2002.
- 2. F. Finger, S. Klein, T. Dylla, A.L. Baia Neto, O. Vetterl, and R. Carius. Defects in microcrystalline silicon prepared with hot wire cvd. *Mater. Res. Soc. Proc.*, 715:123, 2002.
- 3. F. Finger, R. Carius, T. Dylla, S. Klein, S. Okur, and M. Gunes. Stability of microcrystalline silicon for thin film solar cell applications. *IEE Proceedings-Circuits, Devices and Systems*, 150(4):300, 2003.
- 4. S. Klein, F. Finger, R. Carius, T. Dylla, B. Rech, M. Grimm, L. Houben, and M. Stutzmann. Intrinsic microcrystalline silicon prepared by hot-wire chemical vapour deposition for thin film solar cells. *Thin Solid Films*, 430(1-2):202, 2003.
- 5. T. Dylla, F. Finger, and R. Carius. Adsorption and oxidation effects in microcrystalline silicon. *Mater. Res. Soc. Proc.*, 762:81, 2003.
- 6. F. Finger, S. Klein, R. Carius, T. Dylla, O. Vetterl, and A.L.B. Neto. Microcrystalline silicon prepared with hot-wire cvd. *J. Mater. Sci., Mater. Electron.*, 14(10-12):621, 2003.
- F. Finger, L. Baia Neto, R. Carius, T. Dylla, and S. Klein. Paramagnetic defects in undoped microcrystalline silicon. *Phys. Stat. Sol.*, 1(5):1248, 2004.
- 8. T. Dylla, E.A. Schiff, and F. Finger. Hole drift-mobility measurements and multiple-trapping in microcrystalline silicon. *Mater. Res. Soc. Proc.*, 2004 in press.

### Acknowledgments

At this point, I want to acknowledge all those who helped me during this work, including the ones I will forget to include in this list:

First of all, I would like to express my gratitude to Prof. Lux-Steiner for the great interest in my work and for all the discussions and suggestions to my thesis.

I would also like to thank Prof. Brewer for his interest in this work and for its revision.

My particular thanks go to my supervisor Dr. Friedhelm Finger, for his attention and patience guiding my work from the very beginning till writing the manuscript. I gratefully acknowledge his support in the discussion of ideas and results as well as in the experiments, which largely contributed to the success of this work, and that made this time a real pleasure.

I would also like to thank Prof. E.A. Schiff for giving me the opportunity to work in his lab at Syracuse University. For introducing me into the exciting field of transient photocurrent experiments, for all the enlightening discussions and all the suggestions concerning my thesis.

Dr. Reinhard Carius I thank for his great interest into my work and all the discussions.

Special thanks goes to Dr. Steve Reynolds, Torsten Bronner, Christoph Ross, Mar'yun Donna Kay Thame and Stefan Klein for carefully reading the manuscript.

I would also like to thank all my friends from the physics subbasement at SU, as there are Steluta Dinca, Jian Jun Liang, Weining Wang and Kai Zhu. I'm also very grateful to Johannes Wolff, Silke Michel and Andreas Lambertz for the technical support.

I'm very thankful to Markus Hülsback for providing the Raman data used in this work, Stefan Klein for preparing the HWCVD material, the numerous discussions and carefully reading the manuscript, Yaohua Mai, Andreas Lambertz, Gunnar Schöpe, Matthias Krause and Erke Bunte for preparing the excellent pin diodes used for TOF.

I especially thank all my colleagues from the IPV.

Last but not least, I want to express my deep gratitude to my girlfriend Dana Freese, my parents and my brother for their encouragement and support in various aspects.

# Schriften des Forschungszentrums Jülich Reihe Energietechnik / Energy Technology

#### 1. Fusion Theory

Proceedings of the Seventh European Fusion Theory Conference edited by A. Rogister (1998); X, 306 pages ISBN: 3-89336-219-3

#### 2. Radioactive Waste Products 1997

Proceedings of the 3rd International Seminar on Radioactive Waste Products held in Würzburg (Germany) from 23 to 26 June 1997 edited by R. Odoj, J. Baier, P. Brennecke et al. (1998), XXIV, 506 pages ISBN: 3-89336-225-8

#### 3. Energieforschung 1998

Vorlesungsmanuskripte des 4. Ferienkurs "Energieforschung" vom 20. bis 26. September 1998 im Congrescentrum Rolduc und im Forschungszentrum Jülich

herausgegeben von J.-Fr. Hake, W. Kuckshinrichs, K. Kugeler u. a. (1998), 500 Seiten

ISBN: 3-89336-226-6

#### 4. Materials for Advances Power Engineering 1998

Abstracts of the 6th Liège Conference edited by J. Lecomte-Beckers, F. Schubert, P. J. Ennis (1998), 184 pages ISBN: 3-89336-227-4

#### 5. Materials for Advances Power Engineering 1998

Proceedings of the 6th Liège Conference edited by J. Lecomte-Beckers, F. Schubert, P. J. Ennis (1998), Part I XXIV, 646, X pages; Part II XXIV, 567, X pages; Part III XXIV, 623, X pages

ISBN: 3-89336-228-2

#### 6. Schule und Energie

1. Seminar Energiesparen, Solarenergie, Windenergie. Jülich, 03. und 04.06.1998

herausgegeben von P. Mann, W. Welz, D. Brandt, B. Holz (1998), 112 Seiten ISBN: 3-89336-231-2

#### 7. Energieforschung

Vorlesungsmanuskripte des 3. Ferienkurses "Energieforschung" vom 22. bis 30. September 1997 im Forschungszentrum Jülich herausgegeben von J.-Fr. Hake, W. Kuckshinrichs, K. Kugeler u. a. (1997), 505 Seiten

ISBN: 3-89336-211-8

#### Schriften des Forschungszentrums Jülich Reihe Energietechnik / Energy Technology

#### Liberalisierung des Energiemarktes

Vortragsmanuskripte des 5. Ferienkurs "Energieforschung" vom 27. September bis 1. Oktober 1999 im Congrescentrum Rolduc und im Forschungszentrum Jülich

herausgegeben von J.-Fr. Hake, A. Kraft, K. Kugeler u. a. (1999), 350 Seiten ISBN: 3-89336-248-7

#### 9. Models and Criteria for Prediction of Deflagration-to-Detonation Transition (DDT) in Hydrogen-Air-Steam-Systems under Severe Accident Conditions

edited by R. Klein, W. Rehm (2000), 178 pages

ISBN: 3-89336-258-4

#### 10. High Temperature Materials Chemistry

Abstracts of the 10<sup>th</sup> International IUPAC Conference, April 10 - 14 2000, Jülich edited by K. Hilpert, F. W. Froben, L. Singheiser (2000), 292 pages ISBN: 3-89336-259-2

#### 11. Investigation of the Effectiveness of Innovative Passive Safety Systems for **Boiling Water Reactors**

edited by E. F. Hicken, K. Verfondern (2000), X, 287 pages

ISBN: 3-89336-263-0

#### 12. Zukunft unserer Energieversorgung

Vortragsmanuskripte des 6. Ferienkurs "Energieforschung" vom 18. September bis 22. September 2000 im Congrescentrum Rolduc und im Forschungszentrum Jülich

herausgegeben von J.-Fr. Hake, S. Vögele, K. Kugeler u. a. (2000),

IV, 298 Seiten

ISBN: 3-89336-268-1

#### 13. Implementing Agreement 026

For a programme of research, development and demonstration on advances fuel

#### **Fuel Cell Systems for Transportation**

Annex X. Final Report 1997 - 1999

edited by B. Höhlein; compiled by P. Biedermann (2000), 206 pages

ISBN: 3-89336-275-4

#### 14. Vorgespannte Guß-Druckbehälter (VGD) als berstsichere Druckbehälter für innovative Anwendungen in der Kerntechnik

Prestressed Cast Iron Pressure Vessels as Burst-Proof Pressure Vessels for **Innovative Nuclear Applications** 

von W. Fröhling, D. Bounin, W. Steinwarz u. a. (2000) XIII, 223 Seiten

ISBN: 3-89336-276-2

# Schriften des Forschungszentrums Jülich Reihe Energietechnik / Energy Technology

#### 15. High Temperature Materials Chemistry

Proceedings of the 10<sup>th</sup> International IUPAC Conference held from 10 to 14 April 2000 at the Forschungszentrum Jülich, Germany Part I and II

edited by K. Hilpert, F. W. Froben, L. Singheiser (2000), xvi, 778, VII pages ISBN: 3-89336-259-2

# 16. Technische Auslegungskriterien und Kostendeterminanten von SOFC- und PEMFC-Systemen in ausgewählten Wohn- und Hotelobjekten

von S. König (2001), XII, 194 Seiten

ISBN: 3-89336-284-3

#### 17. Systemvergleich: Einsatz von Brennstoffzellen in Straßenfahrzeugen

von P. Biedermann, K. U. Birnbaum, Th. Grube u. a. (2001), 185 Seiten ISBN: 3-89336-285-1

#### 18. Energie und Mobilität

Vorlesungsmanuskripte des 7. Ferienkurs "Energieforschung" vom 24. September bis 28. September 2001 im Congrescentrum Rolduc und im Forschungszentrum Jülich

herausgegeben von J.-Fr. Hake, J. Linßen, W. Pfaffenberger u. a. (2001), 205 Seiten

ISBN: 3-89336-291-6

#### 19. Brennstoffzellensysteme für mobile Anwendungen

von P. Biedermann, K. U. Birnbaum, Th. Grube u. a. (2002)

PDF-Datei auf CD ISBN: 3-89336-310-6

#### 20. Materials for Advances Power Engineering 2002

Abstracts of the 7th Liège Conference edited by J. Lecomte-Beckers, M. Carton, F. Schubert, P. J. Ennis (2002), c. 200 pages

ISBN: 3-89336-311-4

#### 21. Materials for Advances Power Engineering 2002

Proceedings of the 7th Liège Conference

Part I, II and III

edited by J. Lecomte-Beckers, M. Carton, F. Schubert, P. J. Ennis (2002),

XXIV, 1814, XII pages ISBN: 3-89336-312-2

#### 22. Erneuerbare Energien: Ein Weg zu einer Nachhaltigen Entwicklung?

Vorlesungsmanuskripte des 8. Ferienkurs "Energieforschung" vom 23. bis 27. September 2002 in der Jakob-Kaiser-Stiftung, Königswinter herausgegeben von J.-Fr. Hake, R. Eich, W. Pfaffenberger u. a. (2002), IV. 230 Seiten

ISBN: 3-89336-313-0

## 23. Einsparpotenziale bei der Energieversorgung von Wohngebäuden durch Informationstechnologien

von A. Kraft (2002), XII, 213 Seiten

ISBN: 3-89336-315-7

#### 24. Energieforschung in Deutschland

Aktueller Entwicklungsstand und Potentiale ausgewählter nichtnuklearer Energietechniken

herausgegeben von M. Sachse, S. Semke u. a. (2002), II, 158 Seiten,

zahlreiche farb. Abb. ISBN: 3-89336-317-3

#### 25. Lebensdaueranalysen von Kraftwerken der deutschen Elektrizitätswirtschaft

von A. Nollen (2003), ca. 190 Seiten

ISBN: 3-89336-322-X

## 26. Technical Session: Fuel Cell Systems of the World Renewable Energy Congress VII

Proceedings

edited by D. Stolten and B. Emonts (2003), VI, 248 pages

ISBN: 3-89336-332-7

#### 27. Radioactive Waste Products 2002 (RADWAP 2002)

**Proceedings** 

edited by R. Odoj, J. Baier, P. Brennecke and K. Kühn (2003), VI, 420 pages

ISBN: 3-89336-335-1

#### 28. Methanol als Energieträger

von B. Höhlein, T. Grube, P. Biedermann u. a. (2003), XI, 109 Seiten

ISBN: 3-89336-338-6

# 29. Hochselektive Extraktionssysteme auf Basis der Dithiophosphinsäuren: Experimentelle und theoretische Untersuchungen zur Actinoiden(III)-Abtrennung

von S. A. H. Nabet (2004), VI, 198 Seiten

ISBN: 389336-351-3

#### 30. Benchmarking-Methodik für Komponenten in Polymerelektrolyt-Brennstoffzellen

von Matthias Gebert (2004), 194 Seiten

ISBN: 3-89336-355-6

#### 31. Katalytische und elektrochemische Eigenschaften von eisen- und kobalthaltigen Perowskiten als Kathoden für die oxidkeramische Brennstoffzelle (SOFC)

von Andreas Mai (2004), 100 Seiten

ISBN: 3-89336-356-4

# Schriften des Forschungszentrums Jülich Reihe Energietechnik / Energy Technology

#### 32. Energy Systems Analysis for Political Decision-Making

edited by J.-Fr. Hake, W. Kuckshinrichs, R. Eich (2004), 180 pages

ISBN: 3-89336-365-3

### 33. Entwicklung neuer oxidischer Wärmedämmschichten für Anwendungen in stationären und Flug-Gasturbinen

von R. Vaßen (2004), 141 Seiten

ISBN: 3-89336-367-X

### 34. Neue Verfahren zur Analyse des Verformungs- und Schädigungsverhaltens von MCrAlY-Schichten im Wärmedämmschichtsystem

von P. Majerus (2004), 157 Seiten

ISBN: 3-89336-372-6

# 35. Einfluss der Oberflächenstrukturierung auf die optischen Eigenschaften der Dünnschichtsolarzellen auf der Basis von a-Si:H und $\mu$ c-Si:H

von N. Senoussaoui (2004), 120 Seiten

ISBN: 3-89336-378-5

### 36. Entwicklung und Untersuchung von Katalysatorelementen für innovative Wasserstoff-Rekombinatoren

von I.M. Tragsdorf (2005), 119 Seiten

ISBN: 3-89336-384-X

### 37. Bruchmechanische Untersuchungen an Werkstoffen für Dampfkraftwerke mit Frischdampftemperaturen von 500 bis 650°C

von L. Mikulová (2005), 149 Seiten

ISBN: 3-89336-391-2

### 38. Untersuchungen der Strukturstabilität von Ni-(Fe)-Basislegierungen für Rotorwellen in Dampfturbinen mit Arbeitstemperaturen über 700 °C

von T. Seliga (2005), 106 Seiten

ISBN: 3-89336-392-0

#### 39. IWV-3 Report 2005. Zukunft als Herausforderung

(2005), 115 Seiten ISBN: 3-89336-393-9

#### 40. Integrierter Photodetektor zur Längenmessung

von E. Bunte (2005), XI, 110 Seiten

ISBN: 3-89336-397-1

# 41. Microcrystalline Silicon Films and Solar Cells Investigated by Photoluminescence Spectroscopy

by T. Merdzhanova (2005), X, 137 Seiten

ISBN: 3-89336-401-3

#### Schriften des Forschungszentrums Jülich Reihe Energietechnik / Energy Technology

#### 42. IWV-3 Report 2005. Future as a challenge

(2005), 115 Seiten ISBN: 3-89336-405-6

#### 43. Electron Spin Resonance and Transient Photocurrent Measurements on Microcrystalline Silicon

by T. Dylla (2005), X, 138 Seiten ISBN: 3-89336-410-2



Band/Volume 43 ISBN 3-89336-410-2 **Energietechnik Energy Technology**